DISSERTATION

Robust Thin Films for High Temperature Surface Acoustic Wave Devices

zur Erlangung des akademischen Grades
Doktor der technischen Wissenschaften (Dr. techn.)

Institut für Sensor- und Aktuatorsysteme
Technische Universität Wien

Dipl.-Ing. Dipl.-Ing-(FH) Manuel Gillinger
Matrikelnummer: e0826952

Wien, 2018

Verteidigung: Wien, 08 Jänner 2018

Betreuer: Univ.-Prof. Dr.rer.nat. Ulrich Schmid
Technische Universität Wien, Österreich
Gutachter: Ao.Univ.-Prof. Dr.techn. Christoph Eisenmenger-Sittner
Technische Universität Wien, Österreich
Gutachter: Univ.-Prof. Dr.sc. Silvan Schmid
Technische Universität Wien, Österreich

ABSTRACT

Surface Acoustic Wave (SAW) devices are nowadays most commonly used in the telecommunication sector as frequency filters or as delay lines. Besides these standard applications, such devices can also be used as key component in battery-less and wireless sensor applications. This may include temperature measurements, both in high temperature as well as aggressive gaseous environments.

Current solutions for high temperature stable SAW devices are based on substrates like *langasite*, *langatate* oder *langanite*. The main disadvantage of all these crystals is the low phase velocity (~2700 m/s) and the high transition losses of the signal at elevated temperatures. To overcome these drawbacks, aluminum nitride (AlN) sputter-deposited as piezoelectric thin film in combination with sapphire as substrate show a promising alternative. Phase velocities of around 5700 m/s can be reached, which is substantially higher compared to other systems, named above. Therefore, with the same device geometry even higher resonance frequencies can be achieved.

In this thesis the modifications of the electro-mechanical properties of aluminum nitride thin films due to the influence of temperature as well as inert and aggressive gases are investigated. The results showed that AlN layers are stable without changing their device relevant properties such as crystallographic structure, surface roughness, intrinsic stress, piezoelectricity and leakage current up to 700 °C independent of the surrounding gas atmosphere. At higher temperatures, the AlN layer gets oxidized in an oxygen-containing atmosphere, resulting in the loss of piezoelectric properties. Therefore, the impact of different passivation coatings on the oxidation resistance of the active AlN thin film was investigated. A promising solution is reactively sputtered-deposited silicon nitride. The oxidation resistance of this layer was evaluated by continuously monitoring with a high temperature X-ray diffraction equipment any changes and hence, any oxidation of the underlying AlN for 24 hours at 1000 °C in pure oxygen atmosphere. Furthermore, possible electrode materials are examined, such as platinum and iridium. To measure the impact of temperature load the modification in film resistance of the metallization lines having a width between 1 µm and 50 µm was investigated.

Finally, SAW devices based on aluminum nitride on sapphire substrates were fabricated. For a better device understanding the thickness of the piezoelectric layer and the wave propagation direction with respect to the crystallographic orientation of the sapphire substrate were varied systematically. In addition, the influence of the electrode material on the phase velocity was examined. As a result, not the thickness, but predominantly the density of the electrode material has an impact and reduces the phase velocity. Finally, SAW devices were measured during high temperature load up to 800 °C in an inert gas atmosphere. The measurements showed that the temperature sensitivity is almost linear in the investigated temperature range. An additional passivation layer has only a minor influence on the latter device parameter.

KURZFASSUNG

Oberflächenwellen-Bauelemente werden heutzutage vorwiegend in Hochfrequenzanwendungen, beispielsweise als Frequenzfilter oder als Zeitverzögerungselemente im Bereich von Telekommunikationsanwendungen, eingesetzt. Neben diesem klassischen Einsatzgebiet können diese Bauelemente in der Zukunft auch eine Schlüsselfunktion in batterielosen und drahtlos auslesbaren Sensorknoten einnehmen. Ein interessantes Anwendungsbeispiel ist die präzise Temperaturmessung unter rauen Umbgebungsbedingungen, was typischerweise hohe Temperaturen als auch eine aggressive Gasatmosphäre umfasst.

Momentan verwendete SAW-Materialien für solche Anwendungen basieren auf *Langasit*, *Langatat* oder *Langanit*. Nachteile dieser einkristallinen Substrate sind die niedrigen Schallgeschwindigkeiten (~2700 m/s) und die hohen Dämpfungsverluste bei erhöhten Temperaturen. Als vielversprechende Alternative gilt Aluminiumnitrid (AlN), das mit Hilfe der Sputtertechnik als piezoelektrisches Material auf einem Saphirsubstrat aufgebracht wird. In dieser Materialkombination sind Schallgeschwindigkeiten von ungefähr 5700 m/s erreichbar, was deutlich höher ist als bei den anderen Systemen. Dadurch können bei gleichen Bauteil-dimensionen höhere Resonanzfrequenzen erreicht werden.

Im Rahmen dieser Arbeit wurden die Änderungen der elektro-mechanischen Eigenschaften von gesputterten Aluminiumnitrid Dünnfilmen unter dem Einfluss von Temperatur sowie unter inerten (d.h. Stickstoff und Argon) als auch aggressiven (d.h. Sauerstoff) Gasatmosphären untersucht. Dabei zeigte sich, dass die AlN-Schichten bis 700 °C unabhängig von der Gasatmosphäre keine Änderung der Schichteigenschaften aufweisen. Bei höheren Temperaturen wird die Aluminiumnitrid Schicht jedoch in Sauerstoffumgebung dauerhaft zu einem Aluminiumoxinitrid umgewandelt, was zu einem Verlust der piezoelektrischen Eigenschaft führt. Um ihre Temperaturstabilität zu erhöhen, wurden auch mehrere Passivierungsschichtsysteme untersucht, welche insbesondere die Oxidationsresistenz erhöhen sollte. Ein vielversprechendes Schicht-

material ist reaktives gesputtertes Siliziumnitrid. Diese Passivierungsschicht konnte durch Röntgenbeugungsmessungen nachweislich selbst bei 1000 °C die Aluminiumnitridschicht für 24 Stunden vor Oxidationsprozessen schützen. Des Weiteren wurden auch mögliche Elektrodenmaterial mit Leiterbahnenbreiten zwischen 1 µm und 50 µm bestehend aus Platin und Iridium für Hoch-Temperatur Anwendungen untersucht.

Mit Hilfe des gewonnen Wissens um die einzelnen Materialien wurden Oberflächenbauelemente basierend aus der Kombination Aluminiumnitrid auf Saphirsubstrat hergestellt. Der Fokus lag bei diesen Untersuchungen auf dem Einfluss der Dicke der piezoelektrischen Schicht als auch auf der Ausrichtung der Interdigitalstrukturen hinsichtlich der kristallographischen Struktur des Saphirsubstrates. Im Zuge dieser Untersuchungen wurde auch ein Einfluss des Elektrodenmaterials auf die Schallgeschwindigkeit festgestellt, wobei hier nicht primär die geometrischen Abmessungen, sondern die Elementmasse den entscheidenden Einfluss spielt. Abschließend wurden auch SAW Bauteile bis 800 °C auf ihre Temperatursensitivität in einer inerten Gasatmosphäre hin vermessen. Dabei zeigte sich, dass die Temperatursensitivität über den ganzen Messbereich nahezu linear ist. Eine zusätzliche Passivierungsschicht auf dem Bauteil ändert diesen Wert nur minimal.

ACKNOWLEDGMENTS

I want thank Prof.-Dr. Ulrich Schmid for the possibility to work on this project at his institute. He had always time and patience for the problems, which appeared during the last years.

Also a thanks goes to Dr. Michael Schneider and Dr. Achim Bittner, which helped me by solving problems and discussing and evaluating of the different results.

Dr. Klaudia Hradil and Werner Artner for helping me with the XRD measurements.

Dr. Michael Stoeger-Pollach for the analysis of the samples at the HRTEM.

I want also thank Dr. Kirill Shaposhnikov for the simulation and furthering the understanding of my SAW devices. Dr. Jochend Bardong from CTR who helped me with the measurements of the SAW devices.

My bachelor students Theresia Knobloch and Aleksandra Marković for their scientific contribution to this work.

During this time a lot of samples were fabricated in the cleanroom. A thanks goes to Dr. Johannes Schalko, Sophia Ewert, Patrick and Michael Buchholz for their effort to keep the cleanroom running. To Franz Prewein for his support and solving problem, which appeared with mechanical issues.

I thank also Andreas Astleitner for his support at IT and equipment issues. To the administration in special Martina Nuhsbaumer for her relentless endeavors in bureaucratic questions. Furthermore, I want thank my colleagues Georg Pfusterschmid, Peter Schmid, Martin Fischeneder, Patrick Mayrhofer, and Elisabeth Wistrela for a wonderful time. A thanks goes to *'Team Cooking'* for the rich-full and funny discussion during lunch time.

I also want to thanks my family. Werner, Maria, Mike, Marina and my niece Marlene, which supported me during the time as Phd. student and a long period before that. Finally, a special thanks goes to Nathalie for the time at my side.

This project has been supported within the COMET - Competence Centers for Excellent Technologies Programme by BMVIT, BMWFJ and the federal provinces of Carinthia and Styria.

CONTENTS

1 INTRODUCTION

1.1 Motivation

Since the beginning of forging the knowledge about the precise, actual temperature of the workpiece is important during forging, hardening and tempering [1]. For example, to harden steel, the workpiece needs a minimum temperature of 720 °C to form austenite steel. During quenching of the workpiece with oil or water, the austenite crystal becomes martensite, which has a *Vickers Pyramid Number* (HV) hardness of 1000 HV compared to iron with 30-80 HV [1, 2]. After hardening of the workpiece a temper step is needed to release the thermal induced stress inside the material. This is done between 180 °C and 650 °C [3]. Therefore, to estimate the temperature of the workpiece, a straight forward approach is to determine the glowing color of the workpiece. Depending on the workpiece temperature the radiated color is changing. For example between 580 °C and 650 °C the color is brown-red and becomes dark-red up to 750 °C. With higher temperatures the color changes several times and becomes bright-yellow for temperatures between 1150 °C and 1250 °C [4]. But, this optical approach is quite a rough method enabling the manufacturer to estimate the temperatures.

Another method for temperature sensing is to make use of the changing volume characteristic. By supplying thermal energy to a system, standard materials typically expand. Mercury thermometers are widely used and work most reliable based on this principle. To increase the sensitivity a reservoir or bulb at the end of the thermometer is used. The expansion of the volume is amplified by the low diameter of a tube [5]. If the pressure level and the amount of molecules are kept constant, the temperature T can be determined within an ideal gas approximately with the formula: $T \approx (V/V_0 - 1)/\gamma + T_0$, were V is the volume in the expanded state, V_0 is the original volume, γ is the volume specific expansion coefficient and T_0 represents the reference temperature, respectively.

By reducing the approach to a linear system, the behavior can be expressed by only a length expansion coefficient $\alpha = \Delta L/(L \cdot \Delta T)$, where ΔL is the change in length, L the original length and ΔT the temperature change. Therefore, the temperature can be calculated with a modified formula $T \approx (L/L_0 - 1)/\alpha + T_0$, where α is for example platinum $8.8 \cdot 10^{-6}\ K^{-1}$. This still leaves the challenging task to measure the exact change in length [6].

A more straight forward, and hence accurate way for temperature determination is to measure the change in resistance of the conductive materials like platinum. For example, platinum films have a reference resistance R_0 of 100 Ω or 1000 Ω at a given reference temperature T_0. During a temperature load the resistance of the platinum film changes. The resistance at a given temperature R_T is calculated according to $R_T = R_0[1 + A \cdot (T - T_0) + B \cdot (T - T_0)^2]$ with T as the actual temperature. The material constants A and B are for example for platinum $A = 3.9083 \cdot 10^{-3} {}^\circ C^{-1}$ and $B = -5.775 \cdot 10^{-7} {}^\circ C^{-2}$ [6]. The formula can be simplified for small temperature ranges and linear behavior to $R_T = R_{20}[1 + \alpha_{20}(T - 20^\circ C)]$ with the platinum resistance R_{20} at a temperature of 20 °C. Such platinum sensors are used up to 500 °C. [6]

A different electrical measurement approach is to use thermocouples. These devices consist of two different metals forming electrical junctions. A temperature dependent voltage is generated because of the thermoelectric effect. Depending on the selected material combination, the sensitivity is between 40 – 60 µV/°C. For standard Type K (chrome – alumel) the measurable temperature range is from -200 °C up to 1270 °C [7]. With special materials like platinum/rhodium alloys the range is increased up to 1800 °C but their usage is limited to temperatures above 50 °C [7].
The disadvantage when measuring the resistance or when applying the thermocouple method is the dependency on electrical wiring. They are isolated typically with silica or polyethylene, which are not temperature resistive and therefore replaced for example by ceramic alloys or sintered magnesia for high temperature applications [7]. Nevertheless for not stationary or moving applications like crucible in a smelting works or steel industry, a wireless temperature measurement system would be preferable.

Such a contact-less measurement technique for determining the system temperature is commercially available with pyrometers. The basic idea behind this measurement method is that every object, emits heat radiation and with a special detector like a thermocouple-chain or photo-detector, the radiation spectra can be measured [6]. The evaluation result of the spectra yields the temperature. The emitted power is $P = \sigma \cdot A \cdot T^4$, where σ is the Stefan-Boltzmann constant $5.6704 \cdot 10^{-8} m^{-2} K^{-4}$ and A the emitting area [6]. The highest emission rate is reached from an ideal black body. For real world objects, an emission coefficient ϵ has to be multiplied. For example, in the cement or rolled material industry a 2-siliconelement detector is used to measure a typical temperature range between 700 °C and 3100 °C [6]. A disadvantage of such a system is the necessary optical access, which can be rather big. Furthermore, the emission ratio is not necessarily constant and can change over time.

A promising approach to measure temperature contact-less is the usage of surface acoustic wave (SAW) devices. The devices are small and can therefore be easily integrated or embedded in the existing, technical system. The measurement principle is that with changing temperature the materials expand and therefore the mechanical wavelength λ is increased. According to $f = c/\lambda$ the frequency is shifted, where f is the frequency and c the sound velocity. By adding an antenna to the device, the temperature can be read-out in a wireless and battery-less way [8]. Currently used SAW devices are based on langasite quartz with a phase velocity of $v_p = 2700\,\mathrm{m/s}$ [8]. These devices are working in the free radio range of 428 MHz to 439 MHz [9]. To reach the free usable 2.4 GHz range, systems with higher phase velocities have to be used. The advantage of such high frequencies lies in smaller antennas, which reduces the device dimension. An alternative to the langasite family are piezoelectric thin film layers on top of hard materials. A promising system can be aluminum nitride in combination with sapphire, where phase velocities of $v_p = 5700\,\mathrm{m/s}$ are achieved [8]. This system also promises to be stable under harsh environmental conditions.

1.2 Surface Acoustic Wave Sensors

Currently available temperature sensors based on the SAW technology are working in the free radio frequency range of 428 MHz to 439 MHz with a maximum measureable temperature of 120 °C [9]. The maximum temperature is too low for example to operate in a gas turbine, where the hot exhaust gas can reach a temperature of up to 700 °C [10]. To enhance the maximum measurable temperature, the materials used in such SAW sensor architectures have to withstand or should be protected against the harsh environmental conditions in a gas turbine application. Therefore, to understand the challenge of fabricating temperature sensors based on SAW devices, the knowledge of altering and changing material properties during high temperature load in aggressive gases has to be obtained. The main component for SAW devices is the piezoelectric layer, which transforms electrical energy in mechanical displacement and *vice versa*. Currently used piezoelectric materials are based on langasite ($La_3Ga_5SiO_{14}$, LGS), langatate ($La_3Ga_{5.5}Ta_{0.5}O_{14}$, LGT) or langanite ($La_3Ga5.5Nb_{0.5}O14$, LGN), which exhibit major disadvantages due to the low phase velocity (e.g., LGS: 2700 m/s) and high acoustic propagation losses, which increases dramatically with higher temperature and frequencies [8, 11, 12]. For the needed electrical energy and signal transport, novel alloys based on Pt-Ni / Pt-Zr thin films on top of LGS are investigated, which withstand temperature cyclings up to 1000 °C [13]. But even this material has to be protected by a very thin (50 nm) $SiAlON$ or $ZrSiON$ coating film [14–16].

For this work aluminum nitride (AlN) was chosen as the piezoelectric thin film. It can be fabricated easily by sputter deposition using a pure aluminum target in a reactive nitrogen plasma. Given that AlN reacts with oxygen to alumina at high temperatures, an analysis of the oxidation behavior of AlN in harsh environments is necessary to find the limits of the material system. The next challenging part are the inter-digital-transducer (IDT) elements, consisting of a conductive material, commonly aluminum or copper. A reason for this material choice is the high conductivity and the low mass. Given, that these materials cannot be operated at high temperatures above 500 °C, because of the low melting point [17], other materials have to be selected for example platinum or iridium with the disadvantage of a higher electrical resistivity and a higher density. But, the latter materials can be easily fabricated with sputter deposition method, thus staying within the same technology platform for film sythetization In this work the electrode material thickness was chosen to be between 40 nm and 50 nm for platinum and 100 nm for aluminum. A thicker electrode means a higher mass loading effect and for thinner electrodes, the resistance will increase significantly. Figure 1.1 shows a typical SAW delay line device with two IDT's. The sapphire substrate and the piezoelectric thin film AlN are optically transparent.

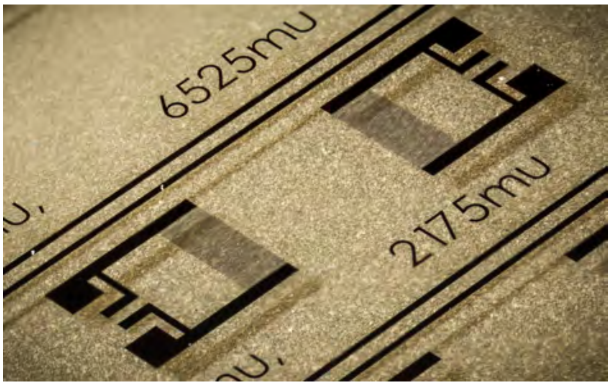

Figure 1.1: SAW delay line with two IDT's placed on top of AlN and sapphire both being optically transparent.

1.3 Structure of the Thesis

Basically, this study can be divided into three main parts: the analysis of the piezoelectric AlN thin film layer, the evaluation of the electrode material for the inter-digital-transducers with possible passivation coatings and the characterization of surface acoustic wave devices, based on the results of the former two parts. In all parts, the impact of harsh environments like oxygen atmosphere at temperatures up to 1000 °C will be investigated. Similar measurements in inert atmospheres like nitrogen, argon or vacuum serve as reference. Part I deals with the changing and altering of the aluminum nitride layer properties. For this purpose at least 2 µm thin AlN films have to be deposited with low intrinsic stress values to ensure proper adhesion to the substrate. The monitored material properties during temperature load were the biaxial intrinsic stress, crystallographic structure and the electrical leakage current. The next section focuses on the behavior of the electrode material and possible protective passivation coatings. Oxidation generally degenerates the electrode performance and changes the chemical composition of the material and the electrical resistance will increase. Noble and common metals are compared for their operation capability at high temperatures and pure oxygen atmosphere. To improve the durability of the electrodes sputtered silicon nitride, alumina and aluminum nitride are selected as passivation layers. The final main section deals with SAW test structures. The behavior of different substrate materials as well as the wave propagation direction relative to the substrate crystallographic directions were investigated. In addition, the impact of substrate pre-treatment and mass loading effects on the SAW performance is evaluated. Besides pure AlN also Scandium doped AlN as the piezoelectric layer is investigated as a promising alternative to AlN due to higher piezoelectric coefficients. Finally, SAW devices are successfully measured during high temperature loads up to 800 °C in an inert nitrogen gaseous atmosphere.

2 FABRICATION TECHNOLOGIES AND EXPERIMENTAL METHODS

2.1 Fabrication Technologies

2.1.1 Physical Vapor Deposition

Physical **V**apor **D**eposition (PVD) is a standard technique to deposit thin films on a surface. Besides PVD, **C**hemical **V**apor **D**eposition (CVD) processes are an alternative for film synthetization. The main difference between both techniques is that within CVD process the source material is provided with a gaseous chemical precursor compared to a PVD process, where the source material is introduced in the deposition chamber as solid. In this work only PVD deposited layers are used. Therefore, in the following the different types, sputtering and thermal evaporation, are explained briefly.

Sputtering

In microelectronics and MEMS sputtering is regarding as standard to deposit thin layers covering a large variety of materials on top of a surface. At the target, which is typically a disc consisting of the source material, a highly negative electrical potential is applied. At low pressure values around 2-6 µbar and high voltage between 300-1500 V, the gas (e.g. argon) gets ionized and a plasma is ignited in the volume between target and substrate. Positive charged ions like Ar^+ generated in the plasma are accelerated towards the target by the electrical field, resulting in impinging particles on the target surface. During this bombardment, kinetic energy is transferred to the target and with a cascade momentum transfer surface atoms are emitted. These atoms are traveling to the substrate and condense on the surface. To increase the sputter yield, permanent magnets are placed directly behind the target. This technique is called magnetron sputtering. Due to the additional magnetic field electrons are forced to move in

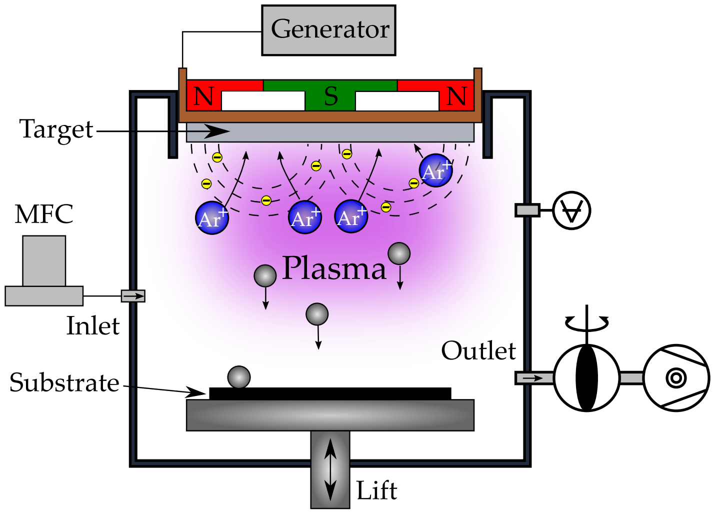

Figure 2.1: Schematic overview of a magnetron sputter equipment.

closed circular paths close to the target surface. Doing so, the electrons remain longer in the plasma where they generate more ions, thus increasing the ionization rate. With the increased amount of ions, more ions are transferred to the target and hence, more atoms are emitted, resulting in an increased sputter yield [18]. A schematic overview of a magnetron sputter equipment showing key components is given in Figure 2.1.

With this technique, even compound layers consisting of different chemical elements can be deposited while preserving to a large degree of the original chemical composition of the target. Therefore, a possible approach is that the target consists of a homogenous mixture of all chemical components needed for film synthetization, by applying either powder sintering or by fusing a special alloy material. Another method to deposit a compound layer is the so-called reactive sputter process, where for example the inert gas argon is at least partly replaced by reactive gases like nitrogen, oxygen or a combination of several gases. When traveling from the target to the substrate the ejected atoms react with the chemically active gaseous species in the plasma. With this approach, compound layers like AlN, Al_xO_y or Si_xN_y can be realized. Further details about this deposition technique can be found elsewhere [18–20]. In this work a sputter equipment from vonAndenne (LS730s) was used. Additionally, to measure the substrate temperature, a pyrometer (DIAS Pyrospot DGE 10N) with a working range from 100 °C up to 850 °C is used. The pyrometer was placed in the process chamber just below the substrate holder and measures continuously the thermal radiation of the holder.

Thermal Evaporation

Within PVD evaporation is another standard technique to deposit thin films. The target material is placed in a crucible or so-called boat and heated up in a vacuum chamber to a temperature above the melting point of the target material. Some of the melted material evaporates and moves straight to the substrate where the atoms condense. There are several methods for heating up the material. A straight-forward approach is to use an electrically conductive so called *boat*, with a high current being driven through the boat, which then heats up the material. This is a simple technique, but not all materials can be used, because the energy needed to evaporate materials with a high melting-point would lead to a diffusion of atoms from the boat into the material to be evaporated basically resulting in a contamination. Therefore, another concept is to heat the material with an electron beam.

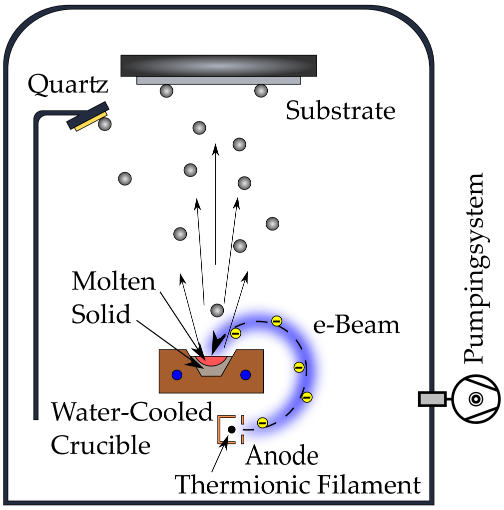

Figure 2.2: Schematics of an e-beam evaporation equipment.

Electrons are extracted by a high electrical field from a thermionic filament. The trajectories of emitted electrons are bent and guided with a magnetic field to the target material. With such a system high energy can be transferred to the material and even high melting materials like tantalum or titanium can be evaporated resulting in thin films properties with low chemical contamination from the crucible. The crucible, where the material is placed, is also water cooled, so that highly pure layers of a single material can be deposited. Such equipment is shown in Figure 2.2. To monitor the thickness of the deposited thin film an oscillating quartz is placed in the path of the evaporated material. The resonance frequency of the quartz is shifted when covered with additionally evaporation material, thus representing a precise gauge to monitor this important film parameter.

2.1.2 Structure Zone Model

There are several **S**tructure **Z**one **M**odels (SZM), which predict the corresponding microstructure of a deposited layer depending on different deposition parameters, like temperature, gaseous back pressure or ion energy. The first SZM was introduced by Movchan and Demchishin in 1969. The only parameter was the homologous temperature T_h, which expresses the deposition temperature T as a fraction of the melting point T_m of the layer, according to $T_h = T/T_m$ (Kelvin scale). Basically, three main zones were defined. The layer in *Zone 1* (at $T_h < 0.3$) has freestanding columns with freestanding tips, a high porosity and a high dislocation density. This poor microstructure is explained by the low ad-atom mobility, which leads to permanent nucleation of new grains during film growth. In *Zone 2* ($0.3 < T_h < 0.5$), surface diffusion starts to dominate so that ad-atoms can overcome shadowing effects arising from e.g. the surface roughness. These films have a dense microstructure with columnar grains and a smooth surface characteristics. In *Zone 3* ($T_h > 0.5$) recrystallization and bulk diffusion leads to dense layers with large grains [21]. In addition, Thornton *et al.* inserted the argon pressure as an additional important parameter to the SZM for predicting the microstructure of sputter deposited films. In this context, a *Zone T* is defined, which indicates a transition region. This latter zone is again densely packed and has a fibrous structure. At low homologous temperatures ($T_h < 0.5$) and low argon pressures ($p < 20$ µbar) the transition zone replaces the original *Zone 1*. The SZM as presented from Thornton is shown in Figure 2.3a [22].

Messier *et al.* extended the SZM from Movchan with the bias voltage as an additional parameter. The *Zone T* is enlarged at low homologous temperatures ($T_h < 0.3$), when increasing the bias voltage [24]. In 2010, Anders presented a SZM with adding the energy of the deposited ions [23]. The zone model is shown in Figure 2.3b. At high ion fluxes, the deposition process inverts and more atoms are removed from the substrate surface than deposited. The numerical values on the axes serve only for orientation as guide for the eyes. Despite these theoretical considerations it is worth noting that the

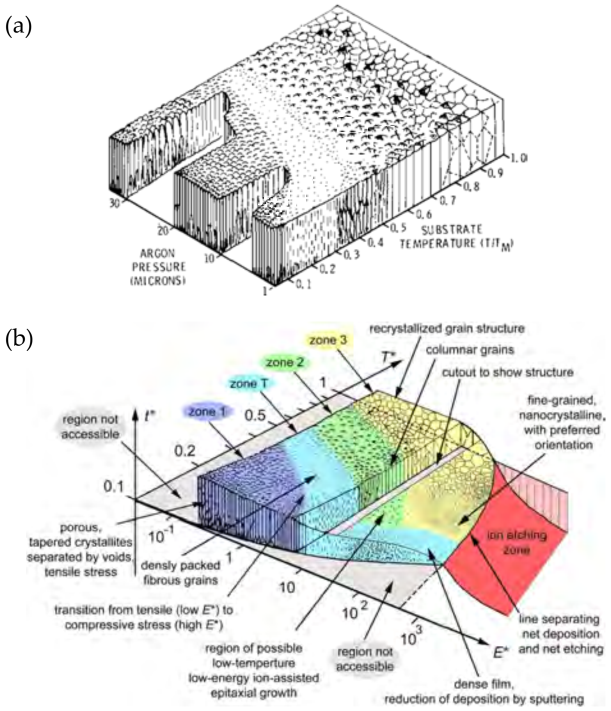

Figure 2.3: Structure Zone Model extended by Thornton (a) and Anders (b) [22][23].

final result on the microstructure may vary, depending on e.g. the deposited thin film material and the used equipment [23].

2.1.3 Growth Defects in Thin Films

During depositing of a material structural defects are implemented inside the layer. Basically, these defects can be classified according to their dimension [25]:

- 0-dim: Point Defects
- 1-dim: Line Defects
- 2-dim: Area Defects
- 3-dim: Cluster Defects

Point defects are irregularities on atomic lattice level. Two kinds of defects can be found, named as Schottky and Frenkel defects. The first type are vacancies in the atomic lattice, where atoms are missing. This can occur, because above zero Kelvin atoms starts to oscillate. With higher temperatures, the probability increases that atoms leave their original sites and diffuse to another lattice site. In contrast, at Frenkel defects, the atom does not move to another position in the crystallographic lattice, but it rests on an interstitial site. Both defect types can also be generated during deposition, predominantly due to a low surface ad-atom mobility [25]. Line defects are relocation of the lattice and are mostly generated by plastic deformation. This defect type has a strong influence on the mechanical properties. Area defects are between two grains or phases, where the lattice parameters are not fitting together. All these defects generate intrinsic stress. Depending on the height and the type of intrinsic stress (i.e. tensile or compressive), cracks or delamination effects can occur [25].

2.1.4 Optical Lithography

Optical lithography is one important process step to pattern thin films. In the semiconductor fabrication, this technique is used multiple times until a device is finished. The pattern to be transferred is written into a chrome layer on a flat quartz glass mask template. This mask is transparent for deep ultra violet (UV) light. If UV light irradiates the mask, the light is absorbed in those areas covered by the remaining chrome layer. The remaining light exposes an UV sensitive film or photo resist. The base component of such photo resists is a UV-sensitive polymer. The polymer changes its structure when exposed to UV radiation. Two basic types of photo resist exist, which are called positive and negative resist. Figure 2.4 shows the difference between both after development of the resists and etching of a thin film arranged below. The area of a positive

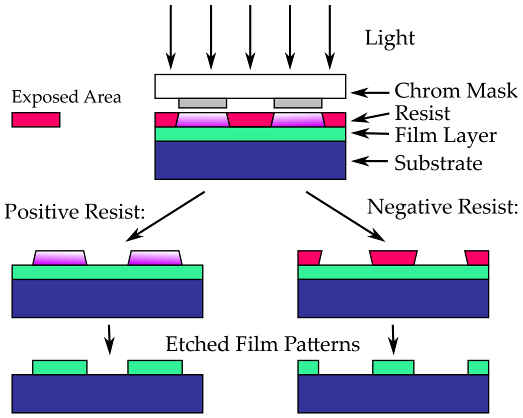

Figure 2.4: Schematically process flow with final structures if positive and negative resist are applied for etching of the thin film.

resist exposed to UV light changes its chemical structure and becomes soluble by the developer. Two families of positive resist exist, one of which is the one-component polymethylmethacrylate (PMMA) and the other the two-component so called DQN resist, which consists of a photoactive diazoquinone ester (DQ) and a phenolic novolak resin (N). In the PMMA resist the molecular chains are destroyed under deep UV light. These areas are then soluble, whereas the unexposed area are still insoluble. In DQN resists the DQ parts undergo a photolysis during UV exposure and produce cabene, which rearranges in so-called ketene, which are finally soluble. Negative resists consist of bis(aryl)azide and generate highly reactive nitrene upon photolysis. The nitrene undergoes several reactions so that a cross-linking of the reactant occurs. These cross-linked areas are then insoluble [18].

2.1.5 Lift-Off

An advanced patterning technique is the so-called *lift-off* process, where no additional etching of the thin film is needed. For this approach, a specific type of resist is needed, a so-called image reversal resist, such as *AZ 5214E* from MicroChemicals. In Figure 2.5, the most important process steps are illustrated. After cleaning of the substrate surface the resist is deposited through a spin-on process on top of the surface. If the resist does not adhere sufficiently, hexamethyldiszilane (HDMS) can be used as an adhesion promoter. With 4000 rpm a typical resist thickness of 1.4 µm is achieved. Afterwards, a pre-bake step is needed to vaporize the solvent in the resist film. The temperature for this step is in the range between 100 °C and 110 °C for several minutes. Subsequently, the resist is exposed to UV light through a mask for several seconds (see Figure 2.5a). Due to shadowing effects during the exposure, the flanks are not perfectly perpendicular to the surface. Depending on the desired slope of the side walls and the surface material property such as the reflectivity the exposure time is adapted. The resist gets soluble in these areas exposed to UV-light, which has now the same side wall characteristics than a positive resist.

The most critical step is the reversal bake step, which is around 120 °C for several minutes. The previously exposed areas undergo an additional cross-linking modification so that these areas are no longer soluble. The time for the reversal bake step should not be longer than necessary, because the temperature affects also these areas not being exposed to UV light before. The next step is a flood exposure of the resist with UV light without using a mask. With this step the previously not exposed areas

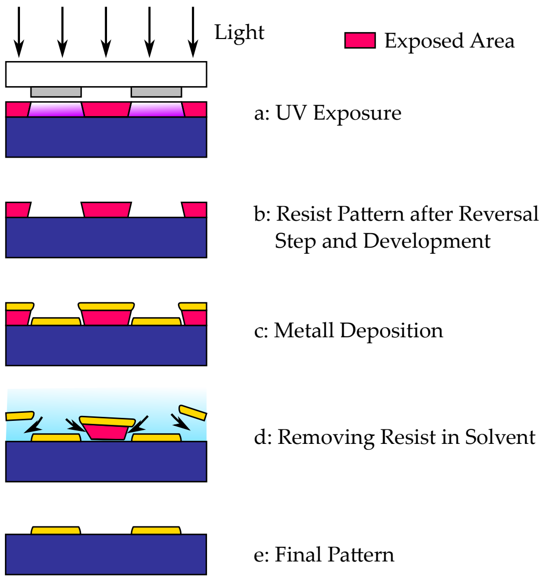

Figure 2.5: Typical process steps during a *lift-off* procedure.

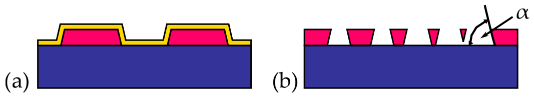

Figure 2.6: Typical problems arising either with positive (a) or negative (b) flank characteristics.

become soluble. A standard developer, for example *AZ 726* from MicroChemicals, can be used to dissolve the soluble areas, resulting in the final patterns (Figure 2.5b). After depositing of the desired material by evaporation or sputtering technique (Figure 2.5c), the resist is dissolved with a solvent like acetone so that the deposited material on top of the resist is removed (Figure 2.5d), thus leaving the desired pattern on the surface (Figure 2.5e) [18, 26].

The slope of the walls is a critical factor for the *lift-off* process, indicated by the angle α. If the walls, as illustrated in Figure 2.6a, feature positive flanks, the deposited material covers the resist completely and the solvent cannot attack the resist. This unwanted behavior occurs when the first exposure was too long. For the so-called negative flank characteristics, other problems emerge in the case, when two walls are too close to each other. Then the contact area between resist and surface becomes so small that both side walls touch as indicated in Figure 2.6b, and the whole resist is removed. To avoid such behavior the side wall angle α of the slope can be increased, with the parasitic effect that parts of the side wall area will be coated. Another method is to reduce the total thickness of the resist. This can be achieved by choosing higher spin-on speeds or by adding a thinner, for example *AR 300*, to the resist. As a consequence, a carefully selected trade-off between the slope of the side walls and the total resist thickness has to be chosen for each lift-off scenario.

2.1.6 Etching

Etching comprises techniques to remove material from a surface with either a chemical or physical approach or a mixture of both. Depending on the used method and reactants, the etching of different materials can be very selective. Basically, etching itself is divided into dry and wet chemical processes, which are explained shortly in the following. A comprehensive overview of etch rates for different methods and materials is published by Williams *et al.* [27].

Dry Etching

Dry etching process is a method to remove solid material in a gas or vapor atmosphere. For purely physical etching, high energy ions are accelerated by an applied electrical field towards the substrate. Due to the transfer of kinetic energy upon impact, atoms from the surface are knocked out. Consequently, the process is not highly selective to different materials. Purely chemical etching on the other hand uses chemical reactions between etchant and the material to be removed. In contrast, this process is very selective with respect to different materials, as the kinetic energy transfer is low [18]. After the etch attack, the vaporized reaction products are removed by a pumping system. In this work, the combination of both, reactive ion etching (RIE) and a purely physical procedure, namely the inverse sputter etching (ISE) are used.

Reactive Ion Etching

During reactive ion etching (RIE), the ion bombardment damages the surface resulting in weakened or destroyed molecular bonds. As a result, the surface is consequently more reactive towards chemical attacks by the reactive species from the gas atmosphere. Depending on the material to be removed, fluorine or chlorine based reactive gases are typically used. The selectivity and anisotropy of the etching can be adjusted by the energy of the ions during bombardment and the chemical reactants [18].

Inverse Sputter Etching

The inverse sputter etch (ISE) process is a pure physical etching and cleaning process of the surface. Ar^+ ions are generated in a plasma and accelerated towards the surface. Through a transfer of kinetic energy, surface atoms are removed. Doing so, the surface may also get damaged during this cleaning step. This method has only very poor etch selectivity between different materials. Additionally, a surface-near implantation of the ions can occur, if the kinetic energy of the ions is too high. The advantage of this approach is that the surface of the substrate can be cleaned *in situ* without breaking the vacuum prior to the sputter deposition of the thin film material. Therefore, most commercially available sputter machines are equipped with ISE etching systems for cleaning purposes [18].

Wet Chemical Etching

Wet chemical etching is a technique to remove a material from a solid surface in a liquid environment, thus being typically highly selective to different materials. The process involves in most cases multiple chemical reactions that consume the original reactants resulting in the corresponding reaction products. The etching itself can be generally described by the following main steps [18]:

1. diffusion of the etchant to the surface

2. reaction between the etchant and the material to be removed

3. diffusion of the byproducts from the reacted surface

Typically chemical etching is isotropic, leading to large under etch when etching thick films. Some etchants offer different etch rates depending on the exposed crystallographic face. Seidel *et al.* showed that potassium hydroxide (KOH) etches the <100> direction 400 times faster than the <111> direction of a single crystalline silicon wafer [28].

2.2 Experimental Methods

2.2.1 Mechanical Stress in Thin Layers

The knowledge of the residual stress inside of deposited thin films is very important when integrating into MEMS devices. High tensile stress values usually result in cracks, whereas high compressive stress leads to delamination of the thin film [29, 30]. The total stress in a deposited thin film can be expressed by:

$$\sigma_{tot} = \sigma_{th} + \sigma_{int} + \sigma_{ext}, \tag{2.1}$$

where σ_{tot} is the total, σ_{th} the thermally induced, σ_{int} the intrinsic and σ_{ext} the externally applied stress component. The origin for thermally induced stress has several origins. Firstly, due to the difference in the temperature coefficients of expansion between two different materials (e.g. layers or between layer and substrate) and secondly due to a difference in the sample temperature during deposition and the temperature during observation, if the materials are in the elastic deformation range. Furthermore, stress is generated in a material of a homogeneous crystal structure, which is exposed to a thermal temperature gradient or in a structure with inhomogeneous thermal expansion coefficients to a uniform temperature change. The intrinsic stress reflects the internal structure of the material and depends on the thickness, deposition rate, deposition temperature, lattice mismatch or incorporation of impurities [18, 31]. For example, the energy of the deposited atoms has a direct effect on the surface mobility of adatoms, where a low surface mobility results in an enhanced pinning probability of atoms next the impact site resulting in a defect-rich microstructure. With higher energy, the atoms are able to move easily across the surface, thus increasing the probability to find an energetically preferable lattice site. In thin films the intrinsic stress is either compressive ($\sigma_{int} < 0$) or tensile ($\sigma_{int} > 0$). In the following some factors causing intrinsic stress are listed [18]:

- Doping ($\sigma_{int} < 0$ or $\sigma_{int} > 0$) can cause both compressive and tensile stress. If the radius of the dopant atoms is larger compared to the doped material (e.g. phosphor in silicon) the resulting stress is compressive, whereas dopants with a smaller atom radius result in tensile stress (e.g. boron in silicon).
- Atomic peening ($\sigma_{int} < 0$), which is for example ion bombardment by the sputter process, densifies the deposited thin film and results in compressive stress.

- Microvoids ($\sigma_{int} > 0$) may be generated, when ad-atoms are not able to overcome the surface topography during the deposition process due to a low surface mobility.
- Gas inclusions ($\sigma_{int} < 0$) occur, when gas molecules (e.g. hydrogen during Si_3N_4 deposition with a CVD process) are trapped.

Finally, externally stress is applied for example by mechanical bending of the material. Assuming that a thin film leads to a bending of a substrate, the residual stress can be determined by measuring the curvature. Basically, if the substrate is flat without a thin film, tensile stress results in a concave and compressive stress in a convex curvature. Since most wafers are not inherently flat, but feature some initial bow. The change in curvature before and after thin film deposition has to be evaluated. A commonly and commercially available technique is to measure the curvature with an interferometer or with a capacitive system. As a result a mean stress value integrated over the whole wafer is determined [18, 32, 33].

In this work, an equipment from E+H (MX203) was used. This technique uses two heavy plates mounted parallel to each other. 15 capacitive distance sensors are embedded in the plates to measures the curvature of a 100 mm wafer. The sensors are homogeneously distributed over the whole area to evaluate the stress of the layer in two directions. The residual stress itself is calculated by the Stoney equation:

$$\sigma = \frac{1}{R}\frac{E}{6(1-\nu)}\frac{T_{sub}^2}{t_l} \tag{2.2}$$

where R is the measured radius of the curvature, $\frac{E}{1-\nu}$ the biaxial modulus of the substrate, T_{sub} the thickness of the substrate and t_l the thickness of the deposited thin film, respectively.

2.2.2 Scanning Electron Microscopy

Scanning **E**lectron **M**icroscopy (SEM) uses high voltages up to several kV to accelerate and to focus an electron beam from an electron emitter toward the sample. The electron beam is scanning line by line over a defined area. The electrons interact with the sample surface up to a depth of about 1 µm depending predominantly on the accelerated voltage, thus back-scattering or emitting electrons and also X-ray radiation. Due to this interaction, several different detectors provide an image of the sample surface or in the case of X-rays chemical informations. The lateral resolution of such measurements depends on the penetration depth of the beam and the area of interaction (which is related to the magnification). Secondary electrons (SE) are emitted from very close to the surface and are used to analyze the topography of the sample. Back-scattered electrons (BSE) are those electrons from the beam that are reflected in volume that is located deeper in the sample. An image generated from mapping based on BSE feature a reduced lateral resolution compared to that gained from SE, but the intensity of the BSE signal is strongly related to the atomic number of the analyzed material and hence, can be used to analyze the local distribution of different sample elements [34]. In this work an SEM from Hitachi (SU8030) with an acceleration voltage of 5 kV with a current of 2 µA was used.

2.2.3 Transmission Electron Microscopy

Transmission **E**lectron **M**icroscopy (TEM) is another important analysis technique based on an electron beam. Given a lateral image resolution down to the Ångström range, even the distances of the atomic lattice can be measured. A disadvantage of this method is that an electron-transparent sample has to be prepared, so that it needs to have a thickness of around 100 nm. The electrons are accelerated by voltages up to 200 kV. The detection and imaging is done by a fluorescent screen or a CCD camera. The focus can be adjusted by using an electromagnetic lens system. Depending on the focal plane, an image or diffraction pattern can be seen [35]. For high-resolution images, an equipment from FEI (TECNAI F20) with 200 kV and 20 mA was used in this thesis.

2.2.4 Atomic Force Microscopy

Atomic **F**orce **M**icroscopy (AFM) is a standard approach to measure and analyze surface-related features as the topography or morphology. A tip with diameter of few nm is fixed to a cantilever. The bending characteristic of the cantilever depends on the interaction between the tip and the surface, which reveals the relative height of the sample [36]. With several line scan measurements an image of the surface is generated with a lateral resolution even in the atomic range. The two standard measurement modes for topography are *contact mode* and *tapping mode*. In *contact mode*, the tip will remain in constant contact with the surface, whereas in *tapping mode* the cantilever is oscillating in some distance to the surface. During a line scan in *contact mode*, the cantilever deflection is kept constant by moving the cantilever perpendicular to the surface thus generating a map of the surface topology. In *tapping mode* the amplitude of the oscillation is kept constant, resulting in a similar closed loop control. The deflection of the cantilever is measured by the position of a reflected laser beam on a four-segment diode [37]. In this work an equipment from Bruker (Dimension Edge) with a RTSPA tip at 300 KHz was used.

2.2.5 X-Ray Diffraction

X-Ray Diffraction (XRD) is used to measure lattice parameters like lattice plane distances or the crystallographic lattice structure, but also textures or residual stress. The advantage of such measurement method is that the preparation is fast, simple and non-destructive. The method makes use of constructive interference from patterns obtained from diffracted X-rays at atomic lattice planes. Positive interference appears when the traveling path is a multiple integer n of the wavelength λ of the X-ray. The condition is called Bragg-Brentano law and described in the following equation:

$$2d_{lattice}\, sin\theta = n\lambda \tag{2.3}$$

where $d_{lattice}$ is the distance between two atomic layers. The peak position and the width of the XRD measurement contain additional information about the average grain size d_{grain} normal to the surface. By using the Scherrer equation d_{grain} can be calculated according to [38]:

$$d_{grain} = \frac{\lambda}{b_{XRD}\, cos\theta} \tag{2.4}$$

where θ is the peak position and b_{XRD} the integrated width of the peak. In the following Figure 2.7a the angles between source, sample and detector are defined. ψ is the tilt of the sample and is kept constant and ϕ is the rotation angle. To measure the <002> peak of AlN, ψ has to be zero. In the Bragg-Brentano setup only the lattice planes parallel to the surface can be measured, see Figure 2.7b. It is a special configuration of the $\omega - 2\theta$ scan with $\omega = \theta$. To measure the misalignment of the grains (i.e. to analyze the angle of the grains with respect to the surface normal), this straight-forward measurement approach needs to be expanded, resulting in is the so-called *rocking curve* or ω-mode. In this configuration, the 2θ value is kept constant. If several ω scans with different 2θ values are made, a reciprocal space mapping can be generated. The position

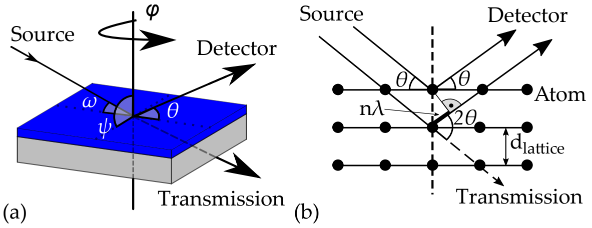

Figure 2.7: Definition of the angle between source, sample and detector (a), Bragg-Brentano configuration with incoming wave angle $\theta = \omega$ (b).

of each point in the reciprocal space is calculated according to the following equations [39]:

$$q_{\parallel} = \frac{1}{\lambda}\left(cos(2\theta - \omega) - cos(\omega)\right) \tag{2.5}$$

$$q_{\perp} = \frac{1}{\lambda}\left(sin(2\theta - \omega) + sin(\omega)\right) \tag{2.6}$$

If the values in the reciprocal space are integrated radially across the whole range, the result is equal to an $\omega - 2\theta$ scan. The XRD analysis in this work were done by a PANalytical X'Pert Pro Bragg-Brentano and a PANanalytical Empyrean system. The source was operated at 40 kV and 40 mA. The source emits CuK_{α} X-rays with $\lambda_1 = 1.5406$Å and $\lambda_2 = 1.5444$Å. In the Empyrean equipment the $CuK_{\alpha 2}$ line was filtered out by mono-crystalline graphite.

In this thesis, Bragg-Brentano measurements were also done at elevated temperatures. A PANalytical X'Pert Pro equipment with a heating chamber (HT1200 from Anton Paar) was used. The sample was heated up to 1000 °C., whereas small windows in the chamber enable the X-ray exposure of the sample. Additionally, the atmosphere of nitrogen or oxygen in the measurement chamber was controlled by a constant gas flow of around 100 sccm, thus mimicking harsh environmental conditions for the evaluation of key materials.

2.2.6 Piezometer

The piezoelectric effect is a property of certain materials to transform electrical into mechanical energy and *vice versa*. A material is piezoelectric if the atomic lattice is non-centrosymmetric. If this condition is fulfilled and the material is an isolator, an electrical charge can be measured if mechanical strain is applied to the lattice (direct piezoelectric effect). The indirect or inverse piezoelectric effect describes the mechanical deformation of the lattice due to an external applied electrical field. Two equations are necessary to describe the mechanical and electrical behavior. Equation 2.7 gives the correlation between the mechanical strain S_i and the electrical field E_m and equation 2.8 that for the inverse piezoelectric effect, linking the dielectric charge density D_m with the mechanical stress T_j through the piezoelectric constant d_{mi} [40, 41]:

$$S_i = s_{ij}^E T_j + d_{mi} E_m \tag{2.7}$$

$$D_m = d_{mj} T_j + e_{mn}^T E_n \tag{2.8}$$

with the elasticity tensor s_{ij} and the dielectric tensor e_{mn}. These equations are written using the Voigt notation [42]. Piezoelectric AlN features the hexagonal wurtzite lattice and is described by the following piezoelectric tensor :

$$d_{ij} = \left\{ \begin{matrix} 0 & 0 & 0 & 0 & d_{15} & 0 \\ 0 & 0 & 0 & d_{24} & 0 & 0 \\ d_{31} & d_{32} & d_{33} & 0 & 0 & 0 \end{matrix} \right\} \tag{2.9}$$

with $d_{31} = d_{32}$ and $d_{15} = d_{24}$ [43]. For thin film MEMS applications, the piezoelectric constant d_{33} and d_{31} are important. The parameter unit is either in pm/V or pC/N. The unit pm/V is for the inverse and pC/N for the direct piezoelectric effect. The first index of d indicates the direction of the polarization generated by an electric field. The second index is the direction of the applied stress or induced strain. A method to determine the piezoelectric constant uses the Berlincourt approach [44]. With a commercial equipment PiezoTest PM300, a fast characterization of the piezoelectric material is possible. Contact areas on both sides of the piezoelectric layer are needed to measure d_{33}. Therefore, pads with a diameter of 1000 µm were deposited on top of the AlN layer. The second electrode is the silicon substrate itself. First, the native oxide on the backside of the silicon substrate was removed. Next, as an electrode material consisting of a bi-layer of 10 nm titanium and 50 nm platinum for an enhanced electrical contact was sputter-deposited. During the measurement procedure the contact pads are clamped between two needles with a constant force of 1 N. Additionally, an AC force of 0.25 N at 110 Hz is applied. The measured area is defined by the contact area of the needles, which both have a curvature radius of 500 µm. With this applied force an electrical charge is generated, according to the following equation 2.10:

$$Q = \int_{A_Q} d_{33} T \, dA = d_{33} T \, A_Q = d_{33} \, F \tag{2.10}$$

The generated electrical charge is compared with that provided from a reference sample with known d_{33} value. The electrical field, however, induces in the piezoelectric material a lateral force and hence, a lateral bending, leading to an influence of d_{31} on the measured d_{33} value [45–47]. The equation 2.11 allows an estimation of the piezoelectric value d_{31} [48]:

$$d_{33} + 2d_{31} = 0 \tag{2.11}$$

Reactively sputtered AlN used in this work, was already investigated by Schneider *et. al*, which showed a relation of [49]

$$d_{31} = -0.39 \cdot d_{33} \tag{2.12}$$

Based on this knowledge, only the d_{33} value was measured in this thesis.

2.2.7 Electrical Characterization

Leakage Current Mechanisms

The charge transport mechanism in dielectric thin layers can be determined by measuring the dependency of the leakage current density J of both temperature and of the applied electrical field E. There are several typical mechanisms, which can appear in thin films like Ohmic, ionic, tunneling, Schottky and Poole-Frenkel. In the following the different mechanisms are summarized listing their most important features.

Ionic and Ohmic Transport

Basically, the ionic charge transportation can be compared with a diffusion process. Mobile ions are traveling through the material driven by an external electrical field. The current decreases over time, because there is no injection of new ions into the layer. The ionic transport mechanism can be described by [50]:

$$J \propto \frac{E}{T_M} exp[-E_a/k_B T_M] \tag{2.13}$$

with the activation energy E_a, Boltzmann constant k_B and temperature during measurement T_M [50]. The mechanism is quite similar to ohmic conduction:

$$J \propto E\, exp[-E_a/k_B T_M] \tag{2.14}$$

Tunneling

Tunneling is the most important mechanism through very thin insulators (several nm) under high electrical fields. Tunneling is explained in the frame of quantum mechanics as the electron wave function penetrates a thin potential barrier under a strong external electric field. From pure theory the mechanism is independent of temperature and can be described by [50]:

$$J \propto E^2 exp\left[-\frac{4\sqrt{2m^*}(q\phi_B)^{3/2}}{3q\hbar E}\right] \tag{2.15}$$

with the effective mass m^*, barrier height ϕ_B, Dirac constant $\hbar$ and the elementary charge q.

Schottky emission

The Schottky effect describes the reduction of the metal-insulator barrier height when applying an electrical field. With a lower barrier height, more electrons are injected into the insulator. The current density can be calculated by [50]:

$$J \propto A^* {T_M}^2 exp\left[-\frac{q\left(\phi_B - \sqrt{qE/4\pi\epsilon}\right)}{k_B T_M}\right] \tag{2.16}$$

with the Richardson constant A^*.

Poole-Frenkel emission

Poole-Frenkel mechanism is due to the emission of trapped electrons into the conduction band of the electrode. The supply of electrons from traps is through thermal excitation. In this case the barrier height is the depth of the trap. The effect is increased by applying an electrical field, because with a higher field the trap barrier height is decreased. In addition, the effect is more dominant at higher temperatures. The current density is described by [50]:

$$J \propto E\, exp\left[-\frac{q(\phi_B - \sqrt{E/\pi\epsilon})}{k_B T_M}\right]. \tag{2.17}$$

The current density for each applied electrical field can be arranged in an Arrhenius plot enabling to extract the activation energy $E_a = -q(\phi_B - \sqrt{E/\pi\epsilon})$. Next, the electron barrier height can be determined by fitting the measured activation energy with the formula from equation 2.17. The AlN investigated in this work is a dielectric material with piezoelectric properties. Schneider *et al.* showed that the main electric transport mechanism is ohmic at electrical fields < 0.1 MV/cm and dominated by Poole-Frenkel emission at > 0.3 MV/cm independent of temperature up to 300 °C [51].

Four Wire Measurements

In this work, the resistance is measured with a Keithley 2400 source measurement unit and a Keithley 3706A system switch with integrated digital multimeter using the integrated four-wire measurement technique. The four-wire measurement method or Kelvin sensing is a technique to make more accurate measurements than with two-wire sensing technique. A constant current is applied to the sample with two wires. The voltage drop at the sample is measured with two independent wires, so that the error generated by the wire resistance are negligible. The measurement current are between 10 µA up to 100 µA to avoid any damage of the sample.

3 ALUMINUM NITRIDE

Parts of this chapter have been published in [29, 52, 53]

3.1 Basic Information

In the year 1880 the piezoelectric effect was found by the Curie brothers. The direct effect is based on the generation of electrical polarization charges due to mechanical deformation [54]. The indirect effect is the mechanical deformation caused by applying an electrical field. Nowadays both effects are utilized in micro electro-mechanical systems for sensor or actuator applications [55].

Aluminum **N**itride (AlN) is a group III-V material. Depending on the fabrication condition, AlN can be deposited in cubic or wurtzite crystalline structure. The cubic phase does not feature piezoelectric properties and is mainly used for hard coatings (e.g. for cutting tools or drilling applications) [56]. The wurtzite phase provides the piezoelectric effect and hence, is beneficial for implementation into MEMS sensors and actuators. But, the piezoelectric coefficient d_{33} being an important parameter for MEMS is lower compared to other materials like PZT (lead ziconate titanate). The d_{33} value of AlN is about 6.5 pm/V, whereas it is about 215-575 pm/V for PZT [57]. Under proper deposition conditions, AlN thin films feature piezoelectric properties in the *as deposited* state. It is an advantage compared to PZT, where a post process step is needed to polarize the layer. A major advantage of AlN is the CMOS (**C**omplementary **M**etal **O**xide **S**emi-conductor) compatibility, which allows the integration of AlN thin films in MEMS production lines with moderate effort [58]. A more detailed influence of the sputter parameter on the AlN quality is given in the work of Ababneh *et al.* [59]. The disadvantage of the low piezoelectric constant d_{33} can be mitigated by doping the layer with scandium, which increases the value up to about 19 pm/V [60]. Furthermore, pure aluminum nitride has a high electrical resistance due to its wide band-gab of 6.2 eV, good thermal conductivity of ~300 W/m·K, chemical resistance and a high

Table 3.1: Material-related properties of monocrystalline AlN.

Property	Value	Reference
Density ρ (single crystal)	3.255 g/cm^2	[64]
Piezoelectric constant d_{33}	6.5 pm/V	[59]
Dielectric permittivity ϵ_r	10	[65]
Thermal conductivity λ_h	~300 W/mK	[61]
Hardness H	16.2 GPa	[66]
Bandgap	6.2 eV	[64]
Young's Modulus Y	225 GPa	[66]
Melting Point	~2700 °C	[63]

melting point of ~2700 °C [61–63].

Important material parameters of monocrystalline AlN are listed in Table 3.1.

In opto-electronic applications, monocrystalline AlN thin films are nowadays e.g. used as nucleation layer for gallium nitride GaN based photo detectors or on rhodium for UV mirrors [58, 67, 68]. In MEMS devices, AlN is often integrated in its polycrystalline form in gyroscopes, microphones or cantilever devices for density/viscosity sensing liquids or as ultra-precise mass sensor [69–73]. For high temperature applications, the layer is beneficial in hydrogen sensors up to 300 °C and in a strain gauge operating at elevated temperatures up to 1000 °C [74, 75]. In combination with sapphire substrates, SAW devices with high phase velocities were realized [76]. Both materials promise high temperature stability and are therefore well suited for operation in harsh environments [77].

A commonly used technique to deposit AlN is reactive DC sputtering in pure nitrogen or mixed nitrogen/argon atmosphere. With this technique, AlN is deposited with good piezoelectric properties on a large variety of different substrate materials such as silicon or even on glass ceramics (e.g. LTCC) at deposition temperatures below 150 °C [65, 78, 79]. As a consequence, it is possible to deposit this active layer material above other temperature sensitive systems. Despite this moderate deposition temperatures many application scenarios request a high temperature stability even in chemically aggressive environmental being targeted in this thesis. The deposition parameters for

Table 3.2: Sputter parameters for AlN thin film synthetization

Parameter	Value
Target	100% Al
Purity	5N
Target Ø	150 mm
Power	800 W
N_2 flow	60 sccm
Back pressure	2 µbar
Target distance	65 mm
Deposition rate	0.44 nm/s

AlN thin films used in this work are summarized in Table 3.2.

To analyze the mechanical and electrical properties, two different methods of sample preparation for different gas atmospheres and temperatures were used. The first method is based on a full 100 mm wafer process, because the measurement equipment to determine the intrinsic stress needs a full wafer. The second method is based on small sample with an area with outer dimension of 12x12 mm². To have a good comparability between each analysis, the samples were used only for one analysis (e.g. leakage current, XRD etc.), but from the same wafer. Hence, the samples were annealed and afterwards electrodes were realized, if needed.

3.2 Microstructural and Mechanical Properties

In the following section, the mechanical properties of the deposited AlN thin films are investigated. An important property of the deposited AlN layer is the uniformity of the c-axis orientated AlN grains. Therefore, two different pre-conditioning procedures of the substrate surface are performed and evaluated. An additional important parameter is the residual intrinsic stress of the deposited thin film. High tensile stress values can cause cracks, whereas high compressive stress values may result in delamination effects, both of which degenerate the device performance.

3.2.1 Pre-treatment of the Substrate Surface

To improve the c-axis orientation of the AlN layer, two different surface modification methods of the substrate prior to sputtering were investigated. Sapphire was chosen as robust substrate targeting the fabrication of high temperature SAW sensors in the next step (see chapter 5). By the first method, the substrate surface was subsequently cleaned in isopropanol and acetone ultrasonic baths for 5 minutes each. By the second method, an ISE step at 500 W for 5 minutes in pure argon atmosphere at a pressure of 6 µbar was performed prior to deposition of the AlN thin film layer, without breaking the vacuum condition in the sputter deposition chamber.

Figure 3.1 shows high-resolution TEM (HRTEM) cross-section images of samples pre-conditioned in an ultrasonic bath (a) and with an ISE process (b). For the ultrasonic sample, the first 2-3 nm of the AlN thin film close to the sapphire substrate have a fine polycrystalline structure. Basically, the interface stays almost unaffected what is in contrast, to the second approach, where the sapphire substrate becomes amorphous, due to the ion bombardment during ISE treatment. The penetration depth of about 3-5 nm of the amorphorised surface-near layer is in good agreement with the stopping range of ions in matter simulations using the tool SRIM from Ziegler *et al.* with a reasonable argon energy of 1.5 keV [80]. Figure 3.2 shows the simulated Ar^+ ions pen-

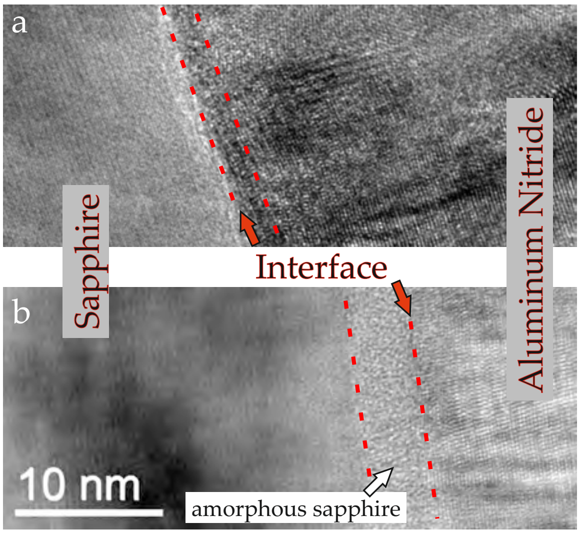

Figure 3.1: High-resolution TEM images of the interface between sapphire and aluminum nitride layer applying either an ultrasonic bath (a) or ISE (b) before AlN deposition.

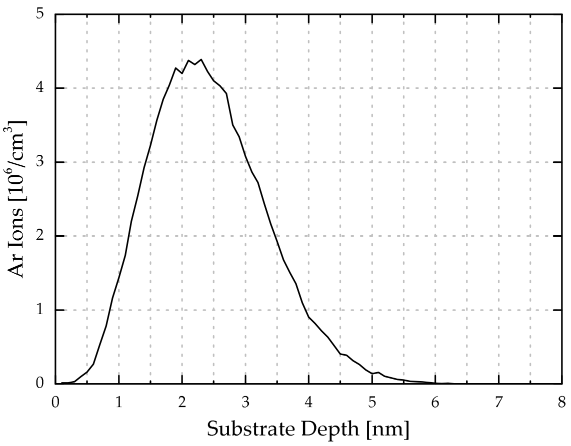

Figure 3.2: Simulation of Ar^+ ion distribution with an acceleration energy of 1.5 keV in a sapphire substrate using the SRIM tool [80].

etration distribution in the sapphire substrate. This generated amorphous layer inside the substrate is clearly visible in Figure 3.1b. The AlN film itself growths in a highly ordered crystalline microstructure from the substrate interface. By applying this pretreatment, Schneider *et al.* achieved on silicon substrate an increase in d_{33} by about 20% compared to a pure hydrogen fluoride *HF* dip for surface cleaning purposes [49]. As on silicon, the reason for the beneficial growth characteristic is the significantly increased structural defect density associated with the amorphorised sapphire surface, which provides a large number of nucleation sites for the subsequent AlN deposition compared to the almost featureless surface characteristics after ultrasonic cleaning due to the high sapphire substrate quality.

For a more in-depth analysis of the crystalline structure of the samples shown in Figure 3.1, diffraction patterns at different positions in distances of 40 nm and 400 nm from the interface were recorded for both sample types, as illustrated in Figure 3.3. For the ultrasonic sample the measurement at about 40 nm from the AlN/sapphire interface shows that the AlN grains are not perfectly aligned (see Fig. 3.3a), which is in good agreement with the observations in Figure 3.1a. When moving to a position 400 nm from the interface into the AlN layer film, the grains are showing an increased misalignment, due to the presence of many points with a blurred characteristics in the diffraction pattern, as shown in Figure 3.3b. Given this result, it cannot be completely excluded that other crystallographic phases are present. With the ISE

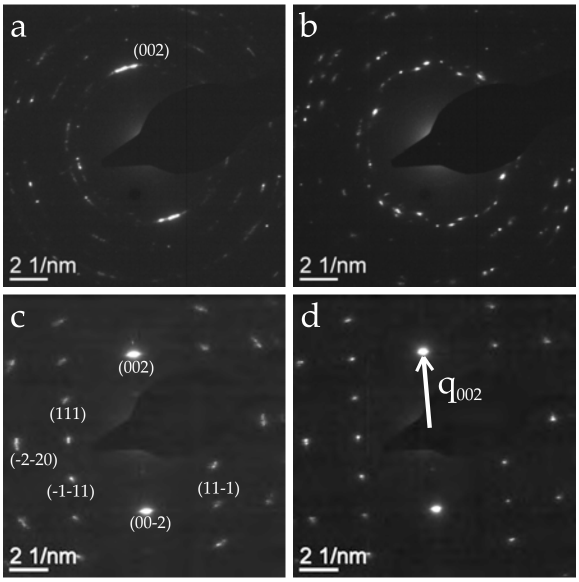

Figure 3.3: Diffraction patterns of the AlN thin film taken from the ultrasonic sample at 40 nm (a) and at 400 nm (b) from the interface compared to the sample with ISE pre-treatment at 40 nm with the main lattice planes (c) and at 400 nm (d).

process, the interface-near microstructure of the AlN film is completely different. Due to the amorphization of the sapphire surface, more nucleation sites are offered in the early stage of film growth without any impact that may arise from the substrate lattice and hence, the layer can grow more uniform, as seen in Figure 3.3c. Furthermore, with increasing thickness the AlN <002> crystallographic direction becomes more c-axis oriented leading to reduced diameter in the spot size and a sharp edge characteristics in the diffraction pattern (see Fig. 3.3d).

Figure 3.4(a) shows XRD measurements in Bragg-Brentano configurations of samples being either pre-treated with an ultrasonic or with the ISE process. The measured AlN (002) peak position is at about 36.1° , although this parameter is slightly shifted to lower values for the ultrasonic sample compared to the ISE pre-treated sample. The literature value of the peak position extracted from the powder diffraction file PDF is at 36.0401°. The determined *Full Width at Half Maximum* (FWHM) of the AlN (002) peak is 0.30° for the ultrasonic and 0.19° for the ISE sample. The FWHM is an indicator of the grain size and the uniformity of the lattice distances parallel to the surface. A lower value indicates the presence of larger grains and lower deviations from the parameters expected from a monocrystalline sample. Additionally, a second peak is

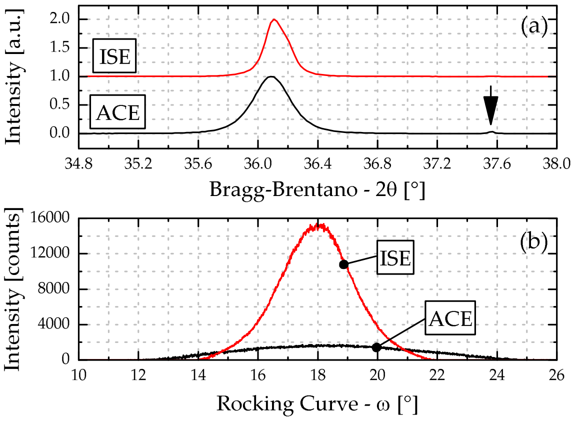

Figure 3.4: XRD measurements in Bragg-Brentano mode (a) and the corresponding rocking curves (b) for the samples cleaned in ultrasonic bath (black) and ISE process (red).

measured at 37.55° for the ultrasonic sample, indicated with an arrow. This peak originates most likely from the (111) orientation of the cubic or from the (101) orientation of the hexagonal lattice. The 2θ value deviates 0.23° and 0.36° from the powder diffraction value. The corresponding powder diffraction file (PDF) numbers are 00-025-1495 for the cubic and 00-025-1133 for the hexagonal system. This peak can also explain the additional diffraction spots in Figure 3.3b. It is reasonable to assume that without the ISE pre-treatment, local stress is generated by lattice mismatch between substrate and deposited film, leading to a pronounced growth in other crystallographic directions and hence, to a distorted c-axis orientation of the grains inside the deposited thin film. Similar behavior was reported by Pelleg *et al.* for TiN thin films [81]. Figure 3.5 shows a reciprocal space mapping measurement realized with a PANalytical Empyrean of the (002) AlN peak on top of silicon for a sample pre-treated with ISE. In this case the reflection from the (002) plane is more extended in $q_{\|}$-direction, what means that the grains are not uniformly aligned perpendicular to the surface along the measurement angle $\varphi = 0°$, which is in good agreement with Bragg-Brentano measurements. An angle of $\varphi = 0°$ corresponds to the $\langle 11\bar{2}0 \rangle$ direction of the sapphire substrate. The scatter in $q_{\perp}$ indicates a variation of the atomic lattice distances $d_{lattice}$ along the c-axis. To analyze the spatial alignment of the grains, the rocking curve method is used. The values for the rocking curve are extracted from reciprocal space mapping measurements, where the values are integrated between $\theta = 35°$ and $\theta = 37°$. Figure 3.4(b) shows the result

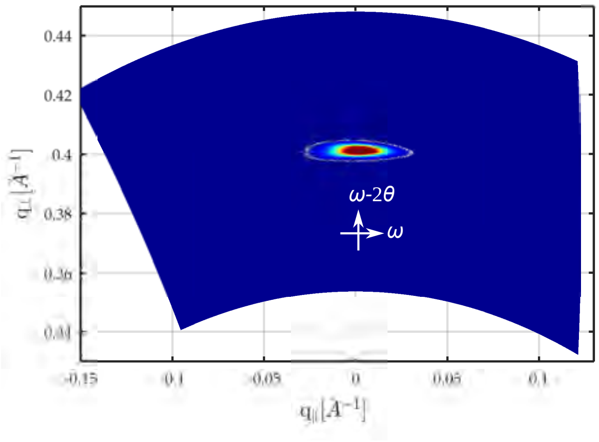

Figure 3.5: Reciprocal space map for the (002) peak of a 500 nm thin AlN layer on top of sapphire after an *in situ* ISE surface pre-treatment process.

of the intensity distribution $I(\omega)$ for both samples. The resulting angle between source and detector is fixed according to $\omega + \theta = 36.1°$. The value $\omega = 18°$ is equivalent to the angle of 36° in the Bragg-Brentano configuration. It can be seen, that the intensity for the ISE sample is much larger, which means that more (002) planes are arranged parallel to the surface.

To verify the assumption, that with the ISE pre-treatment no lattice information is transferred from the substrate into the deposited AlN layer, additional reciprocal space mapping measurements with $\varphi = 45°$ and 90° are performed. Figure 3.6 shows the extracted rocking curves from the reciprocal space for the ISE sample. The intensity is larger compared to these measurement results presented in Figure 3.4, because the component for generating the X-rays was replaced between both measurement cycles. Figure 3.6 exhibit the grain orientation distribution for different rotation angles φ. The intensity at a given angle ω in comparison to the peak position indicates the amount of different grain orientations. The measurements show that the grain orientation distribution is rotation symmetrically for all φ angles with respect to the c-axis direction. In addition, it can be seen, that the peak position differs slightly for each φ, which can be explained by the not perfectly prepared sample. For example, if the angle ψ is not zero, a rotation of the sample around φ causes a peak shift in the rocking curve. Overall, the *in situ* ISE pre-treatment of the surface has to be preferred, because the direction of the growing grains becomes more homogeneous and additionally gets better vertical aligned with respect to the substrate surface. A similar effect was observed by Schneider *et al.* on silicon substrates [65]. Therefore, all substrate surfaces were pre-treated

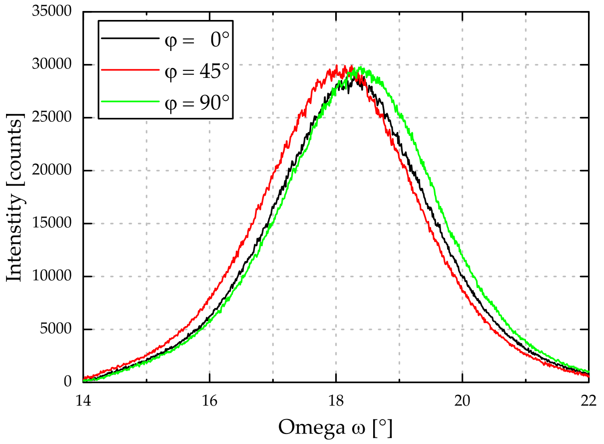

Figure 3.6: Rocking curves for the ISE process at different φ values.

with an ISE step prior to the AlN deposition.

3.2.2 Intrinsic, biaxial Stress

AlN samples with thicknesses between $h_{AlN} = 100$ nm and 2000 nm were deposited on silicon substrates, because the measurement equipment for film stress determination needs a conductive or at least semi-conductive material. Before the deposition process the bow of the silicon substrate was measured. After the deposition process, the bow of the wafer was measured again and the average stress was determined using the method explained in section 2.2.1.

Without Mechanical Stress Compensation during AlN Deposition

Figure 3.7 shows the average stress of AlN thin films sputter-deposited on 100 mm silicon wafers with respect to the layer thickness. The wafer was placed in the middle of molybdenum holder without any mechanical clamping of the substrate. With a layer thickness of $h_{AlN} = 100$ nm the film has a compressive stress of $\sigma_{avg} = -565$ MPa. When increasing the layer thickness the stress changes from compressive to tensile and shows a maximum of $\sigma_{avg} = +517$ MPa at $h_{AlN} = 1000$ nm. At $h_{AlN} = 1500$ nm, the formation of cracks is observed in the AlN layer, what results in the decrease of the average stress inside the layer due to relaxation effects. This characteristic can be explained with the Volmer-Weber (VW) growth mechanism, which is based on the grain growth behavior. The mechanism describes several steps [82]. At the beginning, the layer starts at several nucleation islands. These islands of the thin film feature compres-

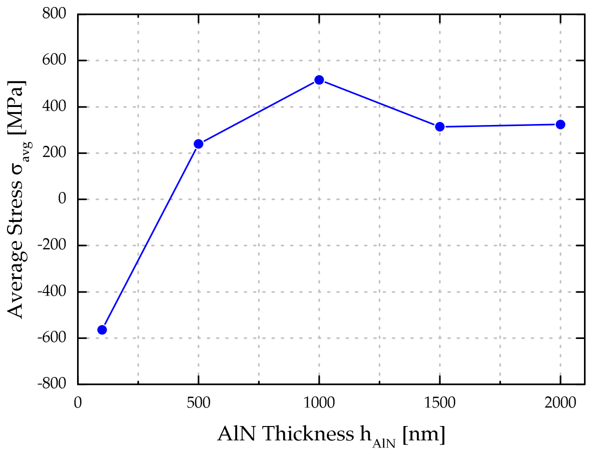

Figure 3.7: Influence of the sputtered AlN thickness on the intrinsic stress. Above 1000 nm with the presence of cracks the stress value drops. The inserted lines serves as guide to the eyes

sive stress due to imperfect crystalline microstructure of the deposited layer. Tensile stress starts to be generated, when the islands coalesce among each another. When the layer becomes thicker, relaxation mechanisms start to occur. One possible mechanism is that atoms diffuse into grain boundaries and generates compressive stress, due to the additional space needed by the atoms. A second mechanism may be inter facial shearing, where inside the crystal structure, different planes of the lattice or grain boundaries are shifted with respect to each other [82–84]. This shear mechanism leads to cracks in the layer. As a result, only AlN thicknesses ranging up to $h_{AlN} = 1000$ nm can be fabricated. A workaround to increase the total AlN layer thickness is to deposit sequential several thin AlN layers with a maximum layer thickness of 1 µm. In this work, between each sub-deposition step a dwell time of around 30-45 minutes is inserted to cool down the self-heated substrate. Figure 3.8(a) shows a TEM image of the interface between two deposited layers. The interface itself can clearly be detected. When analyzing an even higher resolution of the interface, the second layer grows directly in crystallographic c-axis orientation as seen in Figure 3.8(b). Related diffraction patterns for both layers just below and above the interface indicate this conclusion, which can be seen by the sharper and less blurred diffraction pattern. Due to the additional time caused by the dwell time during fabrication of a 2 µm thin AlN layer, an other approach with a tailored wafer holder is evaluated allowing a defined stress state of the wafer during AlN deposition by clamping. This approach will be explained in

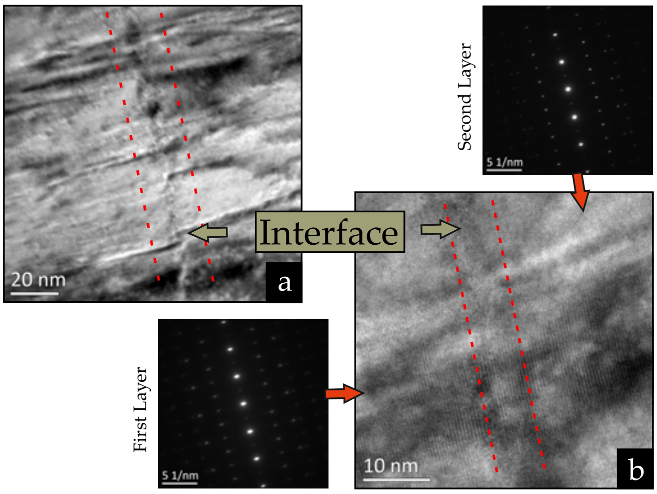

Figure 3.8: TEM images of the interface between AlN sublayers sputter deposited in direct sequence to each other (a). HRTEM image with the crystallographic planes showing the corresponding diffraction patterns of the two sublayers (b). The red lines indicate the interface area.

the following section.

Controlling the Layer Stress

To counterbalance the negative impact of too high tensile AlN stress and hence, the film failure due to crack formation, the wafer was clamped by a ring-shaped arrangement to a flat holder during deposition. Figure 3.9 shows a schematic of the wafer holder without (a) and with a clamping (b) system. It can clearly be seen that without a clamping system, the wafer bow before and during the position process is undefined. With the ring, which presses the wafer flat to the substrate holder, this clamping system leads to a specific bending of the wafer during the deposition process as well the substrate gets in good thermal connection to the holder. The holder material was aluminum because of the good heat capacity $c_p = 0.897$ J/gK and thermal conductivity $\lambda_h = 237$ W/m·K [17]. With these approach a defined self-heating of the substrate during deposition is ensured [85]. Figure 3.10 shows the average stress in the deposited layers as a function of their thickness. With this wafer clamping system even layer thicknesses up to 10 µm can be deposited without delamination effects of the AlN thin film. To verify the deviation of the stress values by clamping of the silicon wafer during the sputter deposition process, additional samples of selected layer thicknesses were fabricated. Due to the

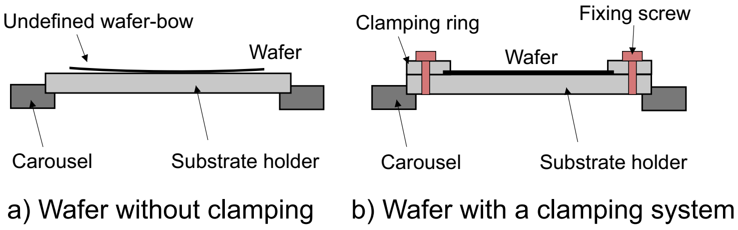

Figure 3.9: Schematics of the wafer status during the deposition process without (a) and with a clamping (b) system.

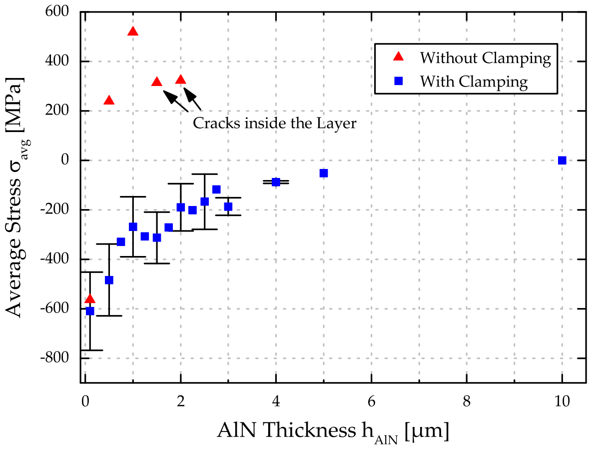

Figure 3.10: Average intrinsic stress of AlN thin films deposited on silicon with and without a clamped wafer configuration.

later target layer thicknesses for SAW devices, thicknesses of up to 4 µm were preferable selected. For a 100 nm thin layer the intrinsic stress starts at the same compressive stress value compared to a deposition without clamping. If the layer thickness is increased, the compressive stress decreases in the clamping configuration. Nevertheless, at thicknesses values of about 5 µm the layer still features compressive stress, compared to samples without clamping, where the sample already reaches tensile stress with a layer thickness of 500 nm. Also at $h_{AlN} = 10$ µm the stress remains at very low compressive values, only some cracks at the edge of the substrate wafer are observed. It is also likely, that with the clamping of the wafer, additional mechanical stress is induced during the deposition process, which leads to an overall compressive stress. For further analysis the temperature during the sputter process was evaluated, because the chamber and the holder are self-heated by the plasma. To measure the temperature of the wafer, a pyrometer was placed right below the holder. The pyrometer starts to

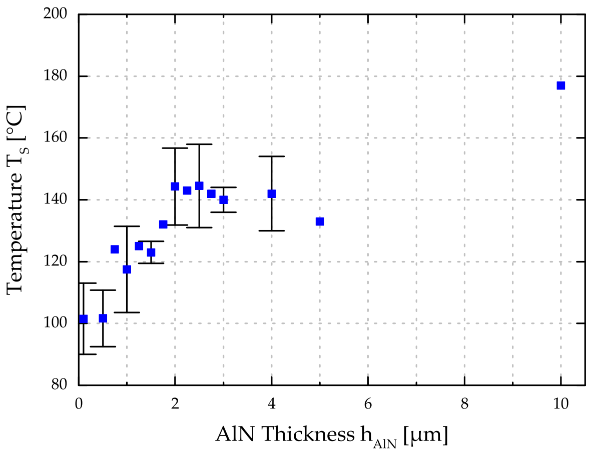

Figure 3.11: Substrate temperature at the end of the sputter process for different AlN thicknesses.

measure at around 90 °C and measures up to 850 °C. Figure 3.11 shows the holder temperature values at the end of the sputter process. With $h_{AlN} = 100$ nm the temperature is around 90-100 °C. For layer thicknesses of $h_{AlN} = 2$ µm the values is increased and in the range of 140-150 °C. If Figure 3.10 and Figure 3.11 are compared, it is indicated that with thicker AlN layers the compressive stress is reduced, while simultaneously the maximum substrate temperature increases. At first, it looks as if with increasing substrate temperature more tensile stress is generated. But an additional effect starts to occur with higher temperatures, as the holder including the clamping ring expand and the edge of the ring, where the silicon wafer is clamped, bends upwards. As a result, the clamping force is reduced and the substrate can slightly move and hence, the effect of the clamping decreases. Figure 3.12 shows the influence of intrinsic stress on the *lift-off* process used for pattering the electrode layer. It can be seen that with a tensile stress of +302 MPa, some regions of the wafer are still covered completely with the electrode material and hence, are not removed during the acetone dissolution step (see Fig. 3.12(a)). This negative impact is reduced if the intrinsic stress changes from tensile to compressive stress, which can be seen in Figure 3.12(b). With a compressive stress of -202 MPa the whole layer is well patterned across the wafer surface without any residuals (see Fig. 3.12(c)). It is reasonable to assume, that due to the tensile stress of the AlN layer, the UV light needed for the exposure gets scattered in an unwanted way, so that it is reflected inside the AlN layer. This in turn, leads to an exposure of resist in areas originally shadowed by the mask during the first UV exposure step of

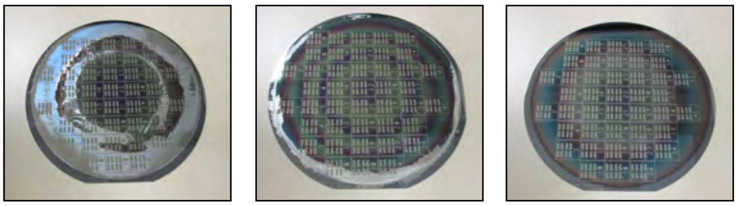

a) 302 MPa b) -90 MPa c) -202 MPa

Figure 3.12: Impact of the intrinsic stress with +302 MPa (a), -90 MPa (b) and -202 MPa (c) of a 1 µm thin AlN layer on the *lift-off* process of the electrode material.

the *lift-off* process and hence, the electrode material is not lifted in a all areas where the metallic film should be removed.

Therefore, to improve the approach with the clamping system, so that even thicker layers with compressive stress between -150 MPa and -300 MPa can be fabricated, other materials like tungsten ($\alpha = 4.5 \cdot 10^{-6}\ K^{-1}$) or molybdenum ($\alpha = 4.8 \cdot 10^{-6}\ K^{-1}$) are currently under test, as they both feature nearly the same linear thermal coefficients of expansion as silicon [17].

3.3 Investigations under Harsh Environmental Conditions

For operation of the AlN layer at elevated temperatures up to 1000 °C in different atmospheres such as vacuum, inert gasses like argon or nitrogen or even aggressive gasses like oxygen, additional investigations are performed. When enhancing the temperature loads, due to crystallographic and chemical modifications (e.g. diffusion of atoms inside the layer, or oxidation processes in an oxygen atmosphere) the electrical and mechanical properties of the thin film change. As a consequence, the AlN layer may lose its piezoelectricity, which would mean a failure of the device. Furthermore, if the intrinsic stress changes too much, delamination effects or cracks inside the layer can arise, which would destroy the device mechanically. For operation of AlN thin films under such challenging conditions, a maximum temperature has to be determined for each gas atmosphere separately before degeneration of the active thin film element lead to device failure. For this purpose, the impact of post-deposited annealing temperatures up to 1000 °C on the mechanical (i.e. intrinsic, biaxial stress), electrical (i.e. leakage current behavior), electro-mechanical (i.e. piezoelectric constant) properties were measured and correlated with the change in film morphology applying techniques such as XRD and AFM.

3.3.1 Intrinsic Stress

Especially for reliable operation, a constant or at least predictable intrinsic stress level is of utmost importance for key components in MEMS devices during high temperature loading. Therefore, AlN layers with thickness of $h_{AlN} = 100$ nm and 500 nm were selected as representatives for compressive and tensile stress values (see Figure 3.7). The samples were placed in an oxidation furnace for 2 hours. The temperature was increased in one step from room temperature 25 °C to 100 °C and subsequently up to 1000 °C in 100 °C steps. Between each annealing step the biaxial film stress was measured at room temperature. As annealing atmosphere, either 100 % nitrogen or 100 % oxygen at atmospheric pressure was chosen, with a constant gas flow of 100 sccm. Argon as an inert and reference gas could not be applied, because the used oxidation furnace for 100 mm wafers was not equipped to feed in this noble gas. Figure 3.13 shows the absolute change of the intrinsic stress influenced by both the temperature and the gas atmosphere. The absolute stress change σ_{avg} was determined according to $\sigma_{avg} = \sigma_{after\,annealing} - \sigma_{as\,deposited}$. Independent of the atmosphere the intrinsic film stress remains constant up to an annealing temperature $T_A = 600$ °C for all samples. After $T_A = 700$ °C, however a shift towards compressive stress is observed. This effect can be attributed to the diffusion of gaseous atoms (i.e. nitrogen or oxygen) into the AlN thin film. This additional atoms in the layer needs volume inside the atomic lattice leading to additional compressive stress. Basically, this diffusion-based effect is stronger for oxygen than for nitrogen. A reason is that an oxygen atom is bigger than nitrogen. Furthermore, oxygen has a higher chemical affinity to aluminum than nitrogen, leading to a replacement of nitrogen by oxygen. As a result, AlN oxidizes to an alumina compound, where an additional oxygen atom is needed for each two aluminum atoms to reach a stoichiometric composition. Lin *et al.* showed that AlN films oxidize in different modifications like the intermediate $\delta - Al_2O_3$ and the thermodynamically stable $\alpha - Al_2O_3$, when exceeding temperature of 850 °C [86]. The 100 nm thin AlN sample in oxygen atmosphere after the $T_A = 1000$ °C annealing step does not follow this trend. It is reasonable to assume, that this effect is due to a complete

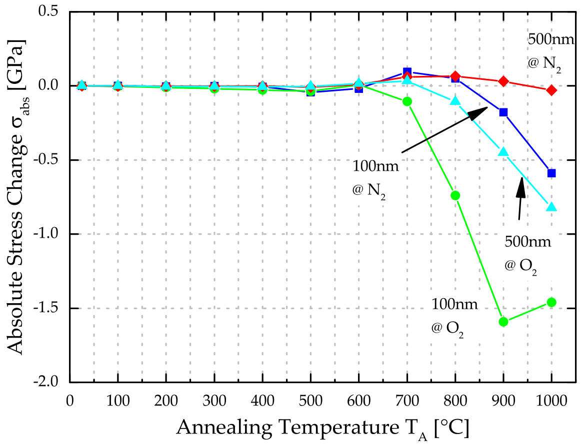

Figure 3.13: Influence of temperature and gas atmosphere on the absolute intrinsic stress change of thin AlN layers.

oxidation of the AlN layer, whereas during the chemical and structural modifications relaxation effects may occur.

3.3.2 Surface Roughness

A low surface roughness independent of temperature load is important for the subsequent deposited thin film electrode, which has a total desired thickness of ~50 nm. Figure 3.14 shows AFM measurements of AlN thin film samples with a thickness of 500 nm, in the *as deposited* state as well as after annealing at $T_A = 600$ °C and $T_A = 1000$ °C in argon, nitrogen and oxygen atmospheres, respectively. The surface topography of *as deposited* films and that of samples after annealing at $T_A = 600$ °C are smooth and show similar features. After an annealing temperature of $T_A = 1000$ °C, however, the surface shows hillocks with heights up to 40 nm independent of the gas atmosphere. The surface roughness R_a at varying annealing temperatures for AlN thicknesses h_{AlN} of 100 nm, 500 nm and 1000 nm is shown in Figure 3.15. As expected, the surface roughness in the *as deposited* state depends on the thickness of the AlN layer. Independent of the AlN thickness and the gas atmosphere, R_a is within the measurement accuracy constant up to $T_A = 800$ °C at around 1 nm. At $T_A = 900$ °C the surface roughness increases up to 2-3 nm, by increasing the temperature to 1000 °C the surface roughness reaches a value of 4-7 nm with local height maxima of ~40 nm independent of the gas atmosphere. Lee *et.al* showed that the surface roughness increases even more dramatically up to R_a values of 130 nm at temperatures above 1200 °C [87].

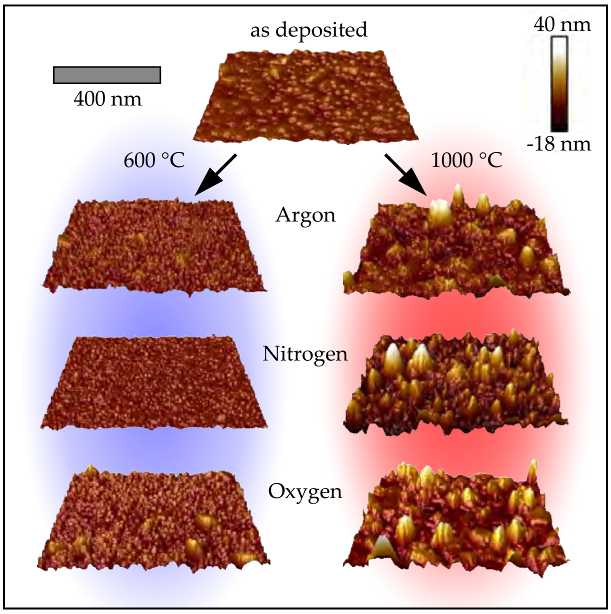

Figure 3.14: AlN surface morphology in the *as deposited* state and after $T_A = 600$ °C and $T_A = 1000$ °C in argon, nitrogen and oxygen atmosphere ($h_{AlN} = 500$ nm).

This can be a problem for thin electrode materials, where the growing hillocks can penetrate into the thin layer resulting in electrical short-cuts or interruption. Their formation is due to the high thermal energy, favoring reorganization and recrystallization processes especially at the top surface and at the grain boundaries. For the sample with a thickness of $h_{AlN} = 100$ nm in oxygen atmosphere the behavior looks different. At first the formation of the hills are the same, but at an annealing temperature of 1000 °C the layer has nearly the same surface roughness value of about 3 nm as at an annealing temperature of 900 °C. The surface roughness after the temperature load at 1000 °C is half the value compared to the nitrogen or argon atmosphere. A reason for this behavior can be the completely oxidation of the thin film AlN layer. As a result, no further increase in roughness was observed. A second effect may occur, where the thin oxide layer during the temperature load smooths the surface, a similar behavior was observed by the oxidation of tantalum [88]. Ababneh showed in his thesis, that during the temperature load, the increasing compressive intrinsic stress leads to delamination effects and hence, to an increase in surface roughness [89]. Additionally, to the behavior he showed, that micro-pores are forming inside the layer at temperatures of 1000 °C, leading to a porous, nitrogen-containing Al_2O_3 layer with a closed alumina surface .

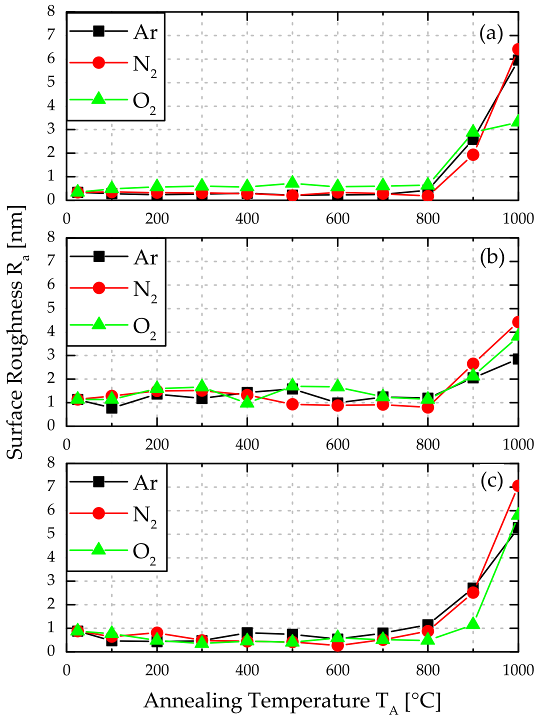

Figure 3.15: Influence of annealing temperature and gas atmosphere on the surface roughness of AlN films with a thicknesses of 100 nm (a), 500 nm (b) and 1000 nm (c).

3.3.3 X-Ray diffraction

Figure 3.16 shows XRD measurements of AlN samples after different annealing temperatures. The time for all samples was 2 hours in different atmospheres (nitrogen and oxygen). The (002) peak at around 36° corresponds to the c-axis orientated AlN and remains stable up to $T_A = 1000$ °C except for $h_{AlN} = 100$ nm in oxygen atmosphere (see Fig. 3.16(a)). During thermal load at this temperature level in oxygen atmosphere, the sputtered AlN thin film oxidizes and forms an amorphous aluminum oxide, as demonstrated by XRD measurements. The complete oxidation and additional relaxation effects of the layer can explain why the intrinsic stress of the thin film does not follow the trend, as illustrated in Figure 3.13. The FWHM of the (002) peak is for all samples between 0.20° and 0.24°, except for $h_{AlN} = 100$ nm and $T_A = 900$ °C in oxygen atmosphere, which is around 0.31°. It is reasonable to assume, that this can be attributed to partial oxidation of the layer, which has a direct influence on the lattice parameter. In contrast, complete oxidation is not observed after 2 hours (see Fig. 3.16(b)) for samples with a thickness of $h_{AlN} = 500$ nm, which does not mean that the surface is not oxidized. Figure 3.17 shows the 2θ peak position gained from XRD measurements as a function of intrinsic stress. Basically, the XRD position is strongly dependent on the intrinsic stress of the thin film layer. The diffusion and oxidation of the layer during the temperature load induce additional compressive intrinsic stress, which results in a shift of the (002) peak to lower values. Up to $T_A = 900$ °C, the position is nearly constant except for the separately labeled temperatures. At higher temperature load the compressive stress shifts the position of the XRD peaks toward lower values, as the lattice distance in c-axis direction is increased. Except for the $h_{AlN} = 100$ nm sample at $T_A = 900$ °C in oxygen atmosphere, all points are in the corridor indicated by two brown solid lines. After 2 hours, an AlN thin film of $h_{AlN} = 100$ nm is completely oxidized. To evaluate how long it will take for different AlN thicknesses to get oxidized, high temperature XRD measurements were performed for 24 hours in pure oxygen atmosphere. Figure 3.18(a) shows continuous XRD measurements at $T_A = 1000$ °C for an AlN sample with $h_{AlN} = 100$ nm. It can be seen that the (002) peak vanishes in less than 60 min, whereas AlN films with a thickness of $h_{AlN} = 500$ nm (see Fig. 3.18(b)) need ~3 hours to oxidize completely. Additionally after ~5 hours an alumina peak is measured at 37.4°. It seems, that for the formation of the crystalline alumina phase a minimum thickness of the AlN layer is required. For AlN thicknesses $h_{AlN} = 1000$ nm

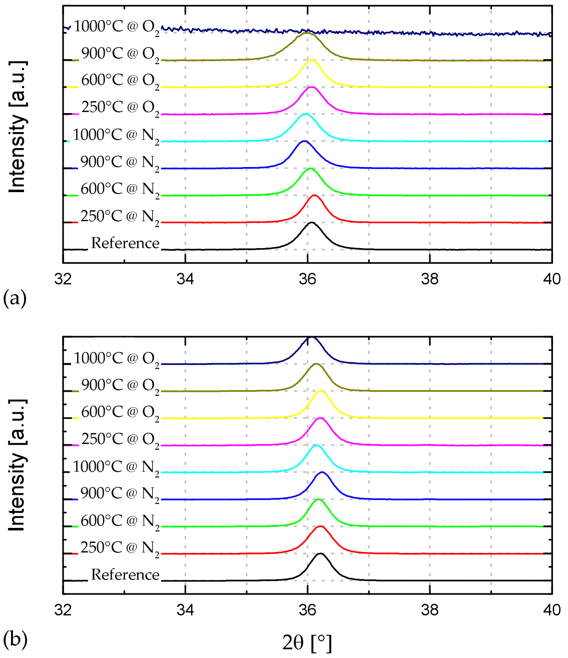

Figure 3.16: XRD measurements of $h_{AlN} = 100$ nm (a) and $h_{AlN} = 500$ nm (b) after annealing at high temperatures and in different gas atmospheres.

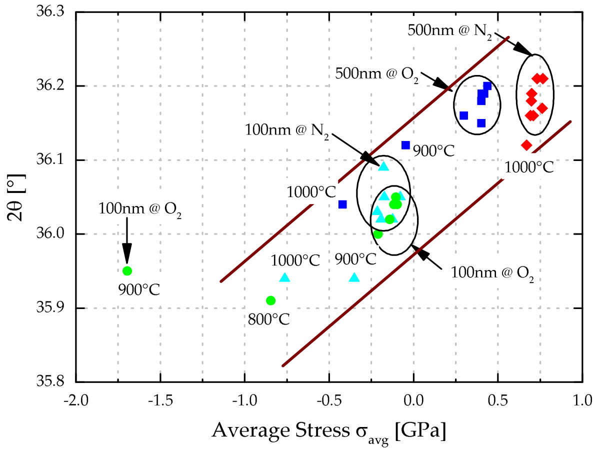

Figure 3.17: (002) AlN peaks determined from XRD measurements vs. the average stress σ_{avg} for samples annealed in different atmospheres and at different temperatures. Clustered points showing samples with annealing temperatures between $T_A = 25$ °C and $T_A = 900$ °C except for separately labeled temperatures. The corridor indicated by two brown solid lines in which the values are located serves as guide to the eyes.

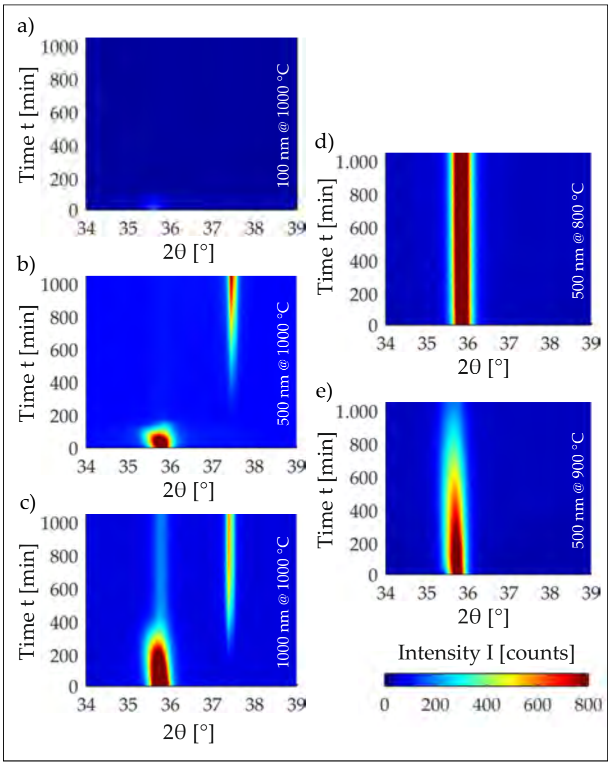

Figure 3.18: Continuous XRD measurements at high temperatures at AlN samples of different thicknesses in oxygen atmosphere.

(see Fig. 3.18(c)) the behavior is similar. As expected, the layer needs again more time to become completely oxidized, but the crystalline alumina phase is measured after ~5 hours. It is reasonable to assume, that due to the polycrystalline microstructure of the AlN also poly crystalline alumina is generated. To analyze the maximum temperature stability of AlN layers in oxygen atmosphere, high temperature XRD measurements were also performed at different temperature levels. An oxidation process is also observed for samples with a thickness $h_{AlN} = 500$ nm at $T_A = 900$ °C (Fig. 3.18e). The (002) peak gets weaker but is still measured after 24 hours, but no formation of the alumina peak at 37.4° is detected. At $T_A = 800$ °C (see Fig. 3.18d) no measurable degeneration was observed after 24 hours. Similar behavior of the decrease in intensity in the spectra at 800 °C and 900 °C was reported by Kolodzey *et al.* after 1 hour, even the formation of Al_2O_3 was observed after 1 hour at an annealing temperature of 1000 °C [90]. The difference in the time, when the Al_2O_3 peaks rises is more than 4 hours earlier compared to AlN layers investigated in this work. A hint can be the difference in the deposition process. Kolodzey *et al.* uses a UHV magnetron sputtering system (Denton Vacuum Discovery 18) with a operation power between 200–400 W with a N_2/Ar gas mixture [91]. Compared to parameters used in this work with DC power of 800 W and pure nitrogen atmosphere, the AlN thin film is longer stable in pure oxygen atmosphere. A reason could be a denser thin film morphology and hence, a higher oxidation resistance.

3.3.4 Piezoelectric Constants $\mathbf{d_{33}}$

The piezoelectric constant d_{33} is an important parameter of the AlN thin film layer. The d_{33} values after deposition process are between 5.1 to 6.6 pm/V across a 100 mm wafer. A degeneration of the d_{33} due to thermal load will have a negative impact on the efficiency when converting electrical to mechanical energy and *vice versa*, thus having a direct influence on the SAW performance. Figure 3.19 shows the piezoelectric constant d_{33} of AlN layers with a thickness h_{AlN} of 100 nm and 500 nm after annealing at varying temperatures up to 1000 °C for two hours in different atmospheres. For each temperature value and gas atmosphere, a separate sample from the same wafer is used. The d_{33} value of sputtered AlN with the parameter set given in Table 3.2 is in the range between 5.1 and 6.6 pm/V, which is in good agreement with values between $d_{33} = 5.15$ pm/V and $d_{33} = 6.5$ pm/V reported in the literature [92–94]. After thermal load, a lithography step is used to define electrode structures on top of the piezoelectric film. The results show that the temperature load has only low influence on the piezoelectric parameter. Only for oxygen atmosphere the piezoelectric effect decreases at higher temperatures, because alumina does not feature the piezoelectric effect. For an AlN thickness of $h_{AlN} = 100$ nm this effect starts at 800 °C, whereas for $h_{AlN} = 500$ nm at $T_A = 1000$ °C The degeneration of the d_{33} value is in good agreement with *in situ* high temperature XRD measurements (see Figure 3.18), where the degeneration of the AlN, indicated by the decrease of the reflected (002) peak at $2\theta = 36°$, is observed at the same temperature.

3.3.5 Leakage Current

Figure 3.20 shows a measured leakage current characteristics at $T_M = 25$ °C as a function of a positive electrical field E for a 500 nm thin AlN layer. When applying a fitting procedure to the measurement data it is demonstrated that for low electrical fields $E < 0.1$ MV/cm, the leakage current is dominated by an ohmic conduction mechanism. For fields $E > 0.3$ MV/cm the dominating mechanism changes from ohmic to a

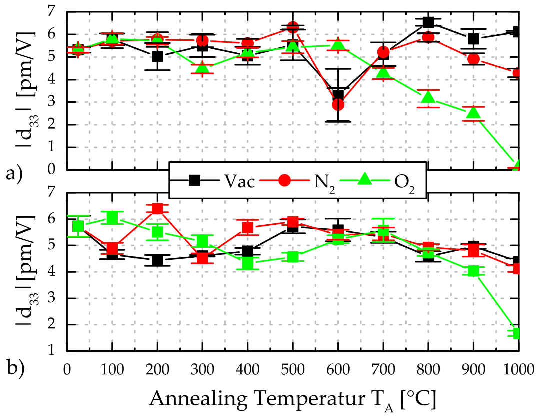

Figure 3.19: Influence of annealing temperatures and different gas atmospheres on the piezoelectric constant d_{33} at room temperature with an AlN thickness of 100 nm (a) and 500 nm (b).

Poole-Frenkel behavior. In between, a combination of both leakage mechanisms fit the measurement data well. Similar results are reported by Schneider *et al.* [51].

During the exposure of the sample in harsh environments, diffusion or oxidation processes starts to occur, which can change the leakage current mechanism. Different AlN samples, for each temperature and atmosphere (nitrogen or oxygen), one device were annealed for 2 hours. After the annealing step electrodes with a diameter of 1 mm were deposited on the surface. To remove the native oxide on the backside of the silicon substrate, an ISE step was performed, before metallization. The leakage current measurements were done at temperatures starting at $T_M = 25$ °C and from 100 °C onwards to 300 °C in steps of 50 °C. To evaluate the electrical stability of the thin film layer in harsh environment, the electron barrier height was extracted from Poole-Frenkel fits by analysing the activation energy at electrical fields $E > 0.3$ MV/cm. Additionally, to the Poole-Frenkel evaluation and the extraction of the barrier height, investigation on the ohmic transport mechanism for electrical field values up to 0.1 MV/cm was done. Figure 3.21(a) shows a typical leakage current density J versus electrical field E measurements up to 300 °C in air of the samples with $h_{AlN} = 100$ nm after annealing in nitrogen atmosphere at $T_A = 600$ °C. It features symmetrical characteristics when combining J as positive and negative applied field values. Furthermore, the measurement at room temperature shows a low hysteresis. The hysteresis originates from the impact of the rest polarization in the AlN thin film, which occurs by changing the applied

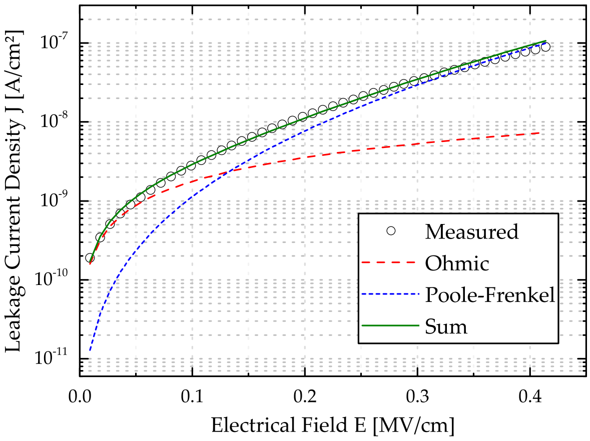

Figure 3.20: Measured leakage current density J versus electrical field E at $T_M = 25$ °C with fitted ohmic and Poole-Frenkel conductive mechanism.

electrical field [95]. Its impact is decreased when using smaller electrical field steps and longer measurement times (i.e. 30 s). Basically, the hysteresis is more dominant at temperatures below 100 °C. A similar leakage current characteristic is measured for a sample in oxygen atmosphere after 600 °C load (see Fig. 3.21(b)). The leakage current density changes dramatically after higher annealing temperatures. Figure 3.21(c) shows a leakage current measurement after the annealing at $T_A = 1000$ °C in nitrogen atmosphere. The leakage current density decreases compared to the sample annealed at 600 °C, but the hysteresis gets more dominant up to a measurement temperature of 200 °C. Whereas, a typical leakage current measurement for $T_A = 1000$ °C in oxygen atmosphere is shown in Figure 3.21(d) yielding an asymmetrical behavior for positive and negative applied field values with a more pronounced hysteresis. Therefore, to improve the evaluation of the electron barrier height, only these current values with a very small hysteresis at a given temperature are used for further evaluation (e.g. 100 °C and onwards for the 100 nm sample at $T_A = 600$ °C in nitrogen atmosphere). The leakage current as a function of the electrical field E and measurement temperature T_M follows Poole-Frenkel [95, 96], according to the equation

$$J(E, T_M) \propto E \cdot e^{-E_a/k_B T_M} \tag{3.1}$$

where k is the Boltzmann constant [50]. Arranging these data in Arrhenius configuration, the activation energy E_a can be determined for each value of E. Figure 3.22 shows an Arrhenius plot for $h_{AlN} = 100$ nm and an applied electrical field of $E =$

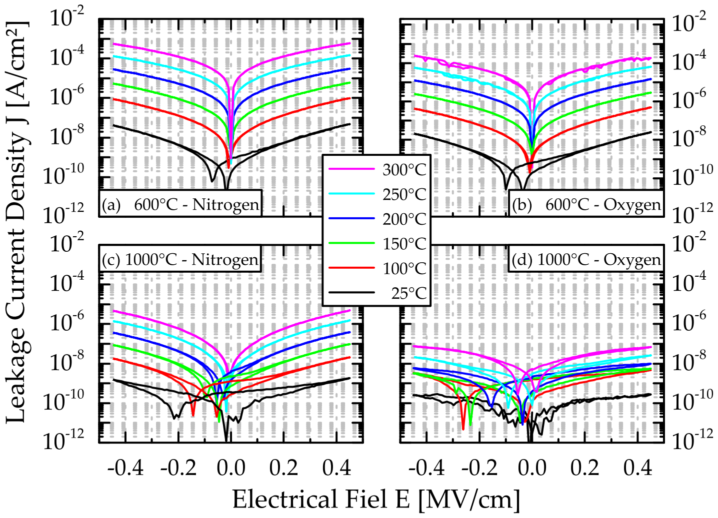

Figure 3.21: Current density J versus applied electrical field E for a 100 nm thin AlN layer after annealing at $T_A = 600$ °C in (a) nitrogen and (b) in oxygen atmosphere as well after $T_A = 1000$ °C in (c) nitrogen and (d) oxygen atmosphere for 2 hours for different measurement temperatures up to 300 °C.

0.45 MV/cm. With the dataset $E_a(E)$, the Poole-Frenkel barrier ϕ_B height can be extracted. Figure 3.23 shows extracted $E_a(E)$ curves with Poole-Frenkel fits, according to the following equation

$$E_a(E) = q(\phi_B - \sqrt{qE/\pi\epsilon_0\epsilon_r}), \tag{3.2}$$

where q is the elementary charge and ϵ_0 is the vacuum permittivity [50]. Schneider *et al.* showed, that the relative permittivity of AlN can be assumed to $\epsilon_r = 10$ [65]. Due to the same deposition equipment used for AlN layer in the latter and in this work, the same value was used for further data evaluation. For temperatures up to $T_A = 700$ °C, the measured data are in excellent agreement with Eq. 3.2, which confirms the assumed Poole-Frenkel behavior for $E > 0.3$ MV/cm. Figure 3.23 shows this for AlN thickness of 100 nm (a) and 500 nm (b) for an annealing temperature of $T_A = 600$ °C in nitrogen and oxygen atmosphere. Above $T_A = 700$ °C, the behavior of the leakage current mechanism changes as can be seen for an annealing temperature of $T_A = 900$ °C in Figure 3.23(c) and 3.23(d). It is assumed that several mechanisms superimpose, especially as strong modifications occur in the thin film, like changing of the intrinsic stress (section 3.3.1) or oxidation of the layer (section 3.3.3). Additionally, Figure 3.23 shows that

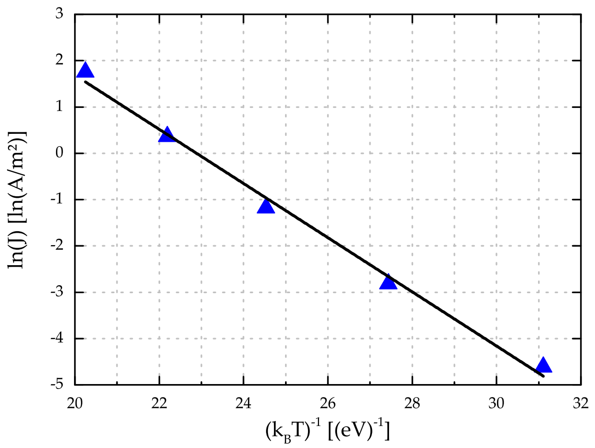

Figure 3.22: Current density J versus $1/k_BT_M$ at an applied electrical field $E = 0.45$ MV/cm for a 100 nm thin AlN layer after annealing at $T_A = 600$ °C.

the oxidation of the AlN significantly decreases the activation energy. Table 3.3 shows the calculated barrier heights ϕ_B based on Poole-Frenkel behavior for $h_{AlN} = 100$ nm and $h_{AlN} = 500$ nm thin AlN layers after annealing at different temperatures up to $T_A = 1000$ °C in nitrogen and oxygen atmospheres for 2 hours. It shows that the barrier height for AlN is in the range between 0.60 and 0.72 eV. This range matches well with data reported in literature for similar sputter deposited AlN films [65]. Ouisse *et al.* showed that by heating up the substrate to 800 °C and exchanging the sputter equipment by an evaporation system with an additional RF plasma source, deposited AlN reaches an electron barrier level of 0.815 eV [97]. Furthermore, ϕ_B values decrease for samples annealed in oxygen. For the 100 nm thin sample, it starts at $T_A = 800$ °C and for 500 nm at $T_A = 900$ °C. The difference can be attributed to the not fully oxidized layer and remaining AlN compounds. The final barrier height between 0.30 and 0.40 eV is lower than reported for sputter-deposited Al_2O_3, which is in the range of 0.6 eV [96]. Compared to reported atomic layer deposited Al_2O_3, it is slightly higher, which is in the range of 0.26 eV [98, 99].

To evaluate the change in leakage current mechanism at electrical fields $E < 0.1$ MV/cm, ohmic leakage current densities were calculated and compared to selected samples. The ohmic transport density was calculated according to Equation 2.14 for each measured temperature and multiplied with a pre-factor ζ. This pre-factor was needed to adjust the calculated ohmic transport density to the measurement values in the electri-

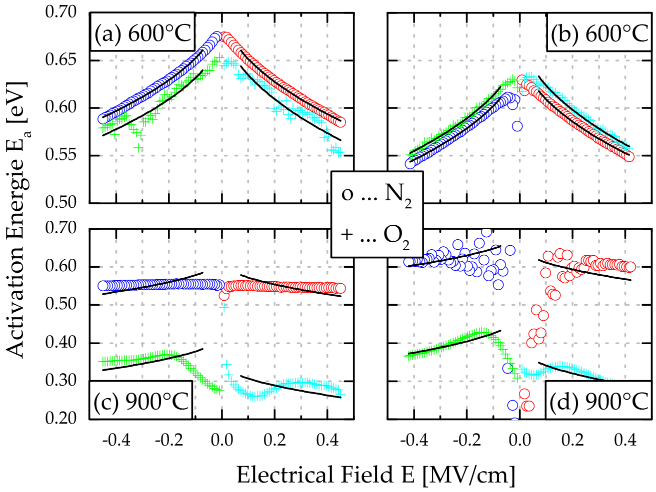

Figure 3.23: Activation energy E_a versus electrical field E with Poole-Frenkel fit for (a) 100 nm and (b) 500 nm after annealing at 600 °C and (c) 100 nm and (d) 500 nm after annealing at 900 °C for 2 hours in nitrogen and oxygen atmospheres.

Table 3.3: Electron barrier heights ϕ_B for 100 nm and 500 nm thin AlN samples annealed at different temperatures in nitrogen and oxygen atmospheres.

	100 nm				500 nm			
	N_2		O_2		N_2		O_2	
	neg. E	pos. E	neg. E	pos. E	neg. E	pos. E	neg. E	pos. E
T_A [°C]	ϕ_B [eV]	ϕ_B [eV]	ϕ_B [eV]	ϕ_B [eV]	ϕ_B [eV]	ϕ_B [eV]	ϕ_B [eV]	ϕ_B [eV]
25	0.65	0.65	0.65	0.65	0.70	0.70	0.70	0.70
250	0.60	0.58	0.61	0.62	0.73	0.72	0.66	0.63
500	0.63	0.64	0.63	0.58	0.69	0.70	0.68	0.68
600	0.71	0.71	0.70	0.69	0.67	0.66	0.69	0.67
700	0.67	0.67	0.62	0.63	0.65	0.63	0.67	0.67
800	0.62	0.63	0.41	0.41	0.71	0.69	0.68	0.70
900	0.56	0.56	0.36	0.40	0.66	0.69	0.39	0.48
1000	0.53	0.53	0.33	0.34	0.54	0.52	0.33	0.36

cal field range $E < 0.1$ MV/cm. Figure 3.24 shows the J-E characteristic for a 100 nm thin AlN layer in the *as deposited* state (a), and annealed at 600 °C in nitrogen (b) and oxygen (c) as well at 1000 °C in nitrogen (d) and oxygen (e) atmosphere. The measurement and the according ohmic transport calculation exhibit that the thin film does not change the electron transport mechanism independent of the gas atmosphere up to an annealing temperature of 600 °C. For an annealing temperature of 1000 °C in nitrogen, the ohmic transport mechanism is dominating, but the overall current level is decreased. This can be an indicator, that defects get annealed inside the layer during the high temperature load. For the oxygen atmosphere at 1000 °C the behavior looks different. The leakage current decreases even more compared to the sample annealed in nitrogen atmosphere. Furthermore, the influence of the measurement temperature decreases. This means that the dominant Poole-Frenkel mechanism, which is sensitive to the measurement temperature for electrical fields $E > 0.3$ MV/cm loses the dominant role. This is in good agreement to the Poole-Frenkel evaluation as discussed above. Therefore, the dominant Poole-Frenkel mechanism for $E > 0.3$ MV/cm is mainly exchanged by the ohmic transport behavior for a 100 nm AlN layer. For an AlN thickness of 500 nm the leakage current mechanism characteristic looks similar as to the 100 nm samples independent of the gaseous atmosphere up to 600 °C, which can be seen in Figure 3.25(a-c). As expected for the 1000 °C in nitrogen annealed sample, the leakage current density decreases, but the dominating ohmic conduction mechanism for an electrical field $E < 0.1$ MV/cm decreases. For the annealed sample at 1000 °C in oxygen atmosphere the influence of the Poole-Frenkel mechanism is still presented, due to the not completely oxidized AlN layer compared to the 100 nm samples, where the influence of the Poole-Frenkel behavior gets negligible. Therefore, the deposited thin film can be assumed to be a mixture of alumina and AlN-rich regions, where in the first mainly an ohmic mechanism is presented and in the latter still the Poole-Frenkel mechanism dominates.

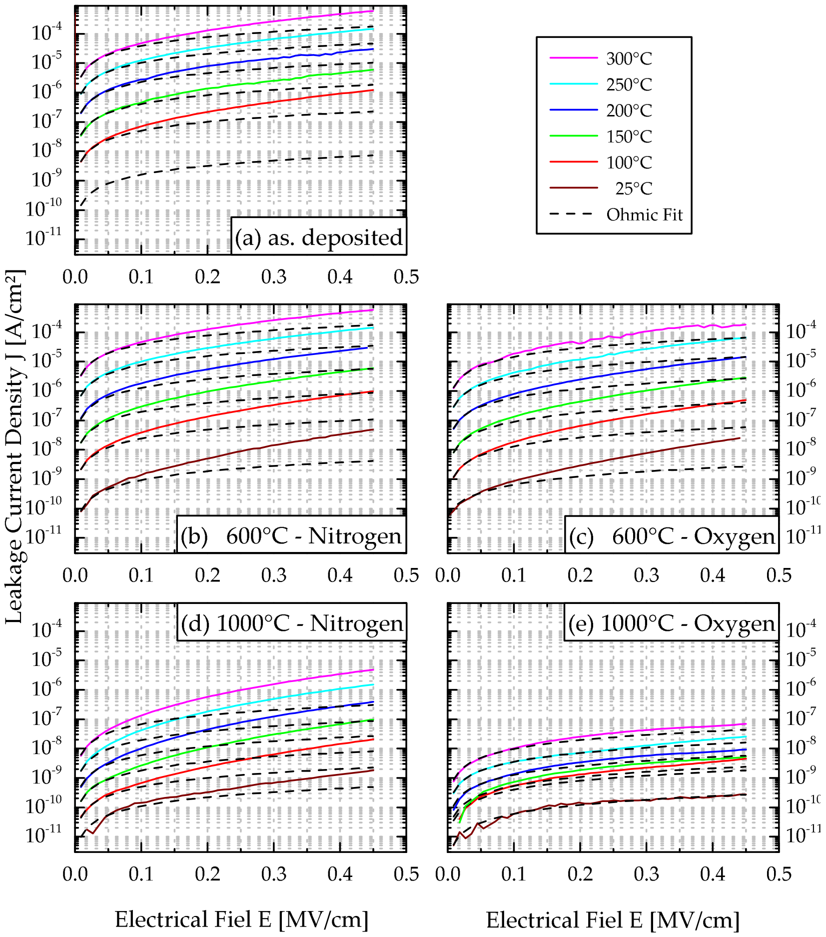

Figure 3.24: Calculated ohmic transport density compared to measured leakage current density J for 100 nm thin AlN samples after deposition (a), after an annealing at 600 °C in nitrogen (b), oxygen (c) and after an annealing at 1000 °C in nitrogen (d) and oxygen (e) atmosphere.

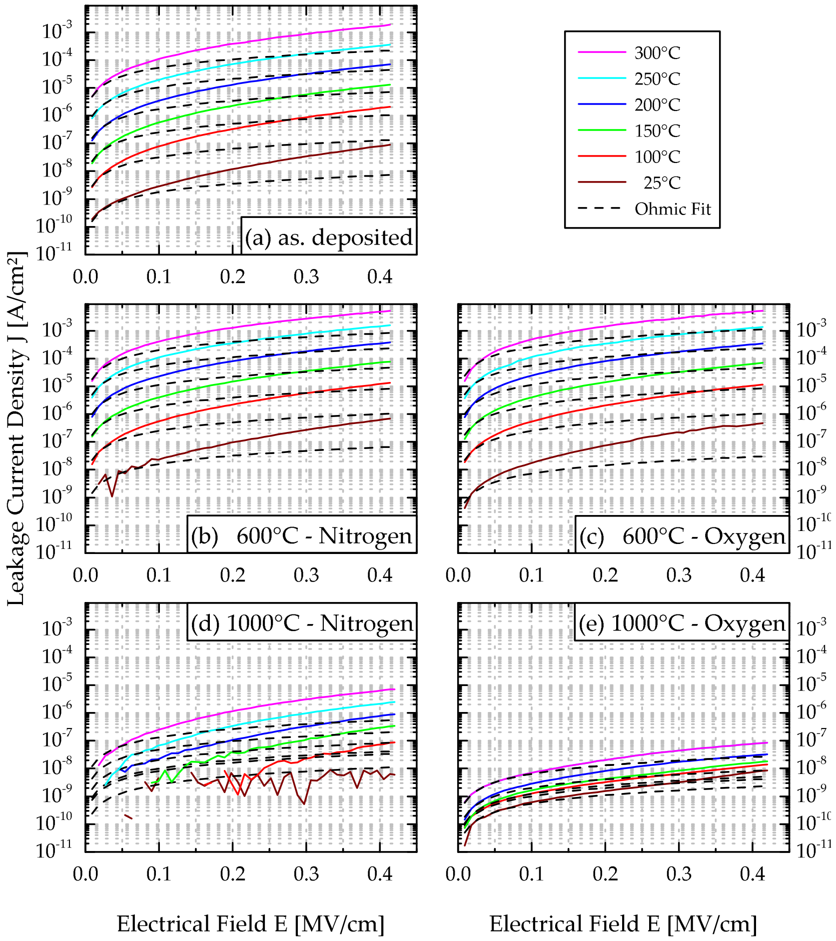

Figure 3.25: J-E characteristics of calculated ohmic transport mechanism compared to 500 nm thin AlN samples after deposition (a), after an annealing at 600 °C in nitrogen (b), oxygen (c) and after an annealing at 1000 °C in nitrogen (d) and oxygen (e) atmosphere.

3.4 Conclusions

Sputter deposited AlN thin films offer high potential as piezoelectric material for SAW application in harsh environments. The thickness of the AlN layer for SAW devices is typically several µm, which can be fabricated with deposition temperatures below 150 °C. To reduce the probability of failure for SAW devices due to crack and delamination effects, the intrinsic stress can be adjusted with a custom-built clamping tool, thus fixing the wafer during film synthetization. Additionally, with this approach, piezoelectric layers up to a thickness of 10 µm can be deposited. Furthermore, an ISE process prior to the sputter deposition process improves the alignment of the AlN grains, which results in an improved c-axis orientation in the thin film. The AlN layer is stable up to 600 °C in various gaseous atmospheres (nitrogen, oxygen) and does not change any properties (e.g. intrinsic stress, surface roughness or leakage current mechanism). Above, compressive stress is generated, due to diffusion of gaseous species from the atmosphere into the layer. Above 800 °C, the leakage current, intrinsic stress behavior and surface roughness are strongly modified. The increased roughness at such high temperatures due to hillock formation with a maximum height of 40 nm can cause problems in the electrode layer (for example short-cuts or failure in metallization lines). Additionally, the layers will start to oxidize at temperatures above 900 °C in oxygen-contained atmospheres. In parallel, at higher electrical fields the leakage current mechanism changes from Pool-Frenkel to a dominating ohmic mechanism or by partially oxidation to a superposition of several mechanism. Furthermore, the oxidized AlN layer loses the piezoelectric property. Therefore, to use AlN for SAW applications at higher temperatures in oxygen atmosphere the surface needs to be protected. For this purpose, the following chapter 4 investigates appropriate electrode materials as well coatings for passivation.

4 ELECTRODES AND PASSIVATION

Parts of this chapter have been published in ...

4.1 Basic Informations

Conductive materials are important parts of microelectronic or MEMS devices. They connect different components within a device electrically for e.g. signal or energy transport. Depending on the application, different materials are required. In the following Table 4.1 selected conductive materials are listed, which are typically used in MEMS devices as electrode material. Each possible electrode material has its individual melting point, electrical resistivity and standard atomic weight. Metals with very low electrical resistivity are silver, copper or gold. Aluminum also has a very low electrical resistivity, but additionally it features a low density compared to materials like platinum. In addition, the melting point has to be taken into account for high temperature applications. Iridium features a melting point of $T_{MP} = 2446$ °C followed by platinum with $T_{MP} = 1768$ °C and palladium with $T_{MP} = 1554$ °C. Aluminum has in this selection the lowest melting point with $T_{MP} = 660$ °C. Furthermore, the atomic density is important for SAW devices, since higher density values lead to a resonance frequency shift, see section 5.4. This can be compensated by an optimized device design (e.g. changing the pitch of the interdigital transducers). Besides these pure materials for the electrode, also intermetallic alloys can be used like iridium-aluminum. With a minimum of 60 at.% aluminum a stable self-passivation layer without losing material to the gaseous oxide phase is ensured [100]. A disadvantage of this material is the extreme oxide thickness of 30 µm, which is not useable for SAW devices where the electrode material should be as thin as possible to avoid negative effects on the performance (e.g. resonance shift) [101]. Therefore, each material has its advantages and disadvantages as electrode material. In this work, mainly platinum, iridium and aluminum are used as electrode material. An advantage of these three materials is a

Table 4.1: Properties of selected conductive materials [17].

Material	Melting Point [°C]	Electrical Resistivity $10^{-8}\Omega$ m	Standard Atomic Weights
Platinum	1768.20	9.78	195.08
Iridium	2446.00	4.70	192.21
Gold	1064.18	2.05	196.96
Palladium	1554.80	9.78	106.42
Silver	961.78	1.47	107.86
Copper	1084.62	1.54	63.54
Aluminum	660.32	2.42	26.98

straight-forward deposition with a MEMS technology compatible sputter equipment.

Besides the high temperature load further challenge for these materials is the aggressive oxygen atmosphere. Bartlett *et al.* showed that even platinum oxidizes at high temperature above 1060 °C in air atmosphere with 10^{-6} cm/hr. It is reasonable to assume, that with even at lower temperatures platinum will oxidize, but with a lower rate. Therefore, an equilibrium condition will result at the platinum surface due to the reversible oxidation reaction [102]:

$$O_2(g) + Pt \rightleftharpoons PtO_2(g) \tag{4.1}$$

It yields an oxidation of platinum and simultaneous desorption of gaseous platinum oxide from the surface and therefore a loss of the conductive material. This behavior was first reported by Fryburg *et al.* [103, 104]. Even iridium, which has a higher melting point, forms volatile oxides such as IrO_2 and IrO_3 at temperatures above 600 °C [105, 106]. Aluminum with its low melting point of $T_{MP} = 660$ °C, features at room temperature a native oxide thickness of ~0.5 nm, whereas at 300 °C this oxide thickness is increased to 0.9 nm. At temperatures above 400 °C no constant oxide layer thickness could be reached by Juergens *et al.*, because the layer oxidizes completely [107]. In addition to the oxidation, thin platinum and iridium layers show recrystallization and de-wetting effects during high temperature loads above 700 °C, which can result in loss of the electrical conductance and hence, to a complete device failure [108–111]. Also the adhesion layer can have an influence on the film resistance. For example, pure titanium as adhesion layer starts to diffuse at temperatures above 450 °C predominantly along platinum grains [112]. This means that thin conductive paths in SAW devices with a typical lateral dimension of 0.5 to 6 µm and some 50 to 100 nm thickness, have to be protected carefully before high temperature loading to prevent oxidation and dewetting effects. There are ongoing investigations into the passivation of electrodes with ultra-thin SiAlON or ZrSiON composite materials in the thickness range of ultra-thin < 50 nm up to 1000 nm using reactive co-sputtering equipment [14–16]. Moulzolf *et al.* showed that these materials can protect the SAW sensor surfaces from degeneration and help to stabilize the IDT electrodes [113]. To adjust and vary the concentration of the different elements, a special equipment with two simultaneously driven targets is needed, which increases the complexity of the equipment and of the process.

In this work, AlN, Al_xO_y and Si_xN_y with thicknesses up to 400 nm were investigated. They are fabricated with a MEMS compatible reactive sputter deposition process at temperatures below 150 °C. The purity of each single element target was 5N. The low deposition temperature allows a resist based lift-off process for electrode pattering. These layers should serve as an oxidation barrier and should also prevent the thin film electrode from dewetting during high temperature load. Furthermore, the effective temperature where dewetting occurs is decreased when targeting thinner electrodes independent of the selected material [114]. Therefore, to decrease negative influence by mass loading effects of SAW devices, the thin electrode paths have to be protected against dewetting. AlN was selected to reduce the number of different materials in the SAW architecture. Zhu *et al.* showed that reactively sputtered Al_xO_y reduces the oxidation process of Ni-based superalloys to rate of 3-8 times for temperatures between 800-1100 °C [115]. LPCVD deposited Si_xN_y is used in the so-called local oxidation of silicon (*LOCOS*) process as oxidation barrier during the oxidation process of the silicon wafer, which was first introduced by Appels *et al.* [116]. Therefore, it was of interest if even RF reactively sputtered Si_xN_y would fulfill the requirement as an effective oxidation barrier layer.

4.2 Test Structure Design

The high temperature performance of sputter deposited electrode materials was investigated on a 1 µm thick AlN thin film deposited on a silicon substrate. The purpose of this AlN layer is to isolate the different electrode paths from each and provide a test system close to the final SAW device architecture. Furthermore, the adhesion between

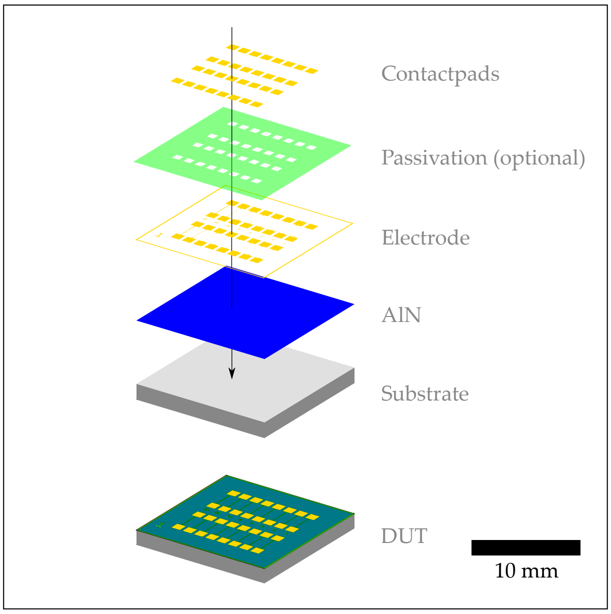

Figure 4.1: Explosion illustration on the layer sequence for high temperature stability testing.

the AlN layer and the electrode material under thermal stress could be evaluated. The next layer is the electrode stack starting with an adhesion layer between 5 nm and 10 nm titanium nitride or tantalum. Titanium nitride was used in combination with platinum and tantalum with iridium, respectively. Pre-investigation showed, that the adhesion layer has a negligible influence on the electrical resistance in the *as deposited* state, so that only those two bi-layer systems are tested. For aluminum no adhesion layer was used. At a given length of 1450 µm the thickness of the metallization lines was 50 nm at a width varying between 1 up to 50 µm. Pads at the end of the lines were designed for connecting and measuring the resistance of the individual metallization lines. Optionally, a 100 nm thin passivation layer of either AlN, Si_xN_y or Al_xO_y was deposited and subsequently patterned to provide an opening for the contact pads. Finally, the pads were thickened in a final depositing process with an additional layer of 200 nm platinum. A schematic overview of the layer sequence is illustrated in Figure 4.1.

4.3 Metallization Layer

A proper electrode design is of utmost importance for surface acoustic wave devices (e.g., the metallization ratio between electrode and free space is fixed to 50%:50%, see

Table 4.2: Sputter parameters for electrode and adhesion materials.

Parameter	*Pt*	*Ir*	*Al*	*TiN*	*Ta*
Target	Pt	Ir	Al	Ti	Ta
Target [mm]	100	100	150	150	150
Power [W]	75	150	300	300	350
Ar flow [sccm]	60	60	50	40	60
N_2 flow [sccm]	0	0	0	40	0
O_2 flow [sccm]	0	0	0	0	0
Back pressure [µbar]	3	3	3	8	3
Deposition rate [nm/s]	0.5	0.79	1.18	0.09	1.19

chapter 5). A *lift-off* process is used to pattern the electrode material. In Table 4.2 sputter deposition parameters for the electrode and adhesion materials are listed. The adhesion layer thickness of *TiN* and *Ta* was between 5 nm and 10 nm.

The following Figure 4.2 shows a lateral thickness profile of *lift-off* processed metallization lines with widths of 2 µm, 5 µm and 10 µm. Iridium with a nominal thickness of 113 nm was deposited with 10 nm tantalum as adhesion layer. The figure shows that lines with different widths have different heights and a non-rectangular profile, which can be explained by shading effects of the tiny resist trenches. Due to the large angle of incidence of impinging particles during sputter deposition, the side walls of the resist are coated as well as the substrate. This hinders the *lift-off* of the resist and results in teared-off edge characteristics remaining at the deposited structure. This can cause problems when covering in a subsequent step the structure with additional layers. This is a general problem of sputter deposition in combination with a *lift-off* process. Full wafer metallization and conventional etching would be another technique. In comparison, wet chemical etching is quite difficult to control for noble metals like platinum when e.g. applying *aqua regia* at elevated temperature of 65 °C. For iridium, special methods such as high-density plasma etching in chlorine-oxygen-argon plasma are needed with the additional drawback that the underlying AlN layer can be unintentionally attacked [111, 117]. Another preferable technique would be ion etching, where the surface is removed by pure kinetic energy, thus would damage also the underlying layer. In this work, the straight forward *lift-off* method was used to fabricate metallization lines to avoid any modification of the AlN surface.

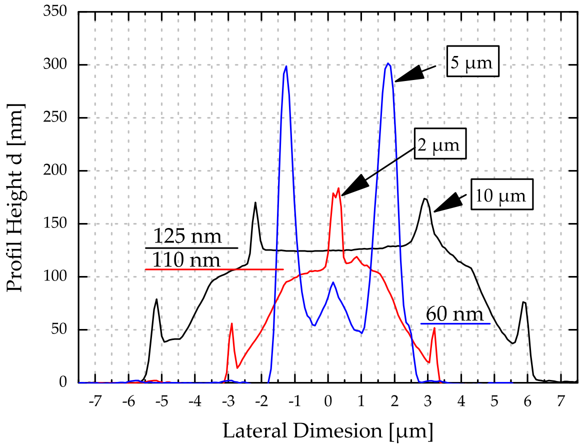

Figure 4.2: AFM profile measurements across metallization lines of different widths fabricated by *lift-off*.

Furthermore, the focus of the high temperature electrode testing was on the temperature-induced modifications and the maximum temperature stability of the deposited material in pure nitrogen or oxygen atmosphere. All metallization lines had a length of $l_{cp} = 1450$ µm and a thickness of ~ 100 nm. For further investigations, a sheet resistance R_s value was determined for different metallization line widths d_w between 1 µm to 5 µm in 1 µm steps and at 10 µm, 20 µm and 50 µm. The sheet resistance R_s is calculated for all line widths with the following equation:

$$R_s = R_{measured} \frac{d_w}{l_{cp}} \tag{4.2}$$

Figure 4.3 shows averaged R_s of the different metallization line widths for platinum, iridium and aluminum thin films after annealing up to $T_A = 1000$ °C in nitrogen (a) and oxygen (b) atmosphere for 2 hours. For each temperature and atmosphere a separate sample was used. The different heights of error bars can be attributed to the variation of the manufactured inhomogeneities during fabrication of the test structures. Aluminum is stable up to $T_A = 500$ °C in both atmospheres. Above this temperature, the metallization lines failed independent of line width, due to dewetting effects. For platinum, the behavior is different. At temperatures between $T_A = 400$ °C and $T_A = 700$ °C, a strong change of the resistance compared to the *as deposited* value is observed. It is reasonable to assume, that in this temperature range a reorganization of the microstructure starts to occur. Given the low deposition temperature, the high melting point of the material and the low sputtering power, the film morphology resembles *Zone T* according to Thornton [22]. Furthermore, titanium diffuses along the grains

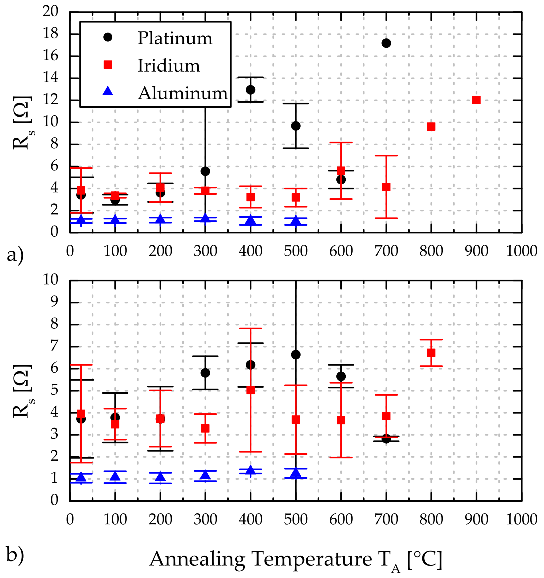

Figure 4.3: R_s of platinum, iridium and aluminum as a function of temperature and nitrogen (a) and oxygen (b) atmosphere.

toward the surface, which leads to a higher electron scattering at the grain boundaries and hence a higher film resistance [112, 118]. At $T_A = 800$ °C, most of the metallization lines are broken indicated by a high resistance value above 60 kΩ. For Iridium, the R_s values are lower and more stable over a wider temperature range compared to platinum. In nitrogen atmosphere, the resistance starts to increase at an annealing temperature $T_A = 800$ °C. At $T_A = 1000$ °C, all metallization lines are broken. Even in oxygen atmosphere, Iridium shows a stability up to $T_A = 800$ °C. Furthermore, narrower electrode lines with a width of 1 µm, 2 µm and 3 µm show an earlier failure at temperatures above 700 °C. For those high temperatures, more than 80 % of the metallization lines are broken and an error bar could not be calculated due to the lack of measurable samples. Figure 4.4 shows surface images of TiN/Pt multilayer at the contact areas with a thickness of 10/250 nm in the *as deposited* state (a) and annealed layers in nitrogen (b) and oxygen (c) at 600 °C as well in nitrogen (c) and oxygen (d) at 1000 °C after 2 hours in a furnace. The surface morphology looks for annealed sample at 600 °C similar to the *as deposited* thin film independent of the gas atmosphere. At 1000 °C the behavior looks different. The metallization layer shows a strong agglomeration with dewetting effects, so that even the surface of the bottom AlN layer gets exposed. It is reasonable to assume, that the degeneration of the thin film during hole forming can be described in a two stage process. In the first stage, grooves are

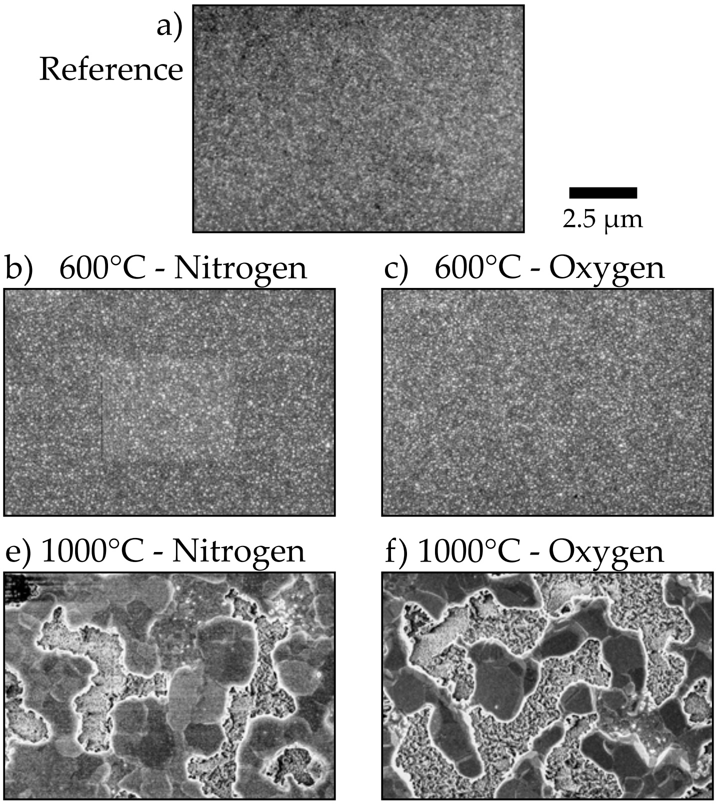

Figure 4.4: SEM images of the TiN/Pt bi-layer surface in the *as deposited* state (a) and exposed at 600 °C in nitrogen (b) and oxygen (c) and at 1000 °C in nitrogen (d) and oxygen (e) after 2 hours.

formed at the grain boundaries, which was first reported by Mullins [119]. With time at a given temperature load, the grooves deepen and may even penetrate through the thin film leading to hole formation. In the second stage, the holes are growing, due to surface diffusion until the complete thin film gets dewetted, so that the thin film is transformed into unconnected island [109]. The presence of oxygen accelerates the degeneration of the film, according to standard literature [120, 121]. To reach higher resonance frequencies of e.g. 2.4 GHz in SAW devices, a metallization line width of around 600 nm is required. Given these material-related results, these inter-digital structure would fail under high temperature load due to the lower electrode width. Therefore, a protective passivation layer is required to stabilize the metallic thin film below. In the following section 4.4 selected passivation coatings are tested for this purpose. Later in section 4.4.2, the effectiveness of passivation coatings in combination with the electrode material are evaluated.

Table 4.3: Sputter parameters of the used passivation coatings.

Parameter	AlN	Al_xO_y	Si_xN_y
Target	Al	Al	Si
Target Ø [mm]	150	150	150
Power [W]	800 DC	800 DC	600 RF
Ar flow [sccm]	0	10	20
N_2 flow [sccm]	50	0	60
O_2 flow [sccm]	0	10	0
Back pressure [µbar]	2	2	5
Deposition rate [nm/s]	0.44	0.14	0.09

4.4 Passivation Coatings

In this section the impact of a passivation being either a sputter deposited Al_xO_y, Si_xN_y or AlN film on the high temperature stability of the metallization lines is investigated. All three passivation layers were chosen, because they are regarded as high temperature stable materials (for AlN see also chapter 3) and can be easily fabricated using sputter deposition process [100, 122]. Furthermore, with a deposition temperature below 150 °C, electrical connection through the passivation layer coating can be realized in a straight forward approach using a resist-based lift-off process. In the following Table 4.3, the sputter deposition parameters for all three layers are listed.

4.4.1 High Temperature XRD

In this section results of pre-investigations on the temperature robustness of AlN thin films are reported using *in-situ* high temperature XRD measurements up to 1000 °C. Figure 4.5 shows the effect of oxygen on the (002) peak position of AlN layers with a thickness of 500 nm during high temperature load. For each temperature, five XRD measurements with 10 minutes delay between each measurement were performed, to investigate the shift of the peak position over time. The (002) peak shifts linearly up to $T_M = 800$ °C toward lower angle values, which can be attributed to the thermal expansion of the thin layer during temperature exposure. Basically, the peak position remains constant over all 5 measurements for each temperature level. At $T_M = 850$ °C and above, however, the (002) peak starts to continuously shift with each measurement

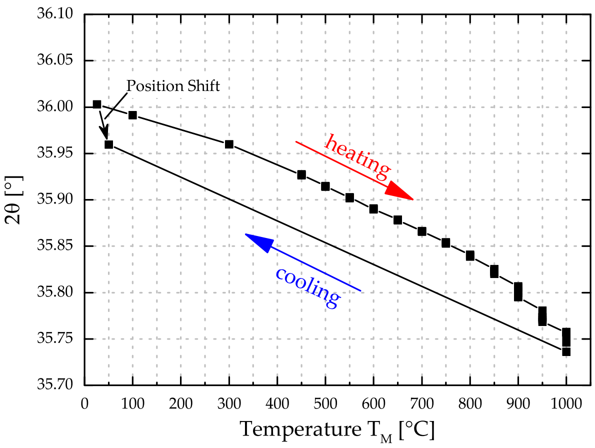

Figure 4.5: AlN (002) peak position from high temperature XRD measurements from 25 °C up to 1000 °C and down to 50 °C measured at a 500 nm thin film.

at a given temperature level. This can be attributed to the diffusion of oxygen into the layer and thus oxidation of the AlN layer occurs, which expands the unit cell. The shift even remains, when the sample is cooled down to $T_M = 50$ °C again, indicating a non-reversible modification within the layer.

To test the effectiveness of Al_xO_y and Si_xN_y as a coating material, a polycrystalline AlN thin film below the passivation layer is used as an indicator. If the AlN layer oxidizes like in section 3.3.3, it would mean that the passivation coating is not sufficient enough as an oxygen barrier at the measured temperature. The passivation layer thickness was set to 100 nm. Figure 4.6 shows continuous XRD measurements at $T_M = 1000$ °C for several hours in oxygen atmosphere. Due to the temperature load the AlN peak (002) is shifted from original ~36° (room temperature) by ~0.2°, as previously shown. An AlN film with a thickness of $d = 500$ nm without any passivation coating oxidizes completely after t = ~2 hours, which can be seen in Figure 4.6a, as the (002) peak completely disappeared. After $t = 7$ hours an $Al_{2.67}O_4$ polycrystalline alumina phase at $2\theta = 37.4°$ starts to form, indicating its growth with an increasing intensity with time [123]. Figure 4.6b shows the corresponding measurement with an additional d = 100 nm Al_xO_y passivation layer. The measured intensity of the AlN (002) peak decreases significantly slower compared to the sample without passivation. The AlN peak is not measurable after t = 6 hours. Also the formation of polycrystalline alumina phase out of the AlN layer starts later at t = 16.5 hours, indicated by the peak

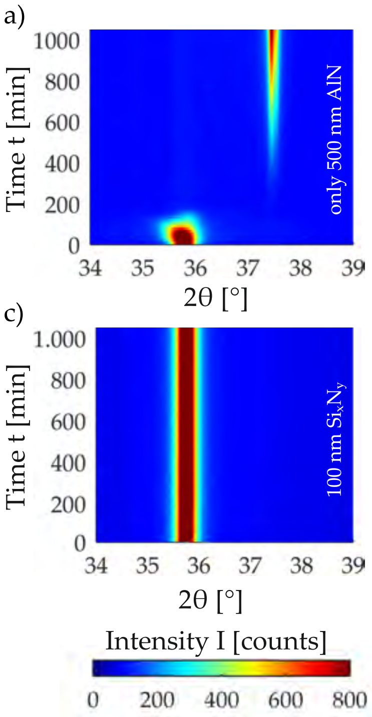

Figure 4.6: Continuous high temperature XRD measurements at 1000 °C of 500 nm AlN with additional 100 nm passivation layer of AlN (a), Al_xO_y (b) and Si_xN_y (c), whereas (d) represents the first and the last XRD measurement of each sequence.

at $2\theta = 37.4°$ (Figure 4.6b). Figure 4.6c shows the same measurement with d = 100 nm Si_xN_y passivation coating, where the oxidation of the AlN thin film is completely suppressed and no degeneration of the AlN layer after 24 hours at T_M = 1000 °C in pure oxygen atmosphere is observed. Figure 4.6d shows XRD measurements at the beginning and the end of the high temperature measurement procedure. It can be seen that for the AlN layer without and with an Al_xO_y passivation layer, the AlN (002) peak vanishes and an $Al_{2.6}O_4$ polycrystalline phase starts to form. But, with Si_xN_y as passivation layer the maximum intensity of the AlN (002) peak remains constant during the complete measurement cycle. As a result, Al_xO_y and AlN are not recommended as efficient oxygen diffusion barrier. Therefore, Si_xN_y should be preferred for operation at high temperatures and in oxygen-rich atmospheres. AlN as passivation layer can be used in inert gas atmospheres for electrode protection against dewetting and reduction of induced thermal stress due to different thermal expansion coefficient of the involved materials.

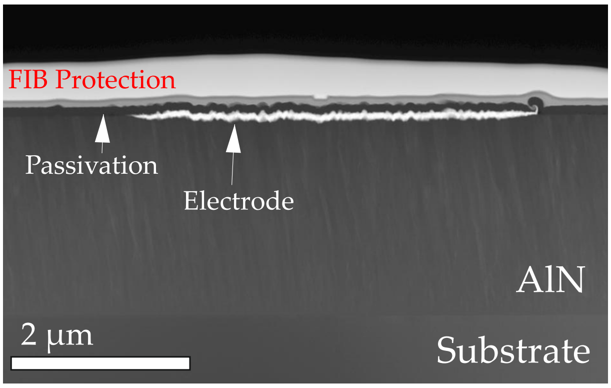

Figure 4.7: Cross sectional image of a single platinum metallization line with a width of 4 µm and a thickness of 50 nm, with additional 50 nm Si_xN_y as passivation layer.

4.4.2 Impact of Annealing on Electrical Thin Film Resistance

To evaluate the robustness of the passivation coatings on top of the electrode material, structures are fabricated as illustrated in Figure 4.1. Figure 4.7 shows a typical cross section of a 5/50 nm bi-layered TiN/Pt electrode with 50 nm Si_xN_y as passivation. The electrode is homogeneously covered by the thin passivation layer. On top of the passivation a bi-layer of 100 nm chromium as adhesion promoter and 400 nm palladium was deposited to protect the sample during FIB preparation.

Due to the previous high temperature XRD measurements, only Al_xO_y and Si_xN_y are selected as passivation layers. Figure 4.8 shows the average R_s value of different line widths of platinum with and without passivation layer as a function of annealing temperature in different atmospheres. Figure 4.8a shows that platinum without passivation changes the resistance after $T_A \geq 400$ °C significantly, see also section 4.3. After $T_A = 800$ °C, no current could be driven through the metallization line due to delamination effects. With an additional passivation layer of Al_xO_y or Si_xN_y, a reasonable resistance of the metallization lines is measured even after an annealing temperature up to 800 °C. After $T_A = 900$ °C, however, only test structures protected with Si_xN_y could be measured. The variation in the resistance values are predominantly attributed to fabrication intolerance's in line width over the whole 100 mm wafer. Therefore, a maximum error of 2 % in the calculation of the R_s occurs, but the method is sufficient to measure the influence of harsh environmental conditions on the electrode resistance. With an Al_xO_y passivation layer, the metallization lines still worked after a maximum

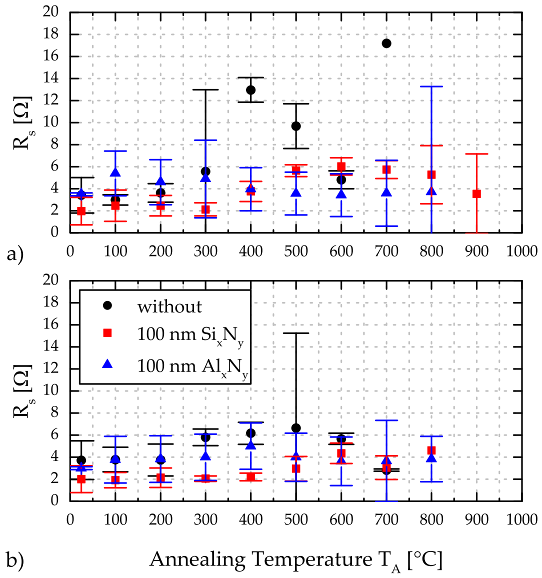

Figure 4.8: R_s of platinum without and with Si_xN_y and Al_xO_y passivation layer as a function of temperature and nitrogen (a) and oxygen (b) atmosphere.

annealing temperature of $T_A = 800$ °C in oxygen atmosphere. This is 100 °C higher than without passivation coating. With a Si_xN_y protection, the metallization line survived even an annealing after $T_A = 900$ °C. When applying an annealing temperature above, all these test structures designed as simple conduction paths failed.

A similar behavior is observed with iridium as an electrode material, see Figure 4.9(a). Without passivation the metallization is electrically measurable after an annealing up to a maximum temperature of $T_A = 900$ °C in nitrogen atmosphere. After 1000 °C all the metallization lines were broken, see also section 4.3. If a passivation layer is used, test structures survived even an annealing step of $T_A = 1000$ °C independent of the passivation layer in nitrogen atmosphere for 2 hours. In addition, the sheet resistance remains constant in the range between 1-3 Ω even over this large temperature range. It is reasonable to assume, that the passivation coating protects the metallization lines most efficiently against delamination and dewetting. In oxygen atmosphere the metallization lines are intact after an annealing temperature of 800 °C. At $T_A = 900$ °C the contact pads, which consist of an additional platinum layer oxidize and/or delaminate.

Based on these results, both platinum and iridium electrodes with passivation layers could be used for operations temperatures up to 800 °C even in oxygen atmosphere. Above this temperature, the adhesion between the different layers (electrode and pas-

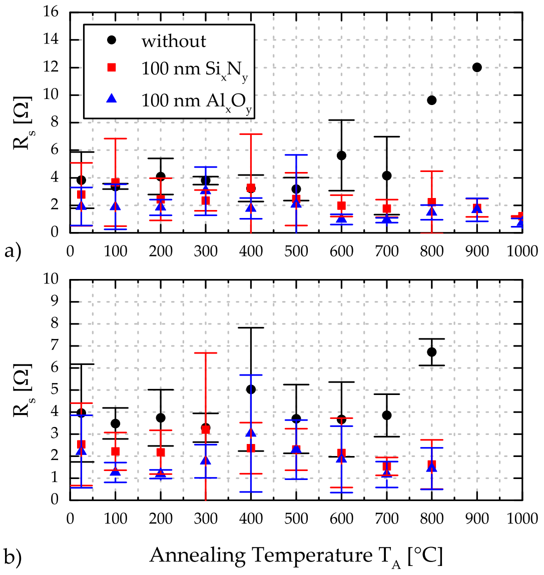

Figure 4.9: R_s of iridium without and with Si_xN_y and Al_xO_y passivation layer as a function of temperature and nitrogen (a) and oxygen (b) atmosphere.

sivation coating) decreases. This can be seen by the partial delamination of the protection layer, see also section 5.5.4, Figure 5.28). With reactive sputter deposited Si_xN_y as coating, high temperature SAW devices can be fabricated, without degeneration and oxidation of the thin electrode interdigital structure. A weak point are the contact areas needed for the electrical characterization, which are not covered by the passivation and exposed to the surrounding atmosphere.

4.4.3 Intrinsic Stress

To estimate the influence of Si_xN_y passivation coating on the total stress of the devices, Si_xN_y with a thickness of d = 100 nm was deposited on top of 500 nm AlN on a 100 mm silicon wafer. This deposited layer on top of the AlN layer generates an additional compressive stress of $|\sigma_{avg}|$ = 150 MPa. The average intrinsic stress was measured before and after each annealing temperature step beginning at 100 °C up to 1000 °C in 100 °C steps using an oxidation furnace. The atmosphere in the furnace was either pure nitrogen or pure oxygen. The absolute stress change σ_{avg} was determined according to $\sigma_{avg} = \sigma_{after\,annealing} - \sigma_{as\,deposited}$. For comparison, wafers with AlN thin films without additional passivation coating were fabricated and annealed under the same conditions, as shown in section 3.3.1. Figure 4.10 shows the absolute change in

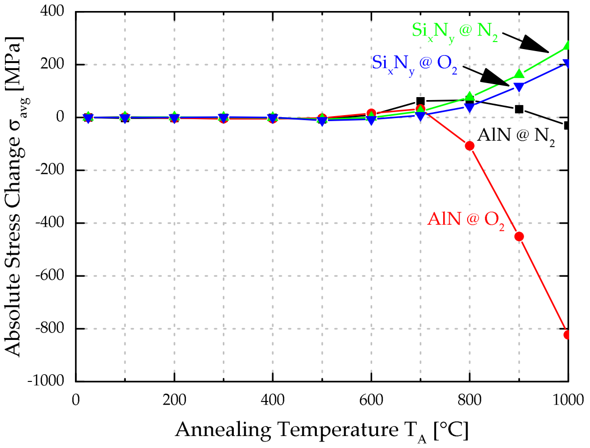

Figure 4.10: Influence of annealing temperature and gas atmosphere on the intrinsic stress of 500 nm thin AlN (see also section 3.3.1) and AlN/Si_xN_y bilayer (500 nm/100 nm).

average stress σ_{avg} measured at room temperature as a function of annealing temperature. For both thin film systems the film stress remains constant up to an annealing temperature $T_A = 600$ °C independent of the atmosphere. At $T_A = 700$ °C, tensile stress is induced into the AlN film without passivation. Above $T_A = 700$ °C, a shift toward compressive stress is observed. This can be attributed to the diffusion of nitrogen and oxygen into the layer, whereas oxygen additional forms an alumina structure. The behavior for AlN with Si_xN_y passivation coating is significantly different. Above $T_A = 600$ °C the film stress continuously shifts towards tensile stress. A reason for this can be the relaxation of the additional compressive film stress and further a prevention of diffusion of nitrogen and oxygen atoms into the AlN layer, which would generate additional compressive stress.

4.5 Conclusions

The functionality and stability of the electrode material at higher temperatures and in aggressive atmospheres for high temperature sensors based on SAW devices is very important. For this reason, materials were chosen, which have a high melting point and are resistive against oxidation, like platinum or iridium. To increase the robustness of the electrode against oxidation and dewetting, an additional passivation coating is needed. AlN itself, which is also used as an active piezoelectric material, is not recommended, because the layer starts to oxidize in oxygen containing atmospheres at temperatures of 900 °C and does not prove to be an efficient oxidation barrier. In oxygen atmosphere also the reactively sputtered Al_xO_y does not show the required properties, because the AlN layer arranged below the passivation coating gets oxidized. It may, however, be used as a protection against dewetting. On the other hand, reactively sputtered Si_xN_y proved to be the best solution for the desired operation under such harsh environmental conditions. The contact pads are still a weak point, which are not covered by the passivation coating to provide electrical access. They can still oxidize during the high temperature load in aggressive gaseous atmosphere.

5 SURFACE ACOUSTIC WAVE DEVICES

Parts of this chapter have been published in [53, 124, 125]

5.1 Theory

Surface **A**coustic **W**aves (SAW) exist in different shapes in nature. Earthquakes are one of them. Heavy damages can appear in distances of up to 50 km to the epicenter, due to the low damping of such waves [126, 127]. First descriptions of this phenomenon were done by Lord Rayleigh in the year 1885 [128]. In the year 1911, Love discussed propagation of horizontal shear waves and Sezawa demonstrated in the year 1927 higher order modes of Rayleigh waves [129, 130]. First small-scaled SAW devices were realized by White and Voltmer in the year 1965 [131]. They fabricated interdigital transducers (IDT) with a wavelength of 203.2 µm and a constant distance of 50.8 µm between each finger electrode. The IDTs generated and received the waves on a quartz crystal. One decade later in 1977, SAW devices were widely used as bandpass filters, delay lines, front-end filters, pulse compression filters or as TV broadcast filters [132]. Besides quartz other materials were also used, e.g. lithium niobate $LiNbO_3$ or lithium tantalate $LiTaO_3$. Nowadays, other promising materials are investigated like langasite $La_3Ga_5SiO_{14}$, langanite $La_3Ga_{5.5}Nb_{0.5}O_{14}$ or gallium phosphate $GaPO_4$. These materials offer higher electromechanical coupling of $k^2 = 0.44$ % for (langasite) compared to $k^2 = 0.12$ for ST-X quartz in combination with higher phase velocities of $v_p = 2700$ m/s (langasite) or $v_p = 2770$ m/s (langanite) compared to $v_p = 2343$ m/s for ST-X quartz [133–136]. To increase the operation frequencies of SAW devices one approach is to decrease the wavelength with the drawback that a more cost intensive lithography is needed. A second disadvantage is the increase of the signal damping. For example, langasite has a quadratic dependency on operation frequency [11]. An alternative to increase the operation frequency at a given wavelength $\lambda = 2.4$ µm from ~1 GHz to ~2.4 GHz, is to use materials with phase velocities above 5600 m/s. A promising solution is the combination of a non-piezoelectric substrate with high acoustic velocity like sapphire in combination with a piezoelectric thin film such as AlN or zinc oxide (ZnO) [137]. ZnO/sapphire features a phase velocity of 5400 m/s and a temperature coefficient of delay TCD of 43 ppm/°C compared to AlN/sapphire, which offers a phase velocity of 5700 m/s and a TCD of 0 ppm/°C [138, 139]. In this work the SAW devices made of AlN/sapphire are fabricated and evaluated with respect to robustness and stability as they are targeted to operate under harsh environmental conditions. In the following section, the architecture of the multilayer SAW devices fabricated in this work is presented and the experimental results are discussed.

5.1.1 Wave Generation

There are different types of surface acoustic waves like Rayleigh, Love or Sezawa waves. Rayleigh waves are vertical transversal waves perpendicular to the direction of propagation, whereas Love waves are horizontal transversal waves also perpendicular to the direction of propagation. The third type are Sezawa waves, which are Rayleigh waves of higher mode order. The primarily excited wave type depends on the crystal orientation and electrode design. This means that several wave types can be excited at the same time with different phase velocities but with different electromechanical coupling efficiency. A method from Campbell *et al.* can be used to verify the phase velocities of the different excited wave modes [140, 141]. By comparing the phase velocities from the theoretical model with the measured ones, it is possible to determine the excited types. Due to the different electromechanical coupling for different wave modes and additional signal damping, some waveforms can not be measured. Figure 5.1 shows an example for the configuration for AlN and sapphire to excite measurable Rayleigh and Love waves. In Figure 5.1(a) the (002) plane of the AlN layer is parallel to the (0001) c-plane surface of the sapphire substrate. In this configuration independent on the wave propagation direction Rayleigh waves are generated predominantly. Compared to Figure 5.1(b), where the (002) planes of the AlN layer is tilted by 26° to the $(1\bar{1}02)$ r-plane sapphire surface, additional to the Rayleigh waves also Love waves with the highest signal magnitude are excited, but with a very poor electromechanical coupling of < 0.05 % compared to the Rayleigh wave of ~0.1 % [141]. For this work a device design was chosen to generate primarily Rayleigh waves. Figure 5.2(a) shows calculated deflection of the material both parallel and perpendicular to the surface as a function of substrate depth, which were simulated by Schropp in 1988 [142]. It can

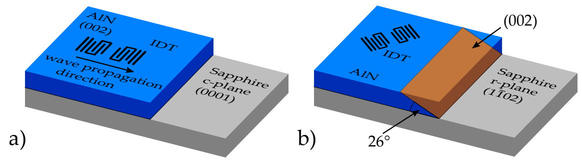

Figure 5.1: AlN-on-sapphire configurations to generate most effectively Rayleigh (a) and Love waves (b).

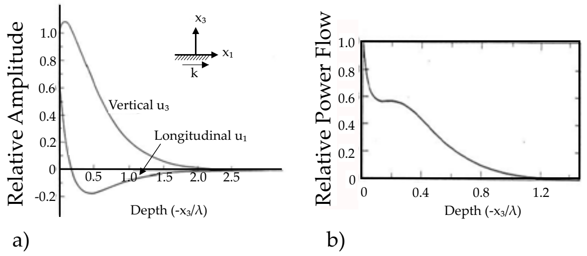

Figure 5.2: Deflection (a) and energy distribution (b) of a surface acoustic wave as a function of substrate depth [142].

be seen that most of the deflection is concentrated near the surface, but the wave extends into the material by almost two times of its wavelength. The energy density shows nearly the same behavior, as ~80 % of the energy is within a depth of half the wavelength (see Figure 5.2b).

IDTs were fabricated, which consists of two interleaving finger or comb structures. By applying an electrical signal with an arbitrary frequency spectrum, a mechanical wave is generated due to the piezoelectric effect. The wave moves perpendicular to the finger axis on the surface of the substrate with a material specific sound velocity. The waves generated by multiple finger pairs get superimposed and only waves with wavelength of twice the electrode pitch are excited effectively, whereas other wavelengths are damped. As a consequence, the device is working as a frequency filter. The sound velocity is a mechanical material constant and is in the range between approximate ~2000 m/s for langasite as substrate and 10000 m/s for AlN in combination with diamond as substrate, where the crystallographic direction strongly influences the velocity [143, 144]. For example with a wavelength of 2.4 µm operation frequencies of 833 MHz and 4.2 GHz can be reached, respectively.

5.1.2 Design Aspects

To fabricate high temperature stable (up to 600 °C) SAW devices for operation frequencies in the free useable 2.4 GHz band, sapphire is chosen as substrate. However, to evaluate basic design aspects, such as oxidation behavior or dewetting effects of the deposited thin films, silicon is used as a more cost efficient alternative for testing basic device features. Due to the increasing electrical conductivity of silicon when increasing temperature, the SAW devices based on silicon cannot be used above 220 °C (see section 5.5.1) and hence, the substrate is replaced by sapphire. Independent of the substrate, however, the basic fabrication steps are identical. Prior to deposition of the piezoelectric AlN or AlScN thin film, an ISE step with 500 W and 6 µbar in pure argon atmosphere was performed for 5 minutes. The piezoelectric layer thickness is varied between 500 nm and 3000 nm, with most of the devices featuring a 2000 nm thin AlN layer, where the influence on the phase velocity by different electrode materials and crystal orientation of the substrate is evaluated. In the next step, the electrode material was deposited with a nominal thickness of 40 nm. Platinum and Iridium were mainly used as conductive material due to high melting points. Depending on the selected material, an adhesion promoter was deposited with a maximum thickness of 10 nm. As materials for the latter purpose titanium nitride (TiN) and tantalum (Ta) were used. Subsequently, the contact pads were thickened with additional 200 nm platinum layer for better contact properties and to prevent penetration of the pad material by the probe needles. After this step, the SAW device is ready for characterization. This is a so-called *as fabricated* state. Optionally, to increase the stability of the devices in harsh environments, a passivation layer was deposited on the device to protect the fragile metallization lines forming the interdigital finger structures. Only a small area of 250 µm^2 was opened to provide contact to the electrodes. This passivation coating step is placed between the IDT fabrication and the thickening of the contact pads. Figure 5.3 illustrates the final device in an explosion drawing.

5.1.3 Network Vector Analyzer

A **N**etwork **V**ector **A**nalyzer NVA is an instrument for measuring electrical network parameters. The NVA generates a high frequency signal with an internal signal generator. The generated signal frequencies can range from 9 kHz (e.g. E5080A ENA Vector Network Analyzer from Keysight Technologies) and up to 1 THz where special

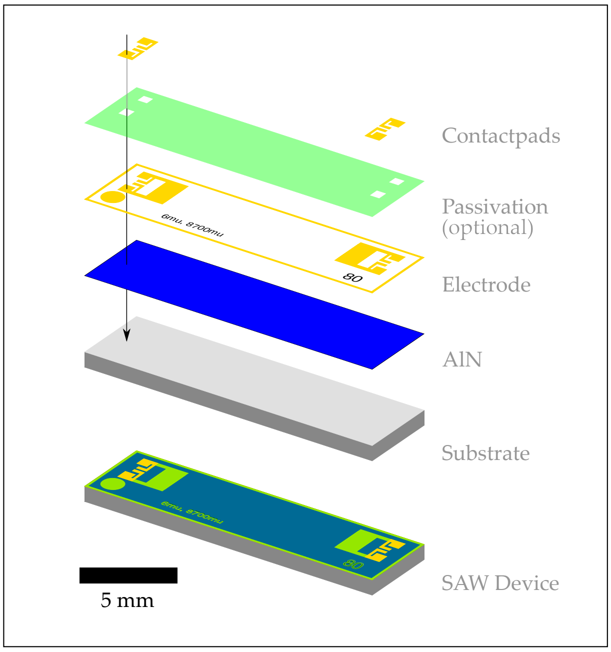

Figure 5.3: Explosion illustration with layer sequence of fabricated SAW devices.

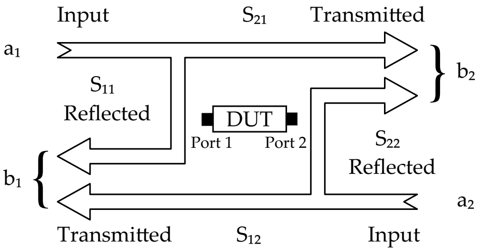

Figure 5.4: S-parameter relation between input and output signal for a two port DUT.

adapters are needed, as reported by Hesler *et al.* [145]. The generated signal is split into two parts. One part is applied to the device under test (DUT). The second one is used as a reference signal. The signal through the device will be measured at the receiver and compared with the reference signal. The results are called scattering parameters or S-parameters, which are complex quantities. Depending on the DUT, a combination of reflected and transmitted parameters can be determined. Figure 5.4 shows the relation between input and output signal based on a two port DUT.

The four S-parameters for a two port device are called:

- S_{11}: input reflection

- S_{21}: forward transmission
- S_{12}: reverse transmission
- S_{22}: output reflection

The indexes label the used ports. The first number corresponds to the measured port and the second number is related to the input port. For example, the S_{21}-parameter describes the transmission losses from port 1 to port 2. The relation between input and output can be written as:

$$b_1 = S_{11}\, a_1 + S_{12}\, a_2 \tag{5.1}$$

$$b_2 = S_{21}\, a_1 + S_{22}\, a_2 \tag{5.2}$$

where a_n is the input and b_n the output signal of port n. By applying a signal on port 1 S_{21} is evaluated by measuring the magnitude and the phase of the signal through the device on port 2. Additionally, port 2 is terminated with Z_0 to prevent any reflection of the port, so that the reflected signal caused only by the device can be measured simultaneously at port 1. If the source is switched to port 2 and port 1 is terminated with Z_0, the S-parameters S_{22} and S_{12} are measured. A not perfectly matched Z_0 with the DUT results in an artificially modified a_1 or a_2 and hence, has to be avoided as it results to an erroneous determination of the parameters S_{11} and S_{22}. Consequently, if Z_0 is perfectly matched, the S-parameters are determined as followed:

$$S_{11} = \left.\frac{b_1}{a_1}\right|_{a_2=0} ; \; S_{21} = \left.\frac{b_2}{a_1}\right|_{a_2=0} \tag{5.3}$$

$$S_{22} = \left.\frac{b_2}{a_2}\right|_{a_1=0} ; \; S_{12} = \left.\frac{b_1}{a_2}\right|_{a_1=0} \tag{5.4}$$

For symmetric SAW devices, as fabricated in this work, the S matrix should be symmetrical, thus $S_{21} = S_{12}$ and $S_{11} = S_{22}$. The used NVA is a HP8753 network vector analyzer from Hewlett Packard, which can measure up to 3 GHz with a given number of measurement points $N = 1601$. The impedance load Z_0 was set to 50 Ω. Due to the low number of measurement points, the frequency measurement range has to be adjusted for each wavelength, so that the resonance frequency is in the center of the investigated frequency range. Therefore, the measurement span B was between 100 MHz and 120 MHz. As a consequence, the length of the time domain is determined according to the following equation:

$$T = \frac{N}{B}\,[s] = \frac{1601}{120\, MHz}[s] = 13.4\; [\mu s] \tag{5.5}$$

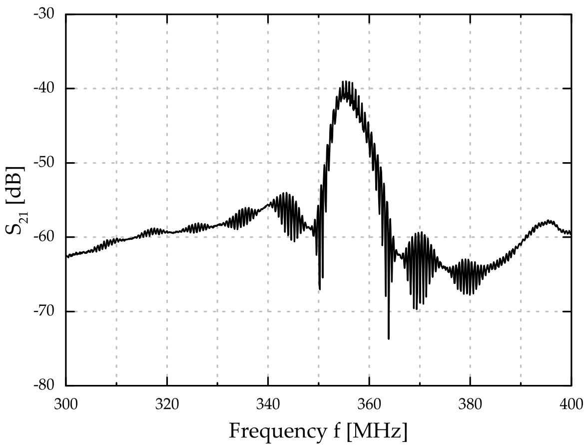

Figure 5.5: Typical S_{21} measurements of an AlN/sapphire device with a wavelength $\lambda = 16$ µm and a distance between transmitter and receiver of 8700 µm. The AlN thickness was 2 µm.

There are two main errors, which can occur: internal ones due to imperfections in the NVA electronics and external ones due to the impedance of the measurement wires and contact points. These latter error sources can be corrected by a careful calibration step applying a standard impedance substrate (e.g. P/N:143-033 from Cascade Microtech). It consists of a ceramic substrate with a defined relative permittivity ϵ_r of around 6 and conductive structures (short, open, matched load of 50 Ω and through) on top of the substrate. For a SAW delay line device, two coplanar probe needles (ACP-250GS and ACP-250SG from Cascade Microtech) are used and each of them has to be calibrated. First, each probe is measured in the selected frequency range in open, short and 50 Ω load configuration. Additionally, both signal and ground tips are connected together to measure the transmission loses of the cable and the contact resistance. Next, the NVA calculates the correction factors, which are used during the measurement procedure.

5.1.4 Device Characterization

The DUT was contacted with two ACP-250 probe needles from Cascade and connected to the NVA. Figure 5.5 shows a typical raw measurement of a SAW delay line device with a wavelength $\lambda = 16$ µm and an AlN thickness $h_{AlN} = 2$ µm on top of a sapphire substrate. This type of device shows a damping minimum at the resonance frequency ~355 MHz with some side-lobe frequencies. For further evaluation purposes, the measurement result is transferred from the frequency to the time domain, using a discrete fast Fourier transformation. To transform the signal from the frequency domain to the time domain, a window function is needed. The window function weights the measurement data of the signal. Furthermore, the window function forces the signal into a mathematical periodicity of the evaluated data range, so that at the beginning and at the end of the window the signal has the same value. This can be done using a rectangular or a smoother window functions like Hamming or Tukey. Without this, Gibbs phenomenon in the transformed signal can occur [146]. The Gibbs phenomenon describes the mathematical behavior of finite Fourier series during Fourier transformation of a piecewise continuously differentiable periodic function at a jump discontinuity. Large oscillations near the jump are generated with the n-th partial sum, but they do not vanish if n is increased to a finite limit [147]. Furthermore, with this technique parts of the signal can be separated in the time domain and isolated for further evaluation. Depending on the application, a suitable window function has to be chosen, because a trade-off between detail frequency resolution and frequency-dependent energy leakage has to be done. This means, that depending on the window function energy is transferred to the side-lobes, which is called leakage effect. These can directly be seen in the magnitude of the side-lobe. If the magnitude of the side-lobe is high compared to the main-lobe, a lot of energy is transformed during the FFT from the original signal to the side-lobe and is lost for further evaluation. This means that the main-lobe characteristics (i.e. height and width) and the leakage effect are directly connected. A narrow main-lobe has a high leakage effect, whereas an expanded main-lobe indicates minor energy leakages. This dependence during transformation is purely mathematical, because during the FFT a convolution between the signal and the window function is performed. A broader window function leads to a stronger smoothing of the signal during the convolution process [148]. In this work, a Tukey window with $\alpha_{Tukey} = 0.3$ is used for the inverse FFT to transfer the signal from the frequency to the time domain. This window function and the value 0.3 proved as a good trade-off between flexibility during the automatic resonance frequency determination procedure and the energy leakage effect. Due to the limitation of the measurement range of 120 MHz, the first and the last 18 MHz are windowed. As a result, Figure 5.6 shows the impulse response of the SAW device from Figure 5.5. The slope in the first few hundred ns can be attributed to the capacitive crosstalk of the measurement setting and the side effects of the FFT. The rise at the end is mainly due to the FFT convolution. The first SAW signal impulse arrives the receiver at $\tau = 1.66$ µs. At $\tau = 5$ µs the triple-transit

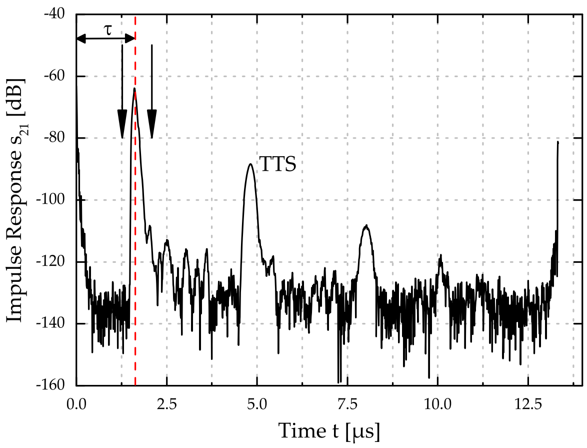

Figure 5.6: Impulse response s_{21} of an AlN device with a wavelength $\lambda = 16$ µm and a distance between the IDT's of 8700 µm with first impulse response τ = 1.66 µm from transmitter and receiver. The triple transit signal is located at τ = 4.97 µs. Arrows just before and after the first impulse indicates the gating times for further evaluation.

signal (TTS) is detected, where the wave is subsequently reflected by the receiver and the transmitter and finally converted by the receiver again. It is lower compared to the main peak, because the wave loses more energy due to three times traveling time and the additional energy transformation processes at the IDT's. To filter out the capacitive crosstalk and other wave modes like excited shear waves or bulk acoustic waves, the first impulse was windowed again with a Tukey function with $\alpha_{Tukey} = 0.3$. The beginning and the end of the window function are indicated with the arrows just before and after the impulse. The position was chosen automatically. First the peak position was detected by determining the maximum of the peak. Afterwards, a procedure for finding the nearest minimum of the signal before and after the peak was performed. Subsequently, the signal was Fourier transformed back into the frequency domain. Figure 5.7 shows the transmission spectrum S_{21} of the gated first impulse response. Due to the averaging process during the transformation, the signal becomes substantially smoothed. Additionally, the base line of the signal is strongly damped, which gives a better visualization of the resonance curve characteristics. This technique allows a detection and evaluation of the resonance frequency for devices with a low signal-to-noise ratio. The resonance frequency f_0 itself is determined by finding the maximum of the main-lobe.

To compare SAW devices with different wave lengths, the phase velocity v_p can be

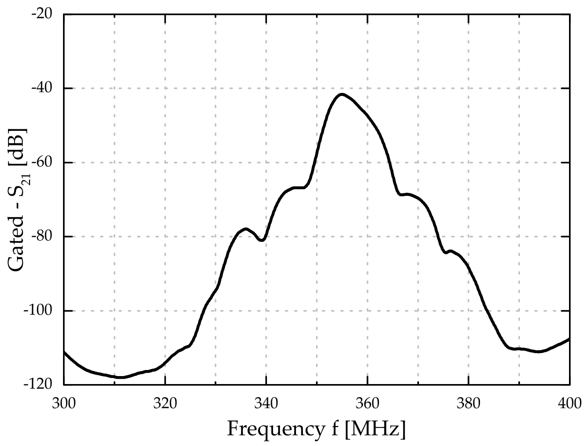

Figure 5.7: Gated first impulse response transmission spectrum S_{21} for wavelength $\lambda = 16$ µm and $d = 8700$ µm measured at a SAW device with a 2 µm AlN thickness.

calculated with the following equation 5.6:

$$v_p = f_0 \cdot \lambda \tag{5.6}$$

5.1.5 High Temperature Measurements

For evaluation of SAW devices at high temperatures and in argon atmospheres, a special measurement equipment is used. The devices were heated using a quartz tube furnace, which allows a regulation of the atmosphere. The SAW devices were placed on a special holder with connection to a copper center conductor having a dioxide dielectric as insulator. Three devices could be placed in the furnace for simultaneous measurements. The temperature was observed using a thermocouple, which was located inside the tube and about 4 cm away from the SAW samples so that the temperature measurement deviation is below 1 °C, what is accurate enough for testing the device functionality and robustness. The used network vector analyzer NVA for measuring the SAW devices was a ZVL6 from Rhode and Schwarz. Due to the simultaneous measurement of three devices, the NVA has to be manually reconnected to the devices for each temperature load. The advantage of the simultaneous measurement was that several samples were annealed with the same temperature profile, allowing a better comparison between the samples. A disadvantage of such an approach is the different interface impedance, which can be seen in different signal loses. Furthermore, the regulation of the temperature is very slow, so that when targeting a certain temper-

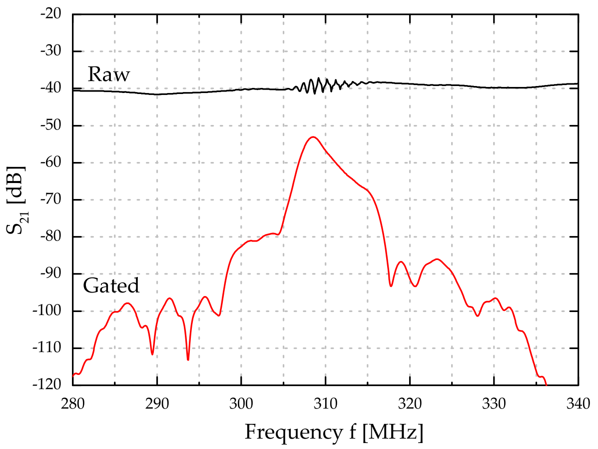

Figure 5.8: Typical raw and gated first impulse response spectra S_{21} for wavelength $\lambda = 16$ µm and distance $d = 4350$ µm for a SAW device with an AlN thickness $h_{AlN} = 2$ µm on silicon.

ature, the systems swings over and needs quite a long time to get stabilized. Due to the long time constant of about 45 min, the SAW measurements were performed during the swing over. More detailed information about the measurement setup are reported by Bardong *et al.* [149].

5.2 Aluminium Nitride

5.2.1 Substrate Effect

The substrate has a major influence on the SAW device performance. Figure 5.8 shows the raw S_{21} and the gated first impulse response signal for $\lambda = 16$ µm, a distance between transmitter and receiver of $d = 4350$ µm and an AlN thin film layer of $h_{AlN} =$ 2 µm on top of a silicon substrate. Compared to a device on sapphire, as illustrated in Figure 5.5, where the main resonance is clearly visible, the resonance lobe of the silicon-based devices is not recognizable and only some oscillations can be seen. This effect can be attributed to the capacitive feedthrough between transmitter and receiver caused by the conductive silicon substrate (n-doped, resistivity: >50 Ωcm) [150]. After gating of the first impulse response of the SAW signal in the time domain, the resonance frequency is determined.

Figure 5.9 shows the different phase velocities v_p for normalized thickness kh values,

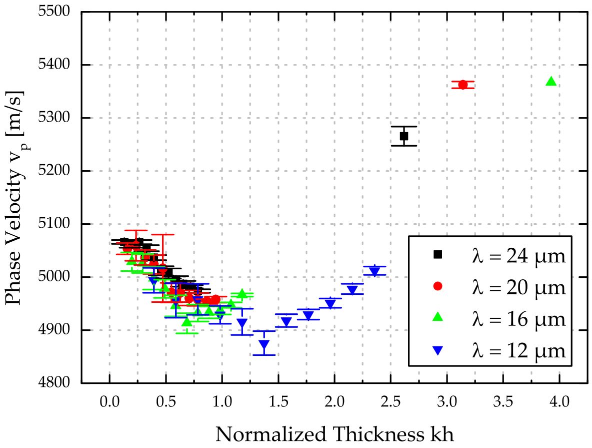

Figure 5.9: Measured phase velocity v_p as a function of normalized AlN thickness for SAW devices on silicon.

which are calculated according to:

$$kh = 2\pi h_{AlN}/\lambda \tag{5.7}$$

The AlN thickness was varied from $h_{AlN} = 500$ nm up to $h_{AlN} = 10$ µm. It can be seen that for low kh, the phase velocity is for all wavelength values in the range between 5050 m/s and 5100 m/s and decreases with larger normalized thickness values. Between $kh = 1$ and $kh = 1.5$ the phase velocity starts to rise again. It is reasonable to assume, that the influence of the AlN layer is low for lower kh values, because most of the SAW energy is traveling in the substrate [151]. With increasing values of kh, however, more energy is transferred into the AlN layer, which has a higher stiffness compared to silicon, which results in a larger phase velocity [152, 153]. The difference in phase velocity for the same normalized thickness kh can be attributed to mass loading effects of the electrode material, which will be deeper investigated in section 5.4. Figure 5.10 shows the dependency of v_p for different wave propagation directions on a (100) silicon substrate. An angle of 0° corresponds to the [011] direction of the silicon substrate, whereas an angle of +45° and -45° corresponds to the [100] and [010] direction, respectively. The phase velocity has the highest value for all equivalent $\langle 110 \rangle$ directions and decreases strongly for other directions. This can be attributed to the changing Young's modulus of silicon depending on the crystallographic direction [154]. Silicon has a Young's modulus of 169 GPa for $\langle 011 \rangle$ directions and 130 GPa for the $\langle 001 \rangle$ directions, which is a difference of ~23 %. This translates into a difference in the sound velocity according to $\Delta v_p \propto \sqrt{\Delta Y}$ of ~4.5 %, what is larger than the decrease

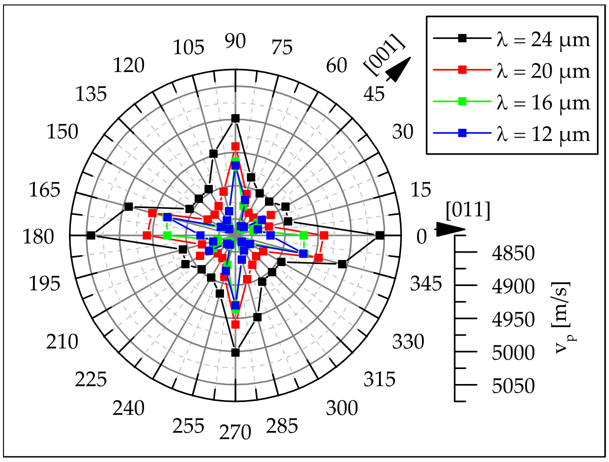

Figure 5.10: Phase velocity v_p dependency on the wave propagation direction with an AlN film thickness of 2 µm. An angle of 0° corresponds to the [011] direction of the silicon substrate.

of the measured phase velocity from the $\langle 011 \rangle$ to the $\langle 001 \rangle$ directions of about 1 %.

For c-plane sapphire substrates, the phase velocity increases with the normalized thickness as shown in Figure 5.11. Similar to the silicon based devices the differences in phase velocity for a given normalized thickness kh is attributed to mass loading effects and are investigated in section 5.4. The phase velocity itself is larger compared to silicon, due to a higher Young's modulus of sapphire. As observed on silicon, the phase velocity of the SAW test structures strongly depends on the crystallographic orientation of the sapphire substrate. For a deeper analysis, acoustic wave simulation for different directions were performed in section A.3. Figure 5.12 shows a high phase velocity for all equivalent $\langle 11\bar{2}0 \rangle$ directions of the c-plane sapphire substrate. For the m-direction $[10\bar{1}0]$ the phase velocity decreases from ~5690 m/s (a-direction) to ~5520 m/s (m-direction), indicating that for a proper SAW device design where a specific resonance frequency is targeted, the orientation of the substrate in wave propagation direction needs to be taken into account.

5.2.2 Pre-treatment of the Substrate Surface

With an ISE process step prior to sputter deposition of the AlN layer, the grain orientation and the piezoelectric constants can be improved, as discussed in section 3.2.1. In this section, the influence of not perfectly c-axis aligned AlN grains on the performance of SAW devices with a wavelength $\lambda = 16$ µm and $h_{AlN} = 500$ nm is investigated.

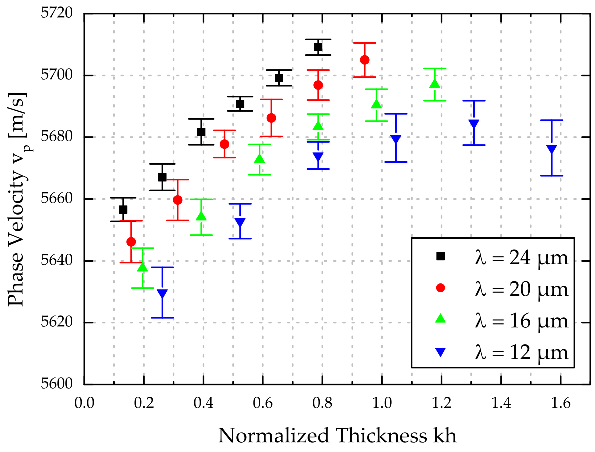

Figure 5.11: Phase velocity v_p dependency of the normalized AlN thickness kh on c-plane sapphire.

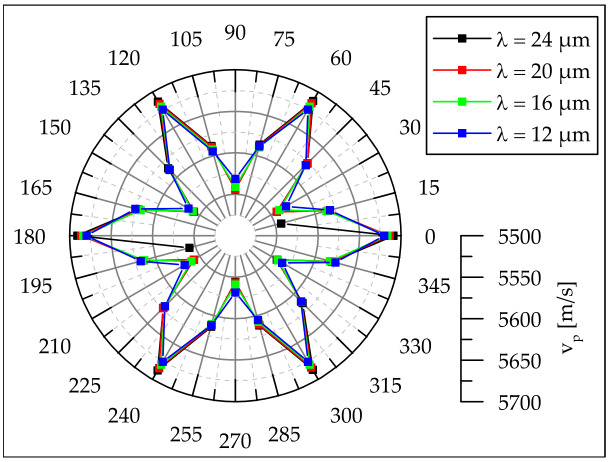

Figure 5.12: Dependency of the phase velocity v_p on wave propagation direction on c-plane sapphire. An angle of 0° corresponds to the $[11\bar{2}0]$ a-direction of the sapphire substrate.

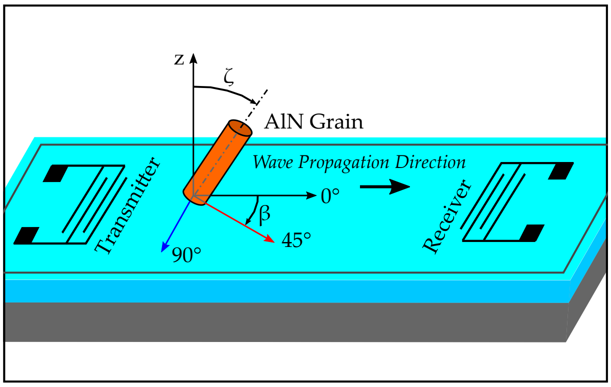

Figure 5.13: Schematic of defined angles needed when investigating the theoretical influence of tilted grains on the SAW phase velocity.

Therefore, FEM simulations of the resonance frequency shift f_0 due to the presence of tilted grains were performed. The modeling approach, basics of the mathematical procedure and the evaluation of the FEM simulations are given in appendix A.4. Figure 5.13 defines the tilting the angle ζ and tilting direction β of a SAW delay line device.

Figure 5.14 shows the impact on the simulated results in resonance frequency, when tilting the grains parallel ($\beta = 0°$) to, perpendicular ($\beta = 90°$) to and with $\beta = 45°$ relative to the wave propagation direction. The wave propagation direction is along the a-direction $[11\bar{2}0]$ of a c-plane sapphire substrate. With an increasing tilt angle ζ of the grains along the wave propagation direction, the resonance frequency decreases from originally $f_0 = 354.9$ MHz to $f_0 = 354.74$ MHz at an angle ζ of 25°. Above, the device parameter f_0 increases up to 355.38 MHz, which is even larger than at $\zeta = 0°$. A tilt perpendicular to the wave propagation direction, results in a continuously decreasing resonance frequency, leading to $f_0 = 354.54$ MHz at a tilting angle ζ of 55°. The change of the resonance frequency can be attributed to the effective change in the stiffness values, resulting in a change in the sound velocity in the AlN layer. When tilting the grains along $\beta = 45°$ of the wave propagation direction the resonance frequency f_0 curve is nearly the same as in the wave propagation direction ($\beta = 0°$).

To estimate the influence of misaligned grains in the sputtered AlN layer, a modified compliance matrix was used. The compliance matrix reported by Tsubouchi was tilted along the wave propagation direction by the angle ω between -30° and +30° [139], written in matrix form $\boldsymbol{C}(\omega)$. This matrix was integrated and weighted by the rocking curve intensity distribution $I(\omega)$ for SAW devices pretreated either by ultrasonics (T1) or by ISE (T2) as introduced in section 3.2.1 (Figure 3.4(b)), ac-

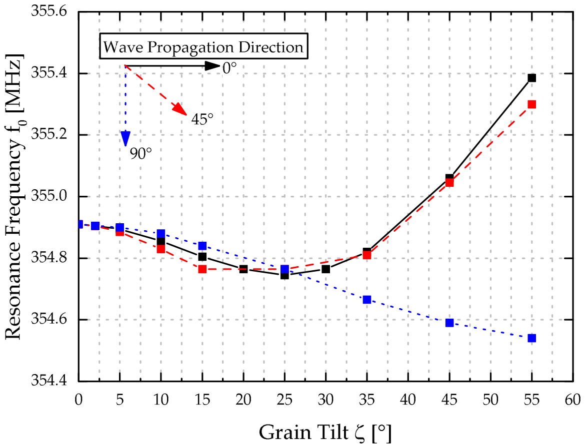

Figure 5.14: Theoretically predicted impact of AlN grain orientation (i.e. parallel, perpendicular and 45° tilt) on the resonance frequency shift, if wave propagation is on c-plane sapphire in $[11\bar{2}0]$ a-direction.

cording to $C_{sim} = \int_{-30^o}^{+30^o} \boldsymbol{C}(\omega)I(\omega)d\omega$. The AlN-related material parameters such as compliance matrix used for the simulations are given in the appendix A.2. For the ISE and the ultrasonic pre-treatment method, the simulated resonance frequency decreases from $f_0 = 354.9$ MHz (i.e. all grains are perfectly aligned to $\omega = 0°$) down to $f_0 = 354.72$ MHz (ISE pre-treatment) and $f_0 = 354.73$ MHz (ultrasonics pre-treatment). The difference between the resonance frequencies is low, which is in good agreement with the measured resonance frequencies of fabricated samples, namely $f_0 = 354.84$ MHz and $f_0 = 355.32$ MHz for the sample with ISE and ultrasonic pre-treatment, respectively.

Figure 5.15 shows the impulse response signals for SAW devices pre-treated with ultrasonics (a-c) and ISE (d-f) having distances between transmitter and receiver ranging from 2175 µm up to 6525 µm. For those, which where pre-treated with ISE, the triple-transit signal and even the quintuple-transit signal are measured. The energy loss between each transited signal is around -20 dB and is mainly attributed to the transformation losses in the IDTs, because the drop is nearly independent of the transmitter and receiver distance. In contrast, the signals of the ultrasonically pre-treatment devices are so heavily damped, that no triple-transit signal can be measured. The difference in the magnitude of the first impulse peak compared to the ISE pre-treated devices is around -20 dB. This means that signal damping is increased by 20 dB for one signal transit and thus by 60 dB for a triple transit and hence, pushing the triple-transit

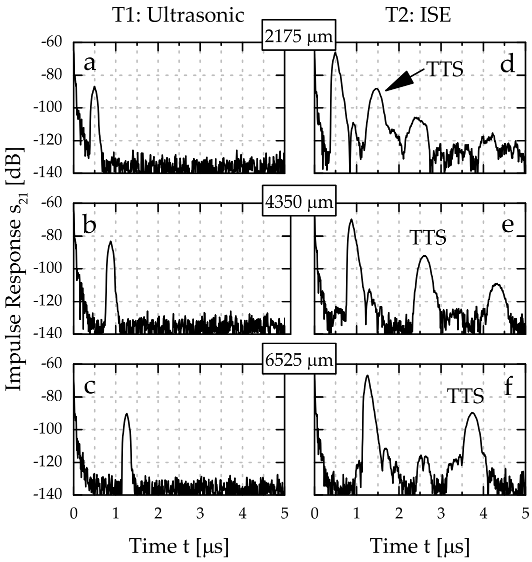

Figure 5.15: Impulse response s_{21} of SAW devices having different pre-treatments and different distances between transmitter and receiver at a wavelength $\lambda = 16$ µm.

signal below the base line of the measurement signal. Figure 5.16(a) shows in detail the signal level of the first-transit (FTS), triple-transit (TTS) and quintuple-transit(QTS) for different distances between transmitter and receiver for T2 devices and a wavelength of 16 µm. It can be seen that in a range of variation, no detectable propagation losses depending on the distance are observed. Consequently, the most losses are during the energy transformation in the IDT's. A better visualization of the signal level of the FTS, TTS, QTS, sevenfold-transit (STS) and ninefold-transit (NTS) signal for different wavelength is shown in Figure 5.16(b). The mean values are calculated over different distances between transmitter and receiver, because the distance has a minor influence on the damping of the signal as mentioned before. At first, it can be seen for both T1 and T2, that the wavelength has an influence on the transduction loses. A continuous increase of the wavelength in 4 µm steps increases the damping in steps by roughly 6 dB for the FTS and additionally for all T2 samples by 2-3 dB for the TTS. By comparing the FTS for both methods, an offset of -20 dB is measured in T1 devices for all wavelengths. When taking the accumulation of these additional transduction losses at each IDT into account, it is clear that the TTS signal of the T1 devices is damped by -60dB and thus below the measurement limit of around -125 dB. The energy loss of the TTS and of the QTS signals for T2 devices is approximately -20 dB per double transit. The

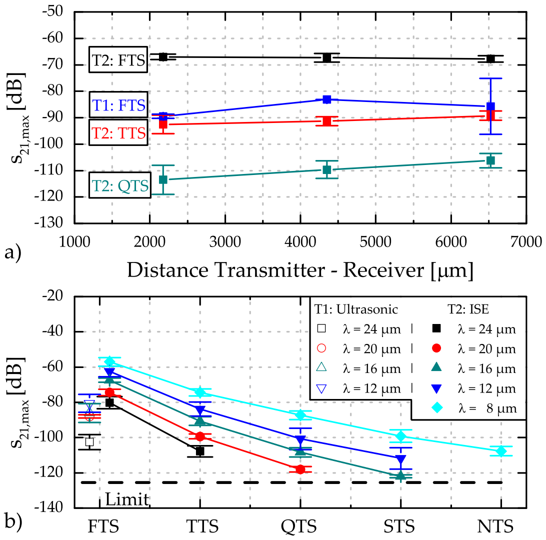

Figure 5.16: (a) Damping range of SAW signals for different distances between transmitter and receiver for a wavelength of 16 µm. (b) Damping of the SAW signal after the first-transit (FTS), triple-transit (TTS), quintuple-transit (QTS), sevenfold-transit (STS) and ninefold-transit (NTS) for the ultrasonic and ISE pre-treatment.

signal can be detected until it reaches the lower limit, which means for a wavelength of 24 µm that only the TTS signal could be measured, whereas for a $\lambda = 8$ µm even the ninefold-transit signal is measureable.

It is reasonable to assume, that with a lower AlN quality (e.g. higher leakage current behavior, lower grain homogeneity), parasitic effects are increased [49, 65].

5.3 Scandium Doped Aluminum Nitride

To enhance the piezoelectric coefficients d_{31} and d_{33} by a factor of ~3, AlN is doped with scandium by using an alloyed target of 27 $\%_{at}$ scandium and 73 $\%_{at}$ aluminum for film synthetization [153, 155, 156]. Higher piezoelectric coefficients lead at a given excitation voltage to a significant increase of the mechanical deformation of the crystal structure and hence, to a better signal to noise ratio at the receiver. Figure 5.17 shows the phase velocity v_p on silicon based devices as a function of the normalized thickness kh. The overall phase velocity is around 100 m/s lower compared to a similar device design with pure AlN, see Figure 5.9. The difference in the phase velocity between pure

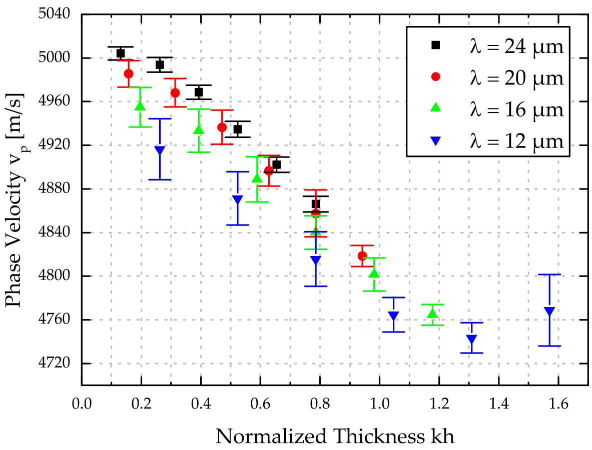

Figure 5.17: Phase velocity v_p as a function normalized thickness kh of AlScN on silicon.

and scandium doped AlN is attributed to the lower Young's modulus of ~306 GPa of the AlScN layer compared to ~345 GPa of AlN [139, 156]. The phase velocity decreases for AlScN layers with layer thicknesses up to $kh = 1.2$. Above, the phase velocity starts to increase again. The same behavior is observed for pure AlN layers (see Figure 5.9).

Figure 5.18 shows the phase velocity v_p with respect to the wave propagation direction along different crystallographic orientations. 0° indicates the [011] direction on a (100)-plane silicon wafer. The behavior is similar to the AlN layer, where in the $\langle 011 \rangle$ directions a higher phase velocity is reached. For other direction besides $\langle 011 \rangle$ the phase velocity is lower. For example SAW devices with a wavelength $\lambda = 24$ µm, the phase velocity deceases from 4935 m/s to 4849 m/s. A reason is the different Young's modulus of the substrate in wave propagation direction.

AlScN SAW devices were also fabricated on c-plane sapphire substrates. Figure 5.19 shows the phase velocity as a function of the normalized thickness kh. As expected, the phase velocity decreases with increasing thickness of the AlScN layer, because a higher portion of the wave propagates inside the piezoelectric layer (see Figure 5.2). The maximum phase velocity $v_p = 5669$ m/s was achieved at a wavelength $\lambda = 24$ µm and an AlScN thickness $h = 500$ nm which corresponds to a normalized thickness $kh = 0.13$. It is reasonable to assume, that due to the large wavelength and thin AlN layer most of the wave energy is traveling inside the substrate, which has a higher Young's modulus and therefore the overall effective modulus is higher.

Figure 5.20 shows the dependency of the phase velocity on the wave propagation

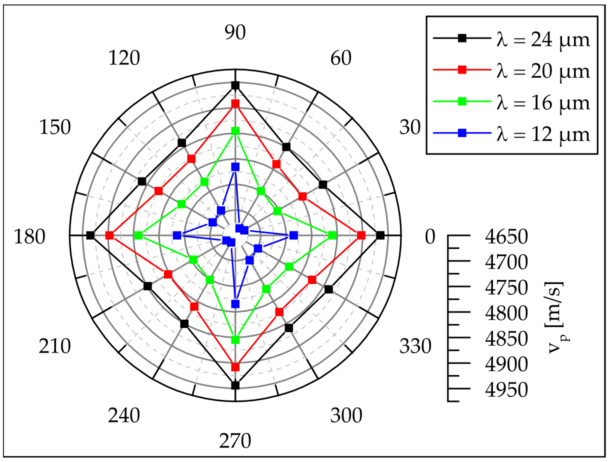

Figure 5.18: Angle dependence of the phase velocity v_p of AlScN-based SAW devices with a thickness $h = 2$ µm on (100) silicon. An angle of 0° corresponds to the [011] direction.

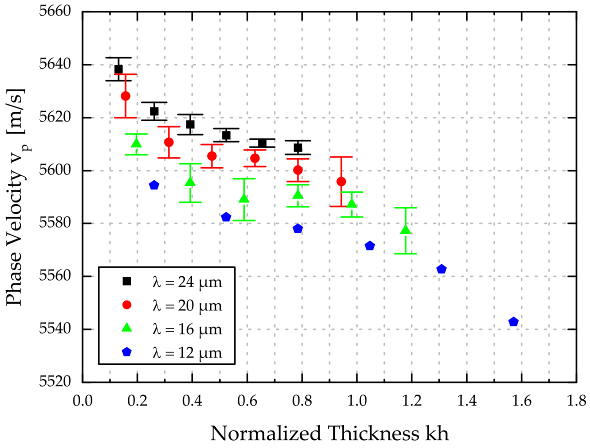

Figure 5.19: Phase velocity v_p as a function of the normalized thickness kh of AlScN-based SAW devices on c-plane sapphire.

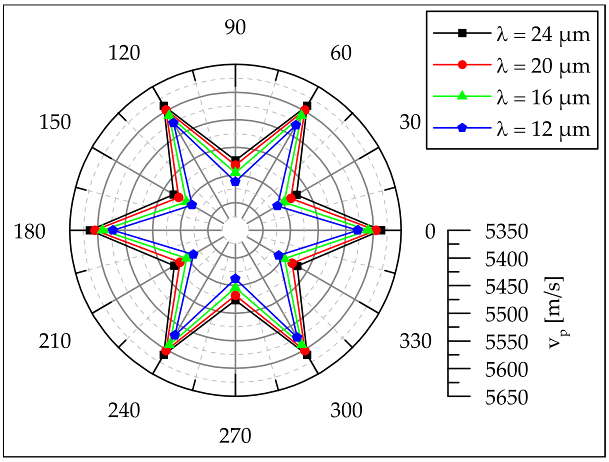

Figure 5.20: Dependency of the phase velocity v_p for different wave propagation directions with an AlScN thickness $h = 2$ µm. An angle of 0° corresponds to the $[11\bar{2}0]$ direction on a c-plane sapphire substrate.

direction. 0° corresponds to the $[11\bar{2}0]$ direction on a c-plane sapphire substrate. The phase velocity is anisotropic and shows the highest value in all a-directions. It decreases by approximately 2.5% in all m-directions of the hexagonal crystallographic structure of the sapphire substrate. This can be directly linked to the different stiffness values associated with different directions, which is discussed in detail in section A.3, where the phase velocity is calculated for devices on sapphire.

5.4 Mass Loading Effects

The substrate material has an influence on the phase velocity, as shown in the previous sections 5.2 and 5.3. This chapter deals with the influence of additional material on top of the piezoelectric thin film. Two kinds of additional layers are addressed, namely the conductive electrode and the passivation layer.

5.4.1 Electrode Layer

Important device components on top of the piezoelectric thin film are the inter-digital transducer elements. These IDTs consist of a conductive material, which can be aluminum, copper or a high temperature resistant material like platinum or iridium, especially when targeting harsh environmental applications. Figure 5.21 shows measurement and simulation results of SAW devices with AlScN as the piezoelectric ma-

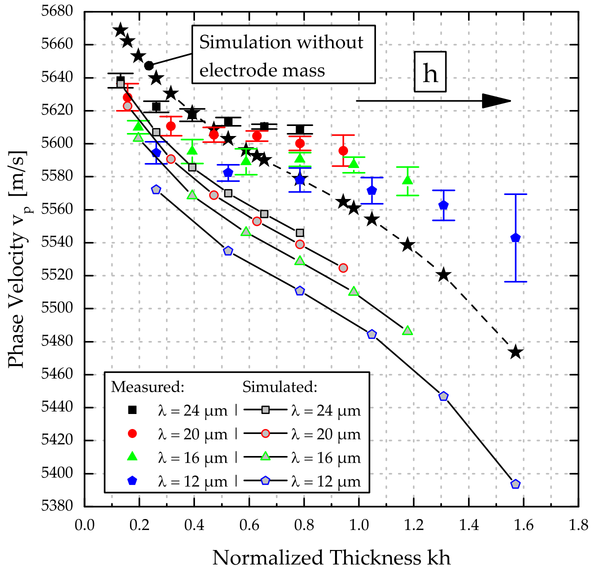

Figure 5.21: Measured and simulated phase velocities v_p of AlScN SAW devices as a function of normalized thickness kh [124].

terial on sapphire with platinum electrodes. The thickness of the IDTs was chosen to $d = 50$ nm independent of the wavelength. It can be seen, that for the same normalized thickness kh and different wavelengths λ the phase velocity v_p differs. The simulations show that the reason is due to mass loading, caused by the platinum electrode material, as simulations with an electrode mass of zero indicate no difference in the phase velocities for a given kh value and different wavelength. The measurement as well the simulation results also exhibit, that for a higher normalized thickness kh the signal damping effect is increased at larger wavelengths. The different slopes between the measured and simulated values can be explained by the not perfectly matched AlScN material parameters, which were derived from *ab initio* simulations, reported by Mayrhofer *et al.* [156] and are given in the appendix A.2.

5.4.2 Passivation Layer

As demonstrated in the previous section 5.4.1, additional weight due to the electrode material on top of the piezoelectric layer reduces the phase velocity. However, for harsh environments, these fragile and thin electrodes have to be covered and protected by an additional passivation layer when targeting reliable and long-term operation of the SAW devices. Therefore, three different materials (Si_xN_y, Al_xO_y and AlN) were deposited on SAW structures. As shown in chapter 4, Si_xN_y promises the best oxidation resistance up to 1000°C. Nevertheless, for lower temperatures up to 700 °C, both AlN and Al_xO_y can also be used, to reduce the number of different materials involved to a minimum and hence, the impact of thermo-mechanical stress arising from different temperature coefficients of thermal expansion. The sputter parameters for the passivation layers are listed in section 4.4. Figure 5.22 shows the shift of the phase velocity v_p as a function of both the type and the thickness of the deposited passivation layer. Al_xO_y shows the highest damping in phase velocity per unit of the passivation layer thickness of around -0.41 m/s·nm for a wavelength of 12 µm, whereas for increasing wavelength the damping of the phase velocity is decreased. At $\lambda = 24$ µm, the damping for increasing passivation layer thickness is at around -0.20 m/s·nm. Si_xN_y shows the same effect where a shift from -0.39 m/s·nm ($\lambda = 12$ µm) down to -0.22 m/s·nm ($\lambda = 24$ µm) is observed. The lowest influence on the phase velocity is observed by AlN, where the damping is -0.35 m/s·nm and -0.17 m/s·nm for $\lambda = 12$ µm and $\lambda = 24$ µm, respectively. It is reasonable to assume, that when increasing the operation frequency more mechanical energy is transported in the passivation layer and hence, the stiffness of the passivation layer has more influence on the overall effective stiffness, the waves experience.

5.5 High Temperature Measurements

In the following section, the influence of high temperature loading on the performance of SAW devices in varying atmospheres is investigated. Two approaches are done, namely SAW device characterization *in situ* or before and after an annealing step. At first, devices on different substrates like silicon or sapphire are analyzed. Furthermore, the piezoelectric AlN layer was replaced by AlScN, to evaluate the impact of higher piezoelectric coefficients on the output signals characteristics. Finally, to improve the high temperature stability, SAW devices with Al_xN_y and Si_xN_y passivation coatings are fabricated and measured.

5.5.1 Impact of Substrate Type

As seen in section 5.2.1, SAW devices on silicon show a poor signal-to-noise ratio in the raw signal characteristics due to the increased electromagnetic crosstalk, such that

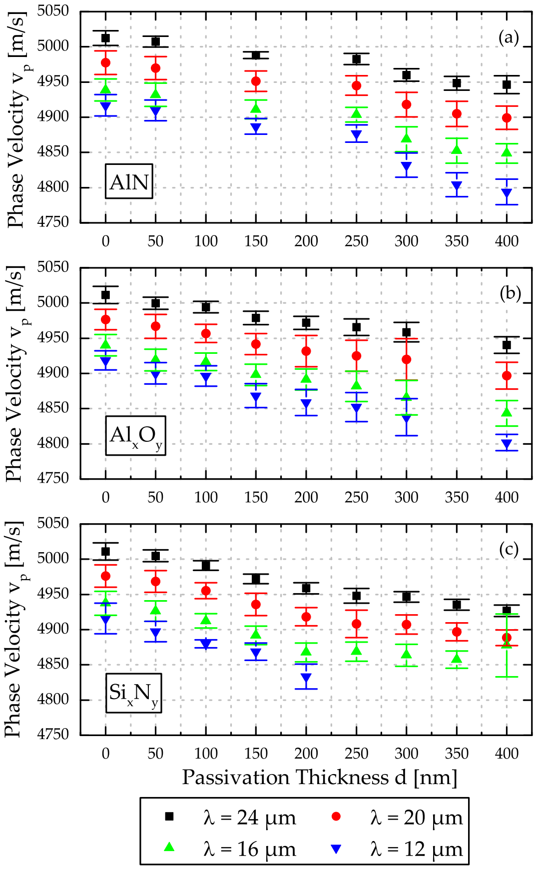

Figure 5.22: Phase velocity shift v_p caused by an additional Si_xN_y, Al_xO_y and AlN as passivation layer on top of the SAW structure.

only a signal oscillation at the resonance frequency is detected. For devices on sapphire having the same geometrical dimensions, a clear main lobe is measured. In Figure 5.23 gated S_{21} measurements both on sapphire (a) and silicon (b) are shown. The measurements on both substrate types were performed from 25 °C up to about 810 °C in steps of about 200 °C for both materials. The thickness of the piezoelectric AlN thin film layer was $h_{AlN} = 2$ µm with a IDT wavelength $\lambda = 16$ µm. For sapphire a signal up to the maximum measured temperature can be observed with a resonance frequency shift indicated by arrows. The shift in the resonance frequency is attributed to the temperature-induced change in device length as well as in the modification of the mechanical stiffness of the materials involved [157]. The difference in insertion loss may be due to small variations of the contact resistance, due to the reconnection of the devices between each measurement step. For the silicon-based device architecture, the signal at $T_M = 216$ °C is still measurable and vanishes completely at $T_M = 464$ °C. Up to 216 °C the temperature coefficient of resonance frequency is 5.2 kHz/°C. After temperature loading, the SAW device still works at room temperature, as seen in Figure 5.23(b). At higher temperatures, the electrical conductivity of the silicon substrate increases and therefore the electromagnetic crosstalk is increased, leading to a higher energy loss and hence, less energy is transferred into the mechanical wave, so that the SAW signal disappears. The silicon system is therefore not suited for such high temperature measurements, but can be used to evaluate the degeneration of the deposited layers with pre- and post- annealing measurements. The results of such investigation are reported in the section 5.5.4.

In contrast to the previous investigations, Figure 5.24 shows continuous high temperature measurements. With increasing temperature, the resonance frequency decreases, due to expansion of the materials and the decrease of the stiffness of the various materials. Starting at $T_M = 600$°C modifications of the electrode material occur, which lead to lower signal losses. These trend changes again starting at $T_M = 800$ °C, where the electrode material properties are modified such that a dramatically drop of the output signals occurs. These additional losses do not recover after having decreased the applied temperature. Furthermore, it is reasonable to assume, that an additional modification of the piezoelectric layer occurs due to the diffusion of gaseous specimens from the air atmosphere into the layer, which causes changes for example in the intrinsic stress, leakage current or surface modification (see section 3.3). The latter modification may change the effective Young's modulus of the device, resulting

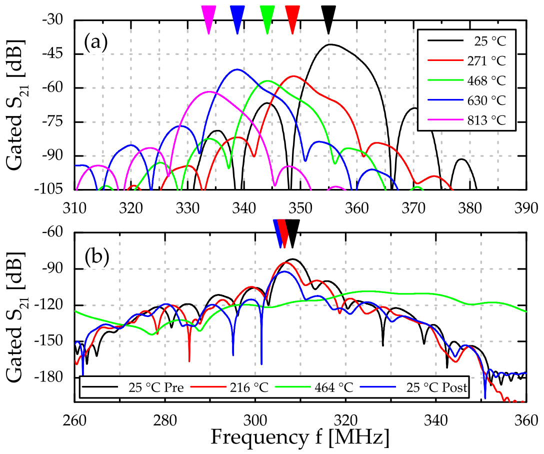

Figure 5.23: High temperature S_{21} measurements of AlN SAW devices on sapphire (a) and silicon (b) substrates with a 40 nm thin Ti/Pt bilayer electrode. The arrows indicate the position of the main resonance frequency.

in a direct influence on the phase velocity according to $v_p \propto \sqrt{Y}$. As a result, a resonance frequency shift at a given measurement temperature occurs between heating up and cooling down cycle. For reason of comparison, only the heating up ramp will be evaluated in the following sections, as similar results are gain from the cooling down phase.

5.5.2 High temperature performance of AlN and AlScN-based SAW devices

To analyze the influence of scandium doped AlN compared to pure AlN on SAW performance at elevated temperatures, devices based on both materials with 2 µm layer thickness and a wavelength of $\lambda = 16$ µm were fabricated. As electrode material, a combination of tantalum as adhesion promoter and platinum as the conductive material was used. In Figure 5.25 the evaluated resonance frequency as a function of temperature is shown. The difference in the absolute maximum resonance frequencies ~354 MHz for AlN and ~348 MHz for AlScN can be explained by the different Young's moduli of ~345 GPa and ~306 GPa, respectively [139, 156]. The measurement starts at room temperatures and goes up to ~820 °C in steps of around 200 °C. The temperature coefficient of resonance frequency (TCF) is -27.62 kHz/°C for the device with AlN and -27.81 kHz/°C for AlScN. Independent of the active material both device types behave similar, as sapphire serves as substrate. Compared to literature, the TCF is around $(f - f_0)/f_0 = -78$ ppm/°C, which is in good agreement with devices from Legrani

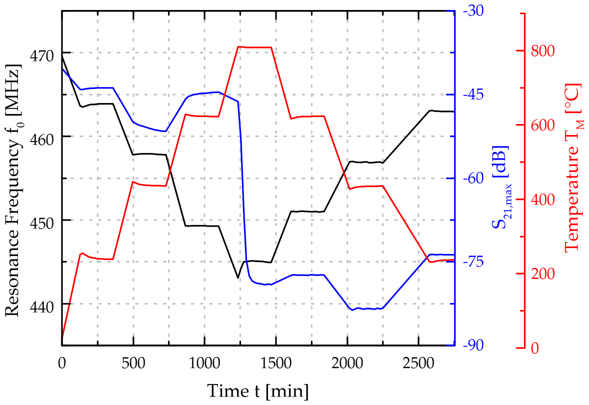

Figure 5.24: High temperature SAW characterization showing resonance frequency and $S_{21,max}$ as a function of measurement temperature. Devices were fabricated with 2 µm AlN on sapphire and a total TiN/Pt electrode multilayer thickness of 40 nm and a wavelength of $\lambda = 12$ µm without a passivation layer.

et al. [158]. Both piezoelectric materials in combination with sapphire proved enough temperature robustness to be operated up to temperatures of 820 °C.

5.5.3 Passivation Layers

Gaseous oxygen (e.g. from the air) can cause especially at elevated temperatures sever damage due to undesired oxidation of functional device layers during operation. These undesired influence of oxygen on the key material properties such as piezoelectric coefficient, intrinsic stress, surface morphology or leakage current are shown in section 3.3 and section 4.3 for the piezoelectric AlN and the electrode layer, respectively. As shown in section 4.4, a passivation layer can protect these elements like the piezoelectric AlN and the electrode layer against such effects like oxidation or delamination. On the other hand, an additional layer has a direct influence on the phase velocity (see section 5.4.2 for different passivation layers). To investigate the high temperature performance of passivated SAWs, devices with Al_xO_y and Si_xN_y as coatings having a thickness of $d = 100$ nm were fabricated and measured from 25 °C up to around 820 °C in argon atmosphere. The wavelength of the IDT's was $\lambda = 16$ µm with an electrode bi-layer of 5 nm tantalum and 40 nm platinum on top of a 2 µm piezoelectric AlN layer. Figure 5.26 shows the resonance frequency as a function of measurement temperature. The

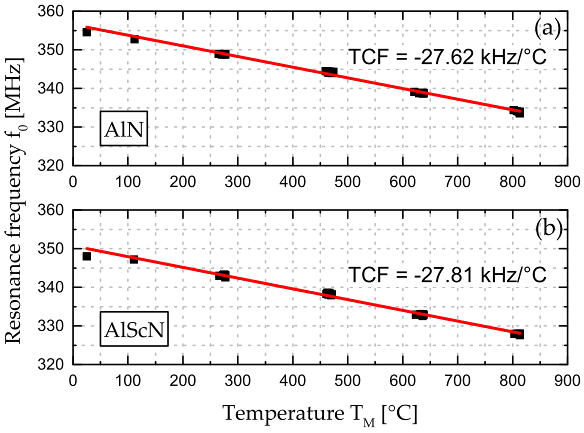

Figure 5.25: Temperature dependence of the resonance frequency TCF of SAW devices on sapphire with AlN (a) and in addition with AlScN (b) as piezoelectric material with a wavelength $\lambda = 16$ µm of the IDT's.

temperature coefficient of resonance frequency (TCF) is -26.23 kHz/°C (-56 ppm/°C) for Al_xO_y and -25.37 kHz/°C (-54 ppm/°C) for Si_xN_y. The difference compared to the device without passivation is around $\Delta TCF = 0.39$ kHz/°C and 1.25 kHz/°C, respectively. The influence of an additional $d = 100$ nm passivation layer is ~1.5 % (Al_xO_y) and ~4.9 % (Si_xN_y). As a result of the additional coating material, the sensitivity of the system is reduced by ~23 ppm/°C.

5.5.4 Oxygen Atmosphere

In order to evaluate the performance under harsh oxidizing environments, SAW devices with and without passivation layer were fabricated. The thickness of the piezoelectric AlN thin film was fixed to $h_{AlN} = 2$ µm on silicon. Silicon was chosen due to a better availability of the substrate material and due to the fact that SAW characterization before and after the annealing gives valuable feedback on the basic functionality, as shown in Figure 5.23. For annealing temperatures $T_A = 600$ °C and $T_A = 700$ °C devices with a wavelength of $\lambda = 20$ µm were selected, whereas for $T_A = 800$ °C up to $T_A = 1000$ °C devices with a wavelength of $\lambda = 16$ µm are used. This variation in the wavelength with approximately the same phase velocity guarantees a better coverage of a targeted frequency bandwidth for further applications, being between 240 MHz and 340 MHz. Devices were placed for 24 hours in a furnace at different annealing temperatures and pure oxygen atmosphere under a constant oxygen flow of 100 sccm. The

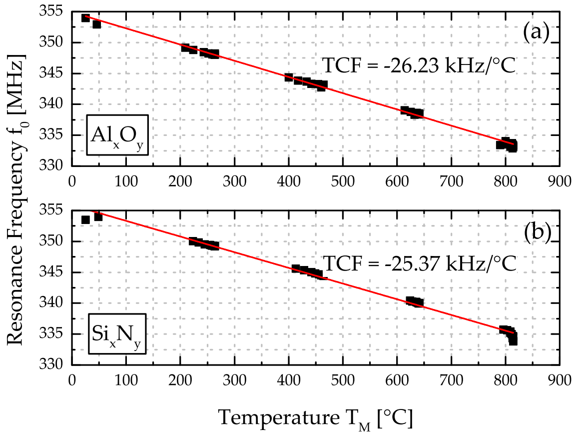

Figure 5.26: Temperature dependence of the resonance frequency of SAW devices at a wavelength $\lambda = 16$ µm with additional Al_xO_y and Si_xN_y coatings as passivation having a thickness $d = 100$ nm.

robustness was tested by measuring the main lobe. Therefore, the resonance frequency was measured prior to the deposition of the passivation layer, before the annealing step and after the annealing step. If the main lobe is not measurable after the annealing step, the sample was marked as failure. Figure 5.27 shows typical S_{21} parameter measurements for samples before deposition of a passivation layer (*as fab.*) and with a 50 nm Si_xN_y passivation layer before (*pre*) and after the annealing step (*post*). Even after $T_A = 700$ °C the sample shows a signal after the harsh environmental load and is confirmed as still working SAW device. This result is in contrast to the sample after $T_A = 800$ °C, where the signal vanished and therefore is declared as failure.

The following Table 5.1 shows at which temperature the different devices fail. Without passivation, the devices withstand a maximum annealing temperature of 600 °C. With a 50 nm thin AlN passivation layer annealing temperatures up to 800 °C are possible. When increasing the thickness of the coating a maximum of 700 °C is achieved. A reason could be the additional thermal induced intrinsic stress, which leads to delamination effects. On the other hand, Si_xN_y showed in section 4.4 good passivation properties up to 1000 °C, but on top of the SAW device only temperatures up to 700 °C could be realized before device failure. Above this temperature range, none of the devices worked after temperature loading. Al_xO_y reaches only with a thickness of 50 nm an annealing temperature of 800 °C. Above 100 nm, all devices failed, only the devices with a 250 nm passivation thickness survived $T_A = 600$ °C.

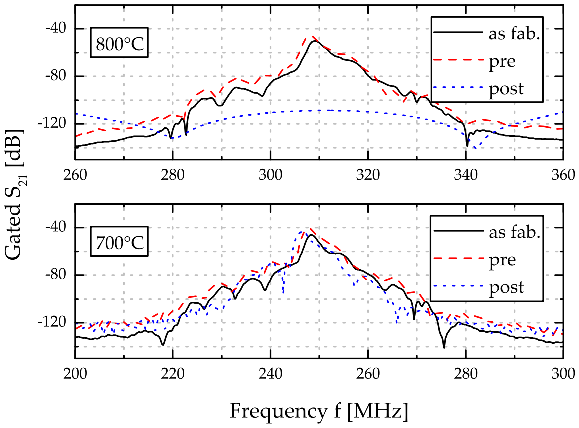

Figure 5.27: Typical S_{21} parameter measurements for SAW devices without passivation (*as fab.*), and with a 50 nm Si_xN_y passivation layer before (*pre*) and after (*post*) high temperature annealing in oxygen for 24 hours at of $T_A = 700$ °C ($\lambda = 20$ µm) and $T_A = 800$ °C ($\lambda = 16$ µm).

Table 5.1: Overview on the SAW device failure for selected passivation layer materials and thicknesses after annealing at varying temperatures in oxygen atmosphere for 24 hours.

Passivation Layer	Thickness [nm]	600 °C	700 °C	800 °C	900 °C	1000 °C
None	0	✓	-	-	-	-
AlN	50	✓	✓	✓	-	-
AlN	150	✓	✓	-	-	-
AlN	250	✓	✓	-	-	-
AlN	400	✓	✓	-	-	-
Al_xO_y	50	✓	✓	✓	-	-
Al_xO_y	100	-	-	-	-	-
Al_xO_y	250	✓	-	-	-	-
Al_xO_y	400	-	-	-	-	-
Si_xN_y	50	✓	✓	-	-	-
Si_xN_y	100	✓	✓	-	-	-
Si_xN_y	250	✓	✓	-	-	-
Si_xN_y	400	✓	✓	-	-	-

To investigate the reason of failure, optical analysis of the devices was performed. Figure 5.28 shows images of annealed devices with passivation layers of Si_xN_y and Al_xO_y. At $T_A = 600$ °C for $d = 100$ nm Si_xN_y the connection pads as well as the passivation layer on top of the IDT's show no indications of degeneration, as illustrated in Figure 5.28(a). If T_A is increased to 800 °C, delamination of the passivation layer deposited above the electrode and the contact pads starts to occur. Such delamination of the connection pads can be seen for 350 nm Al_xO_y in Figure 5.28(b), which was annealed at 700 °C. The passivation layer delaminates itself from the electrodes, which leads to locale flake formation, as can be seen for 100 nm Si_xN_y after 800 °C load in Figure 5.28(c1). The electrode starts to de-wet, indicated by the black holes in Figure 5.28(c2). After $T_A = 1000$ °C, however, the whole device looks different. The passivation layer and perhaps even the AlN layer arranged below oxidize to a certain degree, indicated by the different colored reflection of the layers (see Figure 5.28(d1)). The contact electrode, however, oxidizes and generates volatile gaseous PtO_2 (see section 4.1). For the electrode material below the passivation layer, it is difficult to determine, if it is still there or already diffuse inside the AlN layer, which changes the reflection index and hence, only a shadow is visible (see Figure 5.28(d1-2)). In contrast to the results of section 4.4, where the active AlN layer was successfully protected by the Si_xN_y in oxygen atmosphere for 24 hours, the passivation is not that effective, on device level. It is reasonable to assume, that with the additional electrode layer between the AlN and the Si_xN_y additional stress inside the layer is generated, which leads to a lower diffusion resistance and hence, oxygen can diffuse to the layers arranged below. Additionally to these effects, the different temperature coefficients of expansion of the materials involved generate further stress especially at the interface between different layers. As a result of the additional stress component, the adhesion is reduced and the layers delaminate. For Al_xO_y as passivation layer the result is similar. Figure 5.28(e1-2) shows a device with a 250 nm thin film after temperature loading at 900 °C. It can be seen, that bubbles-type structures are formed on top the Al_xO_y electrode material with partial delamination of the layer. As both systems are showing delamination effects at elevated temperatures, Si_xN_y is preferred as passivation layer due to its better adhesion and its overall robustness.

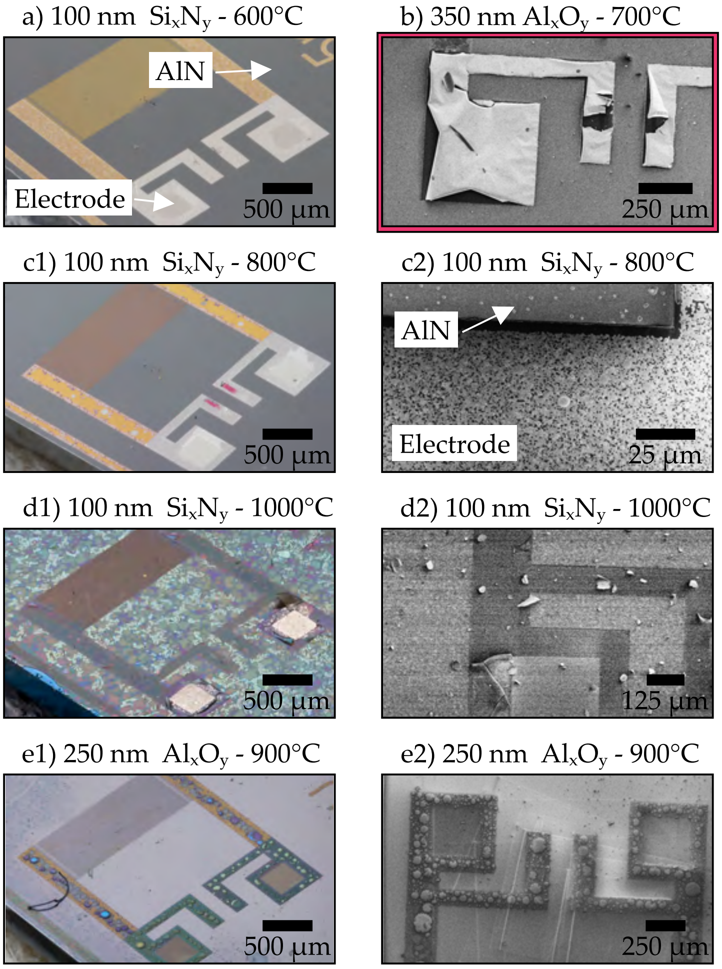

a) 100 nm Si_xN_y - 600°C

b) 350 nm Al_xO_y - 700°C

c1) 100 nm Si_xN_y - 800°C

c2) 100 nm Si_xN_y - 800°C

d1) 100 nm Si_xN_y - 1000°C

d2) 100 nm Si_xN_y - 1000°C

e1) 250 nm Al_xO_y - 900°C

e2) 250 nm Al_xO_y - 900°C

Figure 5.28: Optical microscope and SEM images of annealed samples in oxygen atmosphere. 100 nm Si_xN_y at $T_A = 600$ °C (a), 350 nm Al_xO_y at $T_A = 700$ °C (b), 100 nm Si_xN_y at $T_A = 800$ °C (c) and $T_A = 1000$ °C (d) and also Al_xO_y with a thickness $d = 250$ nm at $T_A = 900$ °C (e).

5.6 Conclusions

The combination of high temperature robust materials like the piezoelectric AlN thin film on top of sapphire offers the opportunity to fabricate SAW devices for harsh environmental applications with high phase velocities. AlN itself showed high resistivity against diffusion and hence, is robust against any changes of the intrinsic stress up to 600 °C. This limit of 600 °C can be expanded with Si_xN_y as a passivation layer on top of the structure. The passivation layer prevents any oxidation of the AlN layer during an annealing sequence for 24 hour at 1000 °C, but it failed if an additional electrode layer is placed between the AlN and the passivation layer, as needed in a SAW device architecture. This can be attributed to a low adhesion between the different layers, because delamination effects occurred at temperatures above 700 °C. AlN and Al_xO_y are not recommended as barriers against oxygen diffusion, because AlN oxidizes as shown in section 3.3.3 and the alumina layer only delays the oxidation process. At lower temperatures levels up to 600 °C, AlN may be used as a passivation layer as a possible solution against dewetting of the electrode layer. Doing so, the number of different materials in the device architecture is reduced to a minimum, when operated in an atmosphere consisting of inert gas. Therefore, the most promising material, which was studied, is Si_xN_y. It protects the active layers best within this study, but the adhesion to the electrode material is poor and further investigations have to be done on this aspect. Furthermore, the combination of piezoelectric AlN films on top of sapphire offers higher phase velocities by a factor of 2 compared to commercially used materials such as langasite. Finally, the electrode material is of major importance to SAW devices. During high temperature load in inert or chemically aggressive atmospheres, the thin metallization lines get degenerated. Platinum and iridium were chosen, because of the high melting point with good electrical performance. The disadvantage of these materials is their high density, which leads to a reduction in phase velocity and a shift in the resonance frequency due to the mass loading effect.

6 CONCLUSIONS AND OUTLOOK

6.1 Conclusions

Surface acoustic wave devices are well established now for several decades. They are mainly used in the telecommunication sector as frequency filter or signal delay lines. For several years, SAW devices are additionally investigated for high temperature application. A high potential as robust active layer for sensor and actuator systems shows reactive sputter deposited AlN. Annealing experiments revealed a stable micro structure in varying gas atmospheres up to 700 °C. At higher temperatures, however, oxidation or diffusion of gaseous constituents like oxygen or nitrogen from the corresponding annealing atmosphere into the layer is observed, resulting in film degeneration. In oxygen atmosphere the film changes the chemical composition from pure AlN to alumina. Furthermore, the leakage current behavior changes from dominating Pool-Frenkel towards a combination of different mechanisms. At an annealing temperature of 1000 °C, a 500 nm thin AlN film is completely oxidized after about 3 hours. At thicker AlN layers, this effect is only delayed, since the oxidation starts at the surface. Overall, AlN thin film layers promise reliable operation in harsh environments with temperatures up to 700 °C without measurable degeneration.

For a reliable operation of electrical devices, also conductive materials need to withstand the harsh environmental conditions. Common material like aluminum are not suited due to their low melting point of 660 °C. Therefore, high temperature stable materials like platinum or iridium are the typical candidates of choice. These materials show a stable behavior up to temperatures of around 700 °C. Above, oxidation, agglomeration and desorption of the thin film layers are observed, which is accompanied with an increase in electrical film resistivity. In agreement with the Thornton structure model, the deposited platinum films feature a Zone *T* morphology, which means, that during the deposition a lot of defects are generated, leading to a higher film resistivity compared to the bulk value. During high temperature loading, these defects are getting annealed, what decreases the resistivity of the electrode metallization. This effect was not observed with iridium. A reason could be the higher melting point of iridium (bulk, 2446 °C) compared to platinum (bulk, 1768 °C). To further improve the high temperature stability, investigations of reactively sputtered passivation coatings were performed. Similar to the piezoelectric layer, an AlN passivation oxidizes at higher temperatures and can only be used up to 700 °C, where no oxidation was observed. Therefore, this material can only be used to prevent dewetting of the conductive paths. Reactively sputtered Al_xO_y shows similar properties compared to AlN, because oxygen diffuses through the layer. Compared to Al_xO_y, the latter layer slows down the oxidation process at 1000 °C by a factor of 3 determined at 500 nm thin AlN layers, but finally AlN oxidizes completely. The best solution was found when applying reactively sputtered Si_xN_y. A thickness of only 100 nm prevents oxidation of a covered AlN layer for at least 24 hours at a temperature of 1000 °C in a pure oxygen atmosphere. A weak point is, however the poor adhesion between the different layers when integrating this material in a device architecture.

Surface acoustic wave devices with an AlN thickness of 2 µm on top of sapphire substrates show a phase velocity of around ~5670 m/s. The phase velocity itself has a dependency on the crystallographic structure of the substrate with respect to the wave propagation direction. This behavior can be directly linked to the difference in the Young's modulus in different directions. Basically, a higher Young's moduli results in a higher phase velocity. Simulations of SAW devices also showed that the electrode mass has an influence on the phase velocity. Electrodes consisting of heavy elements like platinum decrease the phase velocity significantly. Depending on the device dimensions, the difference can reach 1 % compared to a device with a light electrode material such as aluminum. Despite this drawback from high temperature stable metallization systems, SAW devices showed a good temperature sensitivity with a temperature coefficient of frequency TCF of about -28kHz/°C from room temperature up to 800 °C in argon atmosphere. With an additional passivation layer the TCF is reduced by 2-3kHz/°C to ~-25.5kHz/°C. For evaluating the robustness in oxygen atmosphere, the performance of the SAW devices is measured before and after the annealing step. Without passivation, devices withstand temperatures up to 600 °C. With passivation coatings, the maximum temperature can be increased by 100 °C to 700 °C independent of the passivation coating thickness. The main reason, why temperatures above 700 °C could not be reached is the poor adhesion between the different layers. At these temperature levels, delamination effects start to occur leading in the worst case to a complete failure of the SAW device.

6.2 Outlook

A technological problem, which occurred during device fabrication is the used sputter deposited for the electrode fingers in combination with a lift-off process. Basically, it is straight forward process for pattering within a MEMS device fabrication process, but with the problem that part of the material remains at the side walls, thus preventing a proper coverage by the passivation coating. To solve this problem, the implementation of a reactive ion etch step instead of the lift-off process should be considered. With a continuous metallic layer and a subsequent dry etch process, the layer can be fabricated with known stress and a better dimensional accuracy.

As a summery, AlN on top of sapphire is a promising combination for high temperature MEMS devices. The AlN layer itself is stable up to 700 °C, so that above this temperature, a passivation coating is recommended. This work showed that reactively sputtered Si_xN_y is well suited for passivation purposes. It can be deposited at temperatures below 150 °C, which is an advantage for device fabrication when using temperature sensitive sacrificial layers. These SAW devices can operate in harsh environmental up to 700 °C. But this work also showed some weak points of the device architecture. One is the poor adhesion between the different layers during high temperature loadings. Some layers delaminate from each other and therefore the electrical metallization lines get damaged or oxidized. This can cause a variation of the conduction path even at the same IDT structure, resulting in a decreased performance of the SAW device. Finally, the contact pads, which are not covered by the passivation layer, can degenerate during high temperature loading in harsh environments.

Following works on this topic should focus on increasing the adhesion between the different layers. One approach could be to use special adhesion layers or some carefully selected pre-annealing steps during the fabrication of the devices in order to increase adhesion. Furthermore, it should be considered not to open the passivation layer for electrical contact to the IDT’s, but rather use a design utilizing a capacitive coupling through the layer. After all, this work showed the high potential of AlN on sapphire for high temperature SAW sensor applications up to 700 °C even in oxygen atmosphere. Furthermore, due to the passive behavior of the device and by connecting to an antenna, a wire-less and battery less sensor can be realized.

REFERENCES

[1] RICHARDSON, M.T.: *Practical Blacksmithing: The Four Classic Volumes in One*. Book Sales, 2017. – ISBN: 9780785835394

[2] SPEICH, G.R. ; LESLIE, W.C.: Tempering of steel. In: *Metallurgical Transactions* 3 (1972), May, Nr. 5, S. 1043–1054. DOI: dx.doi.org/10.1007/BF02642436. – ISSN: 1543–1916

[3] BÖGE, G. ; BÖGE, W.: *Handbuch Maschinenbau: Grundlagen und Anwendungen der Maschinenbau-Technik*. Springer-Verlag, 2014. DOI: dx.doi.org/10.1007/978-3-658-06598-0. DOI: dx.doi.org/10.1007/978-3-658-06598-0. – ISBN: 978–3–658–06597–3

[4] HUNDESHAGEN, H.: *Der Schmied am Amboß: Ein praktisches Lehrbuch für alle Schmiede*. Vincentz Network, 2007 (4th Edition). – ISBN: 978–3878705819

[5] BEWOOR, A.K. ; KULKARNI, V.A.: *Metrology and Measurement*. McGraw-Hill, 2009. – ISBN: 9780070140004

[6] HESSE, S. ; SCHNELL, G.: *Sensoren für die Prozess- und Fabrikautomation*. Springer Verlag, 2014 (6th Edition). DOI: dx.doi.org/10.1007/978-3-658-05867-8. DOI: dx.doi.org/10.1007/978-3-658-05867-8. – ISBN: 978–3–658–05866–1

[7] PARK, R.M. ; CARROLL, R.M. ; BLISS, P. ; BURNS, G.W. ; DESMARIS, R.R. ; HALL, F.B. ; HERZKOVITZ, M.B. ; MACKENZIE, D. ; MCGUIRE, E.F. ; REED, R.P. ; SPARKS, L.L. ; WANG, T.P.: *MANUAL ON THE USE OF THERMOCOUPLES IN TEMPERATURE MEASUREMENT*. ASTM International, 1993 (Fourth Edition). DOI: dx.doi.org/10.1520/MNL12-4TH-EB. DOI: dx.doi.org/10.1520/MNL12-4TH-EB. – ISBN: 978–0–8031–1466–1

[8] Aubert, T. ; Elmazria, O. ; Assouar, M.B.: Wireless and batteryless surface acoustic wave sensors for high temperature environments. In: *Electronic Measurement Instruments, 2009. ICEMI '09. 9th International Conference on*, 2009, S. 2–890–2–898

[9] Skog, A.: Surface Acoustic Wave Wireless Temperature Sensor for OEM Integration. In: *Sensors & Transducers e-Digest* 89 (2008), Nr. 3. – ISSN: 1726–5479

[10] Padture, N.P. ; Gell, M. ; Jordan, E.H.: Thermal barrier coatings for gas-turbine engine applications. In: *Science* 296 (2002), Nr. 5566, S. 280–284. DOI: dx.doi.org/10.1126/science.1068609

[11] Fachberger, R. ; Bruckner, G. ; Hauser, R. ; Biniasch, J. ; Reindl, L. ; Ruppel, C.: Properties of radio frequency Rayleigh waves on langasite at elevated temperatures. In: *IEEE Ultrasonics Symposium, 2004* Bd. 2, 2004. – ISSN: 1051–0117, S. 1223–1226 Vol.2

[12] Cunha, M.P. da: Wireless sensing in hostile environments. In: *Ultrasonics Symposium (IUS), 2013 IEEE International* IEEE, 2013, S. 1337–1346

[13] Cunha, M.P. da ; Maskay, A. ; Lad, R.J. ; Frankel, D.J. ; Moulzolf, S. ; Call, M. ; Bernhardt, G.: Pt-Ni/Pt-Zr electrodes for stable SAW resonator operation during repeated temperature cycling up to 1000°C. In: *Ultrasonics Symposium (IUS), 2015 IEEE International* IEEE, 2015, S. 1–4

[14] Frankel, D.J. ; Bernhardt, G.P. ; Sturtevant, B.T. ; Moonlight, T. ; Da Cunha, M.P. ; Lad, R.J.: Stable electrodes and ultrathin passivation coatings for high temperature sensors in harsh environments. In: *Sensors, 2008 IEEE* IEEE, 2008, S. 82–85

[15] Krassikoff, J.I. ; Bernhardt, G.P. ; Call, M. ; Dunn, T.: Synthesis and characterization of SiAlON thin film coatings. In: *Society of Vacuum Coaters 46 th Annual Technical Conference*, 2003, S. 627–630

[16] Zhang, X. ; Byrne, M.S. ; Lad, R.J.: Structure and optical properties of Zr 1- x Si x N thin films on sapphire. In: *Thin Solid Films* 518 (2009), Nr. 5, S. 1522–1526. DOI: dx.doi.org/10.1016/j.tsf.2009.09.025

[17] HAYNES, W.M.: *Handbook of Chemistry and Physics*. CRC Press Taylor and Francis Group, 2011. – ISBN: 978–1–4398–2077–3

[18] MADOU, M.J.: *Fundamentals of Microfabrication: The Science of Minituarization*. CRC Press, 2002 (Second Edition). – ISBN: 9780849308260

[19] SCHUEGRAF, K.K.: *Handbook of thin-film deposition processes and techniques: principles, methods, equipment, and applications*. Noyes Data Corporation/Noyes Publications, 1988. – ISBN: 978–0815511533

[20] SESHAN, K.: *Handbook of thin film deposition*. William Andrew, 2012. – ISBN: 978–1437778731

[21] MOVCHAN, B.A. ; DEMCHISHIN, A.V.: Structure and Properties of Tick Ccondensates of Nickel, Titanum, Tungsten, Aluminum Oxides, and Zirconium Dioxide in Vacuum. In: *Phys. Metals Metallogr.* 28 (1969), Nr. 4

[22] THORNTON, J.A.: Influence of apparatus geometry and deposition conditions on the structure and topography of thick sputtered coatings. In: *Journal of Vacuum Science and Technology* 11 (1974), Nr. 4, S. 666–670. DOI: dx.doi.org/10.1116/1.1312732

[23] ANDERS, A: A structure zone diagram including plasma-based deposition and ion etching. In: *Thin Solid Films* 518 (2010), Nr. 15, S. 4087 – 4090. DOI: dx.doi.org/10.1016/j.tsf.2009.10.145. – ISSN: 0040–6090

[24] MESSIER, R. ; GIRI, A.P. ; ROY, R.A.: Revised structure zone model for thin film physical structure. In: *Journal of Vacuum Science and Technology A* 2 (1984), Nr. 2, S. 500–503. DOI: dx.doi.org/10.1116/1.572604

[25] FASCHING, G.: *Werkstoffe für die Elektrotechnik*. SpringerWienNewYork, 2005 (Third Edition). – ISBN: 978–3–7091–4194–6

[26] GOGOLIDES, E. ; TEGOU, E. ; BELTSIOS, K. ; PAPADOKOSTAKI, K. ; HATZAKIS, M.: Micro- and Nano-Engineering 95 Thermal and mechanical analysis of photoresist and silylated photoresist films: Application to AZ 5214™. In: *Microelectronic Engineering* 30 (1996), Nr. 1, S. 267 – 270. DOI: dx.doi.org/10.1016/0167-9317(95)00242-1. – ISSN: 0167–9317

[27] Williams, K.R. ; Gupta, K. ; Wasilik, M.: Etch rates for micromachining processing-Part II. In: *Journal of Microelectromechanical Systems* 12 (2003), Dec, Nr. 6, S. 761–778. DOI: dx.doi.org/10.1109/JMEMS.2003.820936. – ISSN: 1057–7157

[28] Seidel, H ; Csepregi, L. ; Heuberger, A. ; Baumgärtel, H.: Anisotropic Etching of Crystalline Silicon in Alkaline Solutions. In: *J.Electrochem. Soc.* 137 (1990), S. 3612 – 3626. DOI: dx.doi.org/10.1149/1.2086277

[29] Gillinger, M. ; Schneider, M. ; Bittner, A. ; Nicolay, P. ; Schmid, U.: Impact of annealing temperature on the mechanical and electrical properties of sputtered aluminum nitride thin films. In: *Journal of Applied Physics* 117 (2015), Nr. 6. DOI: dx.doi.org/10.1063/1.4907208

[30] Yu, H.-H. ; He, M.Y. ; Hutchinson, J.W.: Edge effects in thin film delamination. In: *Acta Materialia* 49 (2001), Nr. 1, S. 93 – 107. DOI: dx.doi.org/10.1016/S1359-6454(00)00293-7. – ISSN: 1359–6454

[31] Machlin, E.S.: *Materials Science in Microelectronics: The relationships between thin film processing and structure*. Cambridge Univ Press, 2006. – ISBN: 978–0–08–044640–0

[32] Lingnau, J. ; Dammel, R. ; Theis, J.: Recent trends in x-ray resists. In: *Solid State Technology* 32 (1989), Nr. 10, S. 107–112

[33] Mohr, J. ; Ehrfeld, W. ; Münchmeyer, D. ; Stutz, A.: Resist technology for deep-etch synchrotron radiation lithography. In: *Makromolekulare Chemie. Macromolecular Symposia* 24 (1989), Nr. 1, S. 231–240. DOI: dx.doi.org/10.1002/masy.19890240124. – ISSN: 1521–3900

[34] Goldstein, J. ; Newbury, D.E. ; Joy, D.C. ; Lyman, C.E. ; Echlin, P. ; Lifshin, E. ; Sawyer, L. ; Michael, J.R.: *Scanning Electron Microscopy and X-ray Microanalysis: Third Edition*. Springer US, 2013. – ISBN: 9781461349693

[35] Williams, D.B. ; Carter, C.B.: *Transmission Electron Microscopy: A Textbook for Materials Science*. Springer, 2009. – ISBN: 978–0–387–76500–6

[36] Giessibl, F.J.: Advances in atomic force microscopy. In: *Rev. Mod. Phys.* 75 (2003), Jul, S. 949–983. DOI: dx.doi.org/10.1103/RevModPhys.75.949

[37] BUTT, H.-J. ; CAPPELLA, B ; KAPPL, M.: Force measurements with the atomic force microscope: Technique, interpretation and applications. In: *Surface Science Reports* 59 (2005), Nr. 1, S. 1 – 152. DOI: dx.doi.org/10.1016/j.surfrep.2005.08.003. – ISSN: 0167–5729

[38] SPIESS, L. ; BEHNKEN, H ; GENZEL, C ; SCHWARZER, R. ; TEICHERT, G.: *Moderne Röntgenbeugung*. Vieweg+Teubner, 2009. – ISBN: 978–3–8351–0166–1

[39] HOLÝ, V. ; PIETSCH, U. ; BAUMBACH, T.: *High-resolution x-ray scattering from thin films and multilayers*. Berlin [u.a.] : Springer, 1999 (Springer tracts in modern physics ; 149). – ISBN: 3–540–62029–X

[40] HEYWANG, W. ; LUBITZ, K. ; WERSING, W.: *Piezoelectricity: evolution and future of a technology*. Bd. 114. Springer Science & Business Media, 2008. – ISBN: 978–3–642–08818–6

[41] ARNAU, A.: *Piezoelectric transducers and applications*. Bd. 2004. Springer, 2004. – ISBN: 978–3–540–77507–2

[42] VOIGT, W.: *Lehrbuch der kristallphysik (mit ausschluss der kristalloptik)*. Springer-Verlag, 2014. – ISBN: 978–3–663–15316–0

[43] IRE Standards on Piezoelectric Crystals: Determination of the Elastic, Piezoelectric, and Dielectric Constants-The Electromechanical Coupling Factor, 1958. In: *Proceedings of the IRE* 46 (1958), April, Nr. 4, S. 764–778. DOI: dx.doi.org/10.1109/JRPROC.1958.286778. – ISSN: 0096–8390

[44] STEWART, M. ; CAIN, M.G.: *Direct Piezoelectric Measurement: The Berlincourt Method*. Dordrecht : Springer Netherlands, 2014. – 37–64 S. – ISBN: 978–1–4020–9311–1

[45] BARZEGAR, A. ; DAMJANOVIC, D. ; LEDERMANN, N. ; MURALT, P.: Piezoelectric response of thin films determined by charge integration technique: Substrate bending effects. In: *Journal of Applied Physics* 93 (2003), Nr. 8, S. 4756–4760. DOI: dx.doi.org/10.1063/1.1558228

[46] Barzegar, A.F. ; Damjanovic, D. ; Setter, N.: The effect of boundary conditions and sample aspect ratio on apparent d/sub 33/ piezoelectric coefficient determined by direct quasistatic method. In: *IEEE Transactions on Ultrasonics, Ferroelectrics, and Frequency Control* 51 (2004), March, Nr. 3, S. 262–270. DOI: dx.doi.org/10.1109/TUFFC.2004.1320781. – ISSN: 0885–3010

[47] Southin, J.E.A. ; Wilson, S.A. ; Schmitt, D. ; Whatmore, R.W.: e 31, f determination for PZT films using a conventional 'd 33' meter. In: *Journal of Physics D: Applied Physics* 34 (2001), Nr. 10, S. 1456. DOI: dx.doi.org/10.1088/0022-3727/34/10/303

[48] Berlincourt, D. ; Jaffe, H. ; Shiozawa, L.R.: Electroelastic properties of the sulfides, selenides, and tellurides of zinc and cadmium. In: *Physical Review* 129 (1963), Nr. 3, S. 1009. DOI: dx.doi.org/10.1103/PhysRev.129.1009

[49] Schneider, M. ; Bittner, A. ; Schmid, U.: Improved piezoelectric constants of sputtered aluminium nitride thin films by pre-conditioning of the silicon surface. In: *Journal of Physics D: Applied Physics* 48 (2015), Nr. 40, S. 405301. DOI: dx.doi.org/10.1088/0022-3727/48/40/405301

[50] Sze, S.M. ; Kwok, K.Ng.: *Physics of Semiconductor Devices*. John Wiley and Sons, 2006 (Third Edition). – ISBN: 978–0–471–14323–9

[51] Schneider, M. ; Bittner, A. ; Strunz, T. ; Schmid, U.: Impact of Sputter Deposition Parameters on the Leakage Current Behavior of Aluminum Nitride Thin Films. In: *Adaptive, Active and Multifunctional Smart Materials Systems* Bd. 77, Trans Tech Publications, 1 2013 (Advances in Science and Technology), S. 29–34

[52] Gillinger, M. ; Schneider, M. ; Bittner, A. ; Nicolay, P. ; Schmid, U.: High temperature performance of sputter-deposited piezoelectric aluminum nitride thin films. In: *SPIE Microtechnologies* International Society for Optics and Photonics, 2015, S. 951707–951707

[53] GILLINGER, M. ; SHAPOSHNIKOV, K. ; KNOBLOCH, T. ; STÖGER-POLLACH, M. ; ARTNER, W. ; HRADIL, K. ; SCHNEIDER, M. ; KALTENBACHER, M. ; SCHMID, U.: Enhanced c-axis orientation of aluminum nitride thin films by plasma-based pre-conditioning of sapphire substrates for SAW applications. In: *Applied Surface Science* 435 (2018), S. 432 – 437. DOI: dx.doi.org/j.apsusc.2017.11.113. – ISSN: 0169–4332

[54] JACOBI, M.: Pierre Curie – ein Leben für die Forschung. Physikgeschichte. In: *Physik in unserer Zeit* 37 (2006), Nr. 3, 116–121. DOI: dx.doi.org/10.1002/piuz.200601096. – ISSN: 1521–3943

[55] TADIGADAPA, S. ; MATETI, K.: Piezoelectric MEMS sensors: state-of-the-art and perspectives. In: *Measurement Science and Technology* 20 (2009), Nr. 9, S. 092001. DOI: dx.doi.org/10.1088/0957-0233/20/9/092001

[56] CHAWLA, V ; HOLEC, D. ; MAYRHOFER, P.H.: The effect of interlayer composition and thickness on the stabilization of cubic AlN in AlN/Ti–Al–N superlattices. In: *Thin Solid Films* 565 (2014), S. 94 – 100. DOI: dx.doi.org/10.1016/j.tsf.2014.06.051. – ISSN: 0040–6090

[57] KASAP, S ; CAPPER, P: *Springer Handbook of Electronic and Photonic Materials*. Springer Science+Business Media, Inc., 2006. – ISBN: 978–0–387–26059–4

[58] AMBACHER, O.: Growth and applications of Group III-nitrides. In: *Journal of Physics D: Applied Physics* 31 (1998), Nr. 20, S. 2653. DOI: dx.doi.org/10.1088/0022-3727/31/20/001

[59] ABABNEH, A. ; SCHMID, U. ; HERNANDO, J. ; SÁNCHEZ-ROJAS, J.L. ; SEIDEL, H.: The influence of sputter deposition parameters on piezoelectric and mechanical properties of AlN thin films. In: *Materials Science and Engineering: B* 172 (2010), Nr. 3, S. 253 – 258. DOI: dx.doi.org/10.1016/j.mseb.2010.05.026. – ISSN: 0921–5107

[60] AKIYAMA, M. ; TABARU, T. ; NISHIKUBO, K. ; TESHIGAHARA, A.: Preparation of scandium aluminum nitride thin films by using scandium aluminum alloy sputtering target and design of experiments. In: *Journal of the Ceramic Society of Japan* 118 (2010), Nr. 1384, S. 1166–1169. DOI: dx.doi.org/10.2109/jcersj2.118.1166

[61] Slack, G.A. ; Tanzilli, R.A. ; Pohl, R.O. ; Vandersande, J.W.: The intrinsic thermal conductivity of AlN. In: *Journal of Physics and Chemistry of Solids* 48 (1987), Nr. 7, S. 641–647. DOI: dx.doi.org/10.1016/0022-3697(87)90153-3

[62] Handy, E.M. ; Rao, M.V. ; Jones, K.A. ; Derenge, M.A. ; Chi, P.H. ; Vispute, R.D. ; Venkatesan, T. ; Papanicolaou, N.A. ; Mittereder, J.: Effectiveness of AlN encapsulant in annealing ion-implanted SiC. In: *Journal of Applied Physics* 86 (1999), Nr. 2, S. 746–751. DOI: dx.doi.org/10.1063/1.370798

[63] Zheng, Q. ; Reddy, R.G.: Mechanism of in situ formation of AlN in Al melt using nitrogen gas. In: *Journal of materials science* 39 (2004), Nr. 1, S. 141–149. DOI: dx.doi.org/10.1023/B:JMSC.0000007738.14116.fd

[64] Yoder, M.N.: Wide bandgap semiconductor materials and devices. In: *IEEE Transactions on Electron Devices* 43 (1996), Oct, Nr. 10, S. 1633–1636. DOI: dx.doi.org/10.1109/16.536807. – ISSN: 0018–9383

[65] Schneider, M. ; Bittner, A. ; Patocka, F. ; Stöger-Pollach, M. ; Halwax, E. ; Schmid, U.: Impact of the surface-near silicon substrate properties on the microstructure of sputter-deposited AlN thin films. In: *Applied Physics Letters* 101 (2012), Nr. 22. DOI: dx.doi.org/10.1063/1.4768951

[66] Barshilia, H.C. ; Deepthi, B. ; Rajam, K.S.: Growth and characterization of aluminum nitride coatings prepared by pulsed-direct current reactive unbalanced magnetron sputtering. In: *Thin Solid Films* 516 (2008), Nr. 12, S. 4168 – 4174. DOI: dx.doi.org/10.1016/j.tsf.2007.10.129. – ISSN: 0040–6090

[67] Cicek, E. ; McClintock, R. ; Cho, C.Y. ; Rahnema, B. ; Razeghi, M.: AlxGa1-xN-based solar-blind ultraviolet photodetector based on lateral epitaxial overgrowth of AlN on Si substrate. In: *Applied Physics Letters* 103 (2013), Nr. 18, S. 181113. DOI: dx.doi.org/10.1063/1.4828497

[68] Inoue, S. ; Okamoto, K. ; Nakano, T. ; Ohta, J. ; Fujioka, H.: Epitaxial growth of AlN films on Rh ultraviolet mirrors. In: *Applied Physics Letters* 91 (2007), Nr. 13, S. 131910. DOI: dx.doi.org/10.1063/1.2793187

[69] Tabrizian, R. ; Hodjat-Shamami, M. ; Ayazi, F.: High-Frequency AlN-on-Silicon Resonant Square Gyroscopes. In: *Journal of Microelectromechanical Systems* 22 (2013), Oct, Nr. 5, S. 1007–1009. DOI: dx.doi.org/10.1109/JMEMS.2013.2273031. – ISSN: 1057–7157

[70] Williams, M.D. ; Griffin, B.A. ; Reagan, T.N. ; Underbrink, J.R. ; Sheplak, M.: An AlN MEMS Piezoelectric Microphone for Aeroacoustic Applications. In: *Journal of Microelectromechanical Systems* 21 (2012), April, Nr. 2, S. 270–283. DOI: dx.doi.org/10.1109/JMEMS.2011.2176921. – ISSN: 1057–7157

[71] Sökmen, Ü. ; Stranz, A. ; Waag, A. ; Ababneh, A. ; Seidel, H. ; Schmid, U. ; Peiner, E.: Evaluation of resonating Si cantilevers sputter-deposited with AlN piezoelectric thin films for mass sensing applications. In: *Journal of Micromechanics and Microengineering* 20 (2010), Nr. 6, S. 064007. DOI: dx.doi.org/10.1088/0960-1317/20/6/064007

[72] Kucera, M. ; Wistrela, E. ; Pfusterschmied, G. ; Ruiz-Díez, V. ; Manzaneque, T. ; Sánchez-Rojas, J.L. ; Schalko, J. ; Bittner, A. ; Schmid, U.: Characterization of a roof tile-shaped out-of-plane vibrational mode in aluminum-nitride-actuated self-sensing micro-resonators for liquid monitoring purposes. In: *Applied Physics Letters* 104 (2014), Nr. 23. DOI: dx.doi.org/10.1063/1.4882177

[73] Pfusterschmied, G. ; Kucera, M. ; Wistrela, E. ; Manzaneque, T. ; Ruiz-Díez, V. ; Sánchez-Rojas, J.L. ; Bittner, A. ; Schmid, U.: Temperature dependent performance of piezoelectric MEMS resonators for viscosity and density determination of liquids. In: *Journal of Micromechanics and Microengineering* 25 (2015), Nr. 10, S. 105014. DOI: dx.doi.org/10.1088/0960-1317/25/10/105014

[74] Hara, M. ; Kuypers, J. ; Abe, T. ; Esashi, M.: Surface micromachined AlN thin film 2 {GHz} resonator for {CMOS} integration. In: *Sensors and Actuators A: Physical* 117 (2005), Nr. 2, S. 211 – 216. DOI: dx.doi.org/10.1016/j.sna.2004.06.014. – ISSN: 0924–4247

[75] Serina, F. ; Ng, K.Y.S. ; Huang, C. ; Auner, G.W. ; Rimai, L. ; Naik, R.: Pd/AlN/SiC thin-film devices for selective hydrogen sensing. In: *Applied Physics Letters* 79 (2001), Nr. 20, S. 3350–3352. DOI: dx.doi.org/10.1063/1.1415777

[76] Aubert, T. ; Elmazria, O. ; Bardong, J. ; Bruckner, G. ; Assouar, B.: Is AlN/Sapphire bilayer structure an alternative to langasite for ultra-high-temperature SAW applications? In: *2011 IEEE International Ultrasonics Symposium*, 2011. – ISSN: 1051–0117, S. 2082–2085

[77] Aubert, T. ; Elmazria, O. ; Assouar, B. ; Bouvot, L. ; Oudich, M.: Surface acoustic wave devices based on AlN/sapphire structure for high temperature applications. In: *Applied Physics Letters* 96 (2010), Nr. 20, S. 3503. DOI: dx.doi.org/10.1063/1.3430042

[78] Dubois, M.A. ; Muralt, P.: Stress and piezoelectric properties of aluminum nitride thin films deposited onto metal electrodes by pulsed direct current reactive sputtering. In: *Journal of Applied Physics* 89 (2001), Nr. 11, S. 6389–6395. DOI: dx.doi.org/10.1063/1.1359162

[79] Bittner, A. ; Ababneh, A. ; Seidel, H. ; Schmid, U.: Influence of the crystal orientation on the electrical properties of AlN thin films on LTCC substrates. In: *Applied Surface Science* 257 (2010), Nr. 3, S. 1088–1091. DOI: dx.doi.org/10.1016/j.apsusc.2010.08.019

[80] Ziegler, J.F. ; Ziegler, M.D. ; Biersack, J.P.: SRIM–The stopping and range of ions in matter. In: *Nuclear Instruments and Methods in Physics Research Section B: Beam Interactions with Materials and Atoms* 268 (2010), Nr. 11, S. 1818–1823. DOI: dx.doi.org/10.1016/j.nimb.2010.02.091

[81] Pelleg, J. ; Zevin, L.Z. ; Lungo, S. ; Croitoru, N.: Reactive-sputter-deposited TiN films on glass substrates. In: *Thin Solid Films* 197 (1991), Nr. 1, S. 117–128. DOI: dx.doi.org/10.1016/0040-6090(91)90225-M

[82] Sheldon, B.W. ; Rajamani, A. ; Bhandari, A. ; Chason, E. ; Hong, S.K. ; Beresford, R.: Competition between tensile and compressive stress mechanisms during Volmer-Weber growth of aluminum nitride films. In: *Journal of Applied Physics* 98 (2005), Nr. 4. DOI: dx.doi.org/10.1063/1.1994944

[83] Bhandari, A. ; Sheldon, B.W. ; Hearne, S.J.: Competition between tensile and compressive stress creation during constrained thin film island coalescence. In: *Journal of Applied Physics* 101 (2007), Nr. 3. DOI: dx.doi.org/10.1063/1.2432376

[84] Floro, J.A. ; Hearne, S.J. ; Hunter, J.A. ; Kotula, P. ; Chason, E. ; Seel, S.C. ; Thompson, C.V.: The dynamic competition between stress generation and relaxation mechanisms during coalescence of Volmer–Weber thin films. In: *Journal of Applied Physics* 89 (2001), Nr. 9, S. 4886–4897. DOI: dx.doi.org/10.1063/1.1352563

[85] Fischeneder, M. ; Wistrela, E. ; Bittner, A. ; Schneider, M. ; Schmid, U.: Tailored wafer holder for a reliable deposition of sputtered aluminium nitride thin films at low temperatures. In: *Materials Science in Semiconductor Processing* 71 (2017), S. 283–289. DOI: dx.doi.org/10.1016/j.mssp.2017.08.010

[86] Lin, C.Y ; Lu, F.H: Oxidation behavior of AlN films at high temperature under controlled atmosphere. In: *Journal of the European Ceramic Society* 28 (2008), Nr. 3, S. 691 – 698. DOI: dx.doi.org/10.1016/j.jeurceramsoc.2007.07.015. – ISSN: 0955–2219

[87] Lee, J.W. ; Radu, I. ; Alexe, M.: Oxidation behavior of AlN substrate at low temperature. In: *Journal of Materials Science: Materials in Electronics* 13 (2002), Mar, Nr. 3, S. 131–137. DOI: dx.doi.org/10.1023/A:1014377132233. – ISSN: 1573–482X

[88] Grosser, M. ; Münch, M. ; Seidel, H. ; Bienert, C. ; Roosen, A. ; Schmid, U.: The impact of substrate properties and thermal annealing on tantalum nitride thin films. In: *Applied Surface Science* 258 (2012), Nr. 7, S. 2894–2900. DOI: dx.doi.org/10.1016/j.apsusc.2011.11.003

[89] Ababneh, A.: *Herstellung und Charakterisierung von dünnen, piezoelektrischen Aluminiumnitrid-Schichten für MEMS-Anwendungen*, Universität des Saarlandes, Phd.Thesis, 2009

[90] Kolodzey, J. ; Chowdhury, E.A. ; Qui, G. ; Olowolafe, J. ; Swann, C.P. ; Unruh, K.M. ; Suehle, J. ; Wilson, R.G. ; Zavada, J.M.: The effects of oxidation temperature on the capacitance–voltage characteristics of oxidized AlN films on Si. In: *Applied physics letters* 71 (1997), Nr. 26, S. 3802–3804. DOI: dx.doi.org/10.1063/1.120510

[91] Chowdhury, E.A. ; Kolodzey, J. ; Olowolafe, J.O. ; Qiu, G. ; Katulka, G. ; Hits, D. ; Dashiell, M. ; Weide, D. Van d. ; Swann, C.P. ; Unruh, K.M.: Thermally oxidized AlN thin films for device insulators. In: *Applied physics letters* 70 (1997), Nr. 20, S. 2732–2734. DOI: dx.doi.org/10.1063/1.118980

[92] Martin, F. ; Muralt, P. ; Dubois, M.A. ; Pezous, A.: Thickness dependence of the properties of highly c-axis textured AlN thin films. In: *Journal of Vacuum Science & Technology A: Vacuum, Surfaces, and Films* 22 (2004), Nr. 2, S. 361–365. DOI: dx.doi.org/10.1116/1.1649343

[93] Zheng, L. ; Ramalingam, S. ; Shi, T. ; Peterson, R.L.: Aluminum nitride thin film sensor for force, acceleration, and acoustic emission sensing. In: *Journal of Vacuum Science and Technology A* 11 (1993), Nr. 5, S. 2437–2446. DOI: dx.doi.org/10.1116/1.578589

[94] Doll, J.C. ; Petzold, B.C. ; Ninan, B. ; Mullapudi, R. ; Pruitt, B.L.: Aluminum nitride on titanium for CMOS compatible piezoelectric transducers. In: *Journal of Micromechanics and Microengineering* 20 (2010), Nr. 2, S. 025008. DOI: dx.doi.org/10.1088/0960-1317/20/2/025008

[95] Ben Hassine, N. ; Mercier, D. ; Renaux, P. ; Parat, G. ; Basrour, S. ; Waltz, P. ; Chappaz, C. ; Ancey, P. ; Blonkowski, S.: Dielectrical properties of metal-insulator-metal aluminum nitride structures: Measurement and modeling. In: *Journal of Applied Physics* 105 (2009), Nr. 4. DOI: dx.doi.org/10.1063/1.3081977

[96] Engelmark, F. ; Westlinder, J. ; Iriarte, G.F. ; Katardjiev, I.V. ; Olsson, J.: Electrical characterization of AlN MIS and MIM structures. In: *IEEE Transactions on Electron Devices* 50 (2003), May, Nr. 5, S. 1214–1219. DOI: dx.doi.org/10.1109/TED.2003.813231. – ISSN: 0018–9383

[97] Ouisse, T. ; Schenk, H.P.D. ; Karmann, S. ; Kaiser, U.: Electrical characterization of the AlN/Si (111) system. In: *Materials Science Forum* Bd. 264 Trans Tech Publ, 1998, S. 1389–1392

[98] Groner, M.D. ; Elam, J.W. ; Fabreguette, F.H. ; George, S.M.: Electrical characterization of thin Al2O3 films grown by atomic layer deposition on silicon and various metal substrates. In: *Thin Solid Films* 413 (2002), Nr. 1, S. 186–197. DOI: dx.doi.org/10.1016/S0040-6090(02)00438-8

[99] Lin, H.C. ; Ye, P.D. ; Wilk, G.D.: Leakage current and breakdown electric-field studies on ultrathin atomic-layer-deposited Al2O3 on GaAs. In: *Applied physics letters* 87 (2005), Nr. 18, S. 182904. DOI: dx.doi.org/10.1063/1.2120904

[100] Lee, K.N. ; Worrell, W.L.: The Oxidation of iridium-aluminum and iridium-hafnium intermetallics at temperatures above 1550°C. In: *Oxidation of Metals* 32 (1989), Nr. 5, S. 357–369. DOI: dx.doi.org/10.1007/BF00665443. – ISSN: 1573–4889

[101] Tay, K.W. ; Huang, C.L. ; Wu, L.: Influence of piezoelectric film and electrode materials on film bulk acoustic-wave resonator characteristics. In: *Japanese journal of applied physics* 43 (2004), Nr. 3R, S. 1122. DOI: dx.doi.org/10.1143/JJAP.43.1122

[102] Bartlett, R.W.: Platinum oxidation kinetics with convective diffusion and surface reaction. In: *Journal of The Electrochemical Society* 114 (1967), Nr. 6, S. 547–550

[103] Fryburg, G.C.: Enhanced Oxidation of Platinum in Activated Oxygen. In: *The Journal of Chemical Physics* 24 (1956), Nr. 2, S. 175–180. DOI: dx.doi.org/10.1063/1.1742453

[104] Fryburg, G.C. ; Petrus, H.M.: Kinetics of the Oxidation of Platinum. In: *Journal of the Electrochemical Society* 108 (1961), Nr. 6, S. 496–503

[105] Griffith, W.P.: *The chemistry of the rarer platinum metals (Os, Ru, Ir, and Rh)*. Interscience Publishers, 1967 (Interscience monographs on chemistry: Inorganic chemistry section)

[106] Chalamala, B.R. ; Wei, Y. ; Reuss, R.H. ; Aggarwal, S. ; Gnade, B.E. ; Ramesh, R. ; Bernhard, J.M. ; Sosa, E.D. ; Golden, D.E.: Effect of growth conditions on surface morphology and photoelectric work function characteristics of iridium oxide thin films. In: *Applied physics letters* 74 (1999), Nr. 10, S. 1394–1396. DOI: dx.doi.org/10.1063/1.123561

[107] Jeurgens, L.P.H. ; Sloof, W.G. ; Tichelaar, F.D. ; Mittemeijer, E.J.: Growth kinetics and mechanisms of aluminum-oxide films formed by thermal oxidation of aluminum. In: *Journal of applied physics* 92 (2002), Nr. 3, S. 1649–1656. DOI: dx.doi.org/10.1063/1.1491591

[108] LEE, J.S. ; PARK, H.D. ; SHIN, S.M. ; PARK, J.W.: Agglomeration phenomena of high temperature coefficient of resistance platinum films deposited by electron beam evaporation. In: *Journal of Materials Science Letters* 16 (1997), Nr. 15, S. 1257–1259. DOI: dx.doi.org/10.1023/A:1018562505640. – ISSN: 1573–4811

[109] FIREBAUGH, S.L. ; JENSEN, K.F. ; SCHMIDT, M.A.: Investigation of high-temperature degradation of platinum thin films with an in situ resistance measurement apparatus. In: *Journal of Microelectromechanical systems* 7 (1998), Nr. 1, S. 128–135. DOI: dx.doi.org/10.1109/84.661395

[110] WRBANEK, J.D. ; LASTER, K.L.H.: *Preparation and analysis of platinum thin films for high temperature sensor applications*. Bibliogov, 2005. – ISBN: 978–1289262853

[111] SCHMID, U. ; SEIDEL, H.: Effect of high temperature annealing on the electrical performance of titanium/platinum thin films. In: *Thin Solid Films* 516 (2008), Nr. 6, S. 898–906. DOI: dx.doi.org/10.1016/j.tsf.2007.04.128

[112] TISONE, T.C. ; DROBEK, J.: Diffusion in Thin Film Ti–Au, Ti–Pd, and Ti–Pt Couples. In: *Journal of Vacuum Science and Technology* 9 (1972), Nr. 1, S. 271–275. DOI: dx.doi.org/10.1116/1.1316577

[113] MOULZOLF, S.C. ; FRANKEL, D.J. ; BERNHARDT, G.P. ; NUGENT, B. ; LAD, R.J.: Thin film electrodes and passivation coatings for harsh environment microwave acoustic sensors. In: *SPIE Microtechnologies* International Society for Optics and Photonics, 2011, S. 806606–806606

[114] THOMPSON, C.V.: Solid-state dewetting of thin films. In: *Annual Review of Materials Research* 42 (2012), S. 399–434. DOI: dx.doi.org/10.1146/annurev-matsci-070511-155048

[115] ZHU, S. ; WANG, F. ; LOU, H. ; WU, W.: Reactive sputter deposition of alumina films on superalloys and their high-temperature corrosion resistance. In: *Surface and Coatings Technology* 71 (1995), Nr. 1, S. 9–15. DOI: dx.doi.org/10.1016/0257-8972(94)02289-3

[116] APPELS, J.A. ; KOOI, E. ; PAFFEN, M.M. ; SCHATORJE, J.J.H. ; VERKUYLEN, W.H.C.G.: Local oxidation of silicon and its application in semiconductor-device technology. In: *PHILIPS RESEARCH REPORTS.* 25 (1970), Nr. 2, S. 118–132

[117] CHUNG, C.W. ; KIM, H.I. ; SONG, Y.S.: High-Density Plasma Etching of Iridium Thin Films in a Cl2/O 2/Ar Plasma. In: *Journal of The Electrochemical Society* 150 (2003), Nr. 5, S. G297–G299. DOI: dx.doi.org/10.1149/1.1562935

[118] MAYADAS, A.F. ; SHATZKES, M.: Electrical-resistivity model for polycrystalline films: the case of arbitrary reflection at external surfaces. In: *Physical review B* 1 (1970), Nr. 4, S. 1382. DOI: dx.doi.org/10.1103/PhysRevB.1.1382

[119] MULLINS, W.W.: Theory of thermal grooving. In: *Journal of Applied Physics* 28 (1957), Nr. 3, S. 333–339. DOI: dx.doi.org/10.1063/1.1722742

[120] PARK, K.H. ; KIM, C.Y. ; JEONG, Y.W. ; KWON, H.J. ; KIM, K.Y. ; LEE, J.S. ; KIM, S.T.: Microstructures and interdiffusions of Pt/Ti electrodes with respect to annealing in the oxygen ambient. In: *Journal of materials research* 10 (1995), Nr. 7, S. 1790–1794. DOI: dx.doi.org/10.1557/JMR.1995.1790

[121] OLOWOLAFE, J.O. ; JONES JR, R.E. ; CAMPBELL, A.C. ; HEGDE, R.I. ; MOGAB, C.J. ; GREGORY, R.B.: Effects of anneal ambients and Pt thickness on Pt/Ti and Pt/Ti/TiN interfacial reactions. In: *Journal of applied physics* 73 (1993), Nr. 4, S. 1764–1772. DOI: dx.doi.org/10.1063/1.353212

[122] SINGHAL, S.C.: Thermodynamic analysis of the high-temperature stability of silicon nitride and silicon carbide. In: *Ceramurgia International* 2 (1976), Nr. 3, S. 123 – 130. DOI: dx.doi.org/10.1016/0390-5519(76)90022-3. – ISSN: 0390–5519

[123] GUSE, W. ; SAALFELD, H.: X-ray characterization and structure refinement of a new cubic alumina phase (σ-Al2O3) with spinel-type structure. In: *Neues Jahrbuch für Mineralogie Monatshefte* (1990), Nr. 5, S. 217–226

[124] GILLINGER, M. ; SHAPOSHNIKOV, K. ; KNOBLOCH, T. ; SCHNEIDER, M. ; KALTENBACHER, M. ; SCHMID, U.: Impact of layer and substrate properties on the surface acoustic wave velocity in scandium doped aluminum nitride based SAW devices on sapphire. In: *Applied Physics Letters* 108 (2016), Nr. 23. DOI: dx.doi.org/10.1063/1.4953259

[125] GILLINGER, M. ; KNOBLOCH, T. ; SCHNEIDER, M. ; SCHMID, U.: Harsh Environmental Surface Acoustic Wave Temperature Sensor Based on Pure and Scandium doped Aluminum Nitride on Sapphire. In: *Multidisciplinary Digital Publishing Institute Proceedings* Bd. 1, 2017, S. 341

[126] DONG, L. ; SHAN, J.: A comprehensive review of earthquake-induced building damage detection with remote sensing techniques. In: *{ISPRS} Journal of Photogrammetry and Remote Sensing* 84 (2013), S. 85 – 99. DOI: dx.doi.org/10.1016/j.isprsjprs.2013.06.011. – ISSN: 0924–2716

[127] SHARMA, S. ; JUDD, W.R.: Underground opening damage from earthquakes. In: *Engineering Geology* 30 (1991), Nr. 3, S. 263 – 276. DOI: dx.doi.org/10.1016/0013-7952(91)90063-Q. – ISSN: 0013–7952

[128] RAYLEIGH: On waves propagated along the plane surface of an elastic solid. In: *Proc. Lond. Math. Soc.* 17 (1885), S. 4–11. DOI: dx.doi.org/10.1112/plms/s1-17.1.4

[129] LOVE, A.E.H.: *Some problems of geodynamics*. Cambridge University Press, 2015. – ISBN: 978–1332316601

[130] SEZAWA, K.: Dispersion of elastic waves propagated on the surface of stratified bodies and on curved surfaces. (1927)

[131] WHITE, R.M. ; VOLTMER, F.W.: Direct piezoelectric coupling to surface elastic waves. In: *Applied physics letters* 7 (1965), Nr. 12, S. 314–316. DOI: dx.doi.org/10.1063/1.1754276

[132] WILLIAMSON, R.C.: Case Studies of Successful Surface-Acoustic-Wave Devices. In: *Ultrasonics Symposium, 1977*, 1977, S. 460–468

[133] BERNHARDT, G. ; SILVESTRE, C. ; LECURSI, N. ; MOULZOLF, S.C. ; FRANKEL, D.J. ; LAD, R.J.: Performance of Zr and Ti adhesion layers for bonding of platinum metallization to sapphire substrates. In: *Sensors and Actuators B: Chemical* 77 (2001), Nr. 1, S. 368–374. DOI: dx.doi.org/10.1016/S0925-4005(01)00756-0

[134] FACHBERGER, R. ; BRUCKNER, G. ; KNOLL, G. ; HAUSER, R. ; BINIASCH, J. ; REINDL, L.: Applicability of LiNbO/sub 3/, langasite and GaPO/sub 4/in high temperature SAW sensors operating at radio frequencies. In: *ieee transactions on ultrasonics, ferroelectrics, and frequency control* 51 (2004), Nr. 11, S. 1427–1431. DOI: dx.doi.org/10.1109/TUFFC.2004.1367482

[135] YAKOVKIN, R.M. I.B. a. I.B. andTaziev ; KOZLOV, A.S.: Numerical and experimental investigation SAW in langasite. In: *Ultrasonics Symposium, 1995. Proceedings., 1995 IEEE* Bd. 1, 1995. – ISSN: 1051–0117, S. 389–392 vol.1

[136] M.P., Da C. ; De Azevedo Fagundes, S.: Investigation on recent quartz-like materials for SAW applications. In: *IEEE Transactions on Ultrasonics, Ferroelectrics, and Frequency Control* 46 (1999), Nov, Nr. 6, S. 1583–1590. DOI: dx.doi.org/10.1109/58.808884. – ISSN: 0885–3010

[137] Hagon, P.J. ; Dyal, L. ; Lakin, K.M.: Wide Band UHF Compression Filters Using Aluminum Nitride on Sapphire. In: *1972 Ultrasonics Symposium*, 1972, S. 274–275

[138] Tomabechi, S. ; Kameda, S. ; Masu, K. ; Tsubouchi, K.: 2.4 GHz front-end multi-track AlN/ alpha;-Al2O3 SAW matched filter. In: *Ultrasonics Symposium, 1998. Proceedings., 1998 IEEE* Bd. 1, 1998. – ISSN: 1051–0117, S. 73–76 vol.1

[139] Tsubouchi, K. ; Mikoshiba, N.: Zero-Temperature-Coefficient SAW Devices on AlN Epitaxial Films. In: *IEEE Transactions on Sonics and Ultrasonics* 32 (1985), Sept, Nr. 5, S. 634–644. DOI: dx.doi.org/10.1109/T-SU.1985.31647. – ISSN: 0018–9537

[140] Campbell, J.J. ; Jones, W.R.: A method for estimating optimal crystal cuts and propagation directions for excitation of piezoelectric surface waves. In: *IEEE Transactions on Sonics and Ultrasonics* 15 (1968), Nr. 4, S. 209–217. DOI: dx.doi.org/10.1109/T-SU.1968.29477

[141] Kobayashi, Y. ; Tanaka, N. ; Okano, H. ; Takeuchi, K. ; Usuki, T. ; Shibata, K.: Characteristics of surface acoustic wave on AlN thin films. In: *Japanese journal of applied physics* 34 (1995), Nr. 5S, S. 2668. DOI: dx.doi.org/10.1143/JJAP.34.2668

[142] Schropp, I.: *Modellierung akustischer Oberflächenwellenleiter*, Lehrstuhl für Hochfrequenztechnik: Technische Universitaet München, Master Thesis, 1988

[143] Aubert, T. ; Elmazria, O. ; Assouar, B. ; Blampain, E. ; Hamdan, A. ; Genève, D. ; Weber, S.: Investigations on AlN/sapphire piezoelectric bilayer structure for high-temperature SAW applications. In: *IEEE transactions on ultrasonics, ferroelectrics, and frequency control* 59 (2012), Nr. 5, S. 999–1005. DOI: dx.doi.org/10.1109/TUFFC.2012.2285

[144] Elmazria, O. ; Mortet, V. ; El Hakiki, M. ; Nesladek, M. ; Alnot, P.: High velocity SAW using aluminum nitride film on unpolished nucleation side of free-standing CVD diamond. In: *IEEE Transactions on Ultrasonics, Ferroelectrics, and Frequency Control* 50 (2003), June, Nr. 6, S. 710–715. DOI: dx.doi.org/10.1109/TUFFC.2003.1209558. – ISSN: 0885–3010

[145] Hesler, J.L. ; Duan, Y. ; Foley, B. ; Crowe, T.W.: THz vector network analyzer measurements and calibration. In: *21st International Symposium on Space Terahertz Technology, Oxford, UK*, 2010. – ISBN: 9781617823626, S. 318–320

[146] Butz, T.: *Fouriertransformation für Fußgänger*. Springer, 2009. – ISBN: 978–3834809469

[147] Hewitt, E. ; Hewitt, R.E.: The Gibbs-Wilbraham phenomenon: An episode in fourier analysis. In: *Archive for History of Exact Sciences* 21 (1979), Nr. 2, S. 129–160. DOI: dx.doi.org/10.1007/BF00330404. – ISSN: 1432–0657

[148] Harris, F.J.: On the use of windows for harmonic analysis with the discrete Fourier transform. In: *Proceedings of the IEEE* 66 (1978), Nr. 1, S. 51–83. DOI: dx.doi.org/10.1109/PROC.1978.10837

[149] Bardong, J. ; Bruckner, G. ; Franz, G. ; Fachberger, R. ; Erlacher, A.: Characterisation setup of SAW devices at high temperatures and ultra high frequencies. In: *2009 IEEE International Frequency Control Symposium Joint with the 22nd European Frequency and Time forum*, 2009. – ISSN: 2327–1914, S. 28–32

[150] Visser, J.H. ; Venema, A.: Silicon SAW devices and electromagnetic feedthrough. In: *IEEE 1988 Ultrasonics Symposium Proceedings.*, 1988, S. 297–301 vol.1

[151] Morgan, D.P.: *Surface acoustic wave filters: With applications to electronic communications and signal processing*. Academic Press, 2010. – ISBN: 978–0–12–372537–0

[152] Wright, A.F.: Elastic properties of zinc-blende and wurtzite AlN, GaN, and InN. In: *Journal of Applied Physics* 82 (1997), Nr. 6, S. 2833–2839. DOI: dx.doi.org/10.1063/1.366114

[153] SCHNEIDER, M. ; BITTNER, A. ; SCHMID, U.: Thickness dependence of Young's modulus and residual stress of sputtered aluminum nitride thin films. In: *Applied Physics Letters* 105 (2014), Nr. 20, S. 201912. DOI: dx.doi.org/10.1063/1.4902448

[154] HOPCROFT, M.A. ; NIX, W.D. ; KENNY, T.W.: What is the Young's Modulus of Silicon? In: *Journal of Microelectromechanical Systems* 19 (2010), April, Nr. 2, S. 229–238. DOI: dx.doi.org/10.1109/JMEMS.2009.2039697. – ISSN: 1057–7157

[155] AKIYAMA, M. ; KAMOHARA, T. ; KANO, K. ; TESHIGAHARA, A. ; TAKEUCHI, Y. ; KAWAHARA, N.: Enhancement of piezoelectric response in scandium aluminum nitride alloy thin films prepared by dual reactive cosputtering. In: *Advanced Materials* 21 (2009), Nr. 5, S. 593–596. DOI: dx.doi.org/10.1002/adma.200802611

[156] MAYRHOFER, P.M. ; EUCHNER, H. ; BITTNER, A. ; SCHMID, U.: Circular test structure for the determination of piezoelectric constants of Sc x Al 1- x N thin films applying Laser Doppler Vibrometry and FEM simulations. In: *Sensors and Actuators A: Physical* 222 (2015), S. 301–308. DOI: dx.doi.org/10.1016/j.sna.2014.10.024

[157] GOTO, T. ; ANDERSON, O.L. ; OHNO, I. ; YAMAMOTO, S.: Elastic constants of corundum up to 1825 K. In: *Journal of Geophysical Research: Solid Earth* 94 (1989), Nr. B6, S. 7588–7602. DOI: dx.doi.org/10.1029/JB094iB06p07588

[158] LEGRANI, O. ; AUBERT, T. ; ELMAZRIA, O. ; BARTASYTE, A. ; NICOLAY, P. ; TALBI, A. ; BOULET, P. ; GHANBAJA, J. ; MANGIN, D.: AlN/IDT/AlN/Sapphire SAW Heterostructure for High-Temperature Applications. In: *IEEE Transactions on Ultrasonics, Ferroelectrics, and Frequency Control* 63 (2016), June, Nr. 6, S. 898–906. DOI: dx.doi.org/10.1109/TUFFC.2016.2547188. – ISSN: 0885–3010

[159] HOHENBERG, P. ; KOHN, W.: Inhomogeneous electron gas. In: *Physical review* 136 (1964), Nr. 3B, S. B864. DOI: dx.doi.org/10.1103/PhysRev.136.B864

[160] KOHN, W. ; SHAM, L.J.: Self-consistent equations including exchange and correlation effects. In: *Physical review* 140 (1965), Nr. 4A, S. A1133. DOI: dx.doi.org/10.1103/PhysRev.140.A1133

[161] HAMMOND, Christopher ; HAMMOND, Christopher: *Basics of crystallography and diffraction*. Bd. 214. Oxford, 2001

[162] WANG, Y. ; PERDEW, J.P.: Spin scaling of the electron-gas correlation energy in the high-density limit. In: *Physical Review B* 43 (1991), Nr. 11, S. 8911. DOI: dx.doi.org/10.1103/PhysRevB.43.8911

[163] BLÖCHL, P.E.: Projector augmented-wave method. In: *Physical Review B* 50 (1994), Nr. 24, S. 17953. DOI: dx.doi.org/10.1103/PhysRevB.50.17953

[164] YU, R. ; ZHU, J. ; YE, H.Q.: Calculations of single-crystal elastic constants made simple. In: *Computer physics communications* 181 (2010), Nr. 3, S. 671–675. DOI: dx.doi.org/10.1016/j.cpc.2009.11.017

[165] TASNÁDI, F. ; ODÉN, M. ; ABRIKOSOV, I.A.: Ab initio elastic tensor of cubic Ti 0.5 Al 0.5 N alloys: dependence of elastic constants on size and shape of the supercell model and their convergence. In: *Physical Review B* 85 (2012), Nr. 14, S. 144112. DOI: dx.doi.org/10.1103/PhysRevB.85.144112

[166] NEWNHAM, R.E.: *Properties of materials: anisotropy, symmetry, structure*. Oxford University Press on Demand, 2005. – ISBN: 0–19–852075–1

[167] NEUMANN, F.E.: *Vorlesung über die Theorie der Elastizität der festen Körper und des Lichtäthers*. O. E. Meyer. Leipzig(Hrsg.), B. G. Teubner-Verlag, 1885

[168] TANCRELL, R.H. ; HOLLAND, M.G.: Acoustic surface wave filters. In: *Proceedings of the IEEE* 59 (1971), Nr. 3, S. 393–409. DOI: dx.doi.org/10.1109/ULTSYM.1970.196004

[169] MORGAN, D.P.: A history of surface acoustic wave devices. In: *International journal of high speed electronics and systems* 10 (2000), Nr. 03, S. 553–602. DOI: dx.doi.org/10.1142/S0129156400000593

[170] SMITH, W.R. ; GERARD, H.M. ; COLLINS, J.H. ; REEDER, T.M. ; SHAW, H.J.: Analysis of interdigital surface wave transducers by use of an equivalent circuit model. In: *IEEE transactions on microwave theory and techniques* 17 (1969), Nr. 11, S. 856–864. DOI: dx.doi.org/10.1109/TMTT.1969.1127075

[171] SUZUKI, Y. ; SHIMIZU, H. ; TAKEUCHI, M. ; NAKAMURA, K. ; YAMADA, A.: Some studies on SAW resonators and multiple-mode filters. In: *1976 Ultrasonics Symposium* IEEE, 1976, S. 297–302

[172] Tobolka, G.: Mixed matrix representation of SAW transducers. In: *IEEE Transactions on Sonics and Ultrasonics* 26 (1979), Nr. 6, S. 426–427. DOI: dx.doi.org/10.1109/T-SU.1979.31128

[173] Milsom, R.F. ; Reilly, N.H.C. ; Redwood, M.: Analysis of generation and detection of surface and bulk acoustic waves by interdigital transducers. In: *IEEE Transactions on Sonics Ultrasonics* 24 (1977), S. 147–166. DOI: dx.doi.org/10.1109/T-SU.1977.30925

[174] Hashimoto, K. ; Yamaguchi, M.: Analysis of Excitation and Propagation of Acoustic Waves Under Periodic Metallic-Grating Structures for SAW Device Modeling. In: *ULTRASONICS SYMPOSIUM* Bd. 1 INSTITUTE OF ELECTRICAL & ELECTRONICS ENGINEERS INC, 1993, S. 143–143

[175] Chen, Z.H. ; Takeuchi, M. ; Yamanouchi, K.: Analysis of the film thickness dependence of a single-phase unidirectional transducer using the coupling-of-modes theory and the finite-element method. In: *IEEE transactions on ultrasonics, ferroelectrics, and frequency control* 39 (1992), Nr. 1, S. 82–94. DOI: dx.doi.org/10.1109/58.166814

[176] Endoh, G. ; Hashimoto, K. ; Yamaguchi, M.: Surface acoustic wave propagation characterisation by finite-element method and spectral domain analysis. In: *Japanese journal of applied physics* 34 (1995), Nr. 5S, S. 2638. DOI: dx.doi.org/10.1143/JJAP.34.2638

[177] Shaposhnikov, K.: *Finite-Elemente-Simulation piezoelektrischer akustischer Oberflächenwellen-Sensoren*, TU Wien, Phd. Thesis, 2015

LIST OF FIGURES

LIST OF TABLES

Formulas und Abbreviations

Physical Symbols

Symbols	Unit / Value	Meaning
α	K^{-1}	Expansion Coefficient
α_{Tukey}		Tukey Window Parameter
ϵ		Dielectric Constant
λ	m	Wavelength
λ_h	W/mK	Thermal Conductivity at 27°C
γ		Volume specific Expansion Coefficient
σ	$5.6704 * 10^{-10} m^{-2} K^{-4}$	Stefan-Boltzmann Constant
$\sigma_{avg.}$	Pa	Average Intrinsic Stress
A^*		Richardson Constant
c_p	J/gK	Heat Capacity
d_{31}, d_{33}	pm/V	Piezoelectric Constant
E	m/V	Electrical Field
f_0	Hz	Resonance Frequency
h_{AlN}	nm	Thickness of Reactive Sputtered AlN
J	A/m^2	Current Density
kh		Normalized Thickness
k_B	$8.6173 * 10^{-5} eV/K$	Boltzmann Constant
R_a	nm	Average Surface Roughness
R_s	Ω	Sheet Resistance
R_t	Ω	Resistance at Specific Temperature
p	µbar	Pressure
T	K	Temperature
T_A	°C	Annealing Temperature
T_0	K	Original Temperature

T_h	K	Homologous Temperature
T_MP	K	Melting Temperature
V	m^3	Temperature Expanded Volume
V_0	m^3	Original Volume
v_p	m/s	Phase Velocity
v_g	m/s	Group Velocity
Y	Pa	Young's Modulus

Chemical Formula

Formula	**Meaning**
Al^{3+}	Aluminium-Ion
AlN	Aluminium Nitride
Al_2O_3	Aluminiumoxid, Corundum
Al_xO_y	Aluminiumoxid
Ar^+	Argon-Ion
DQ	Diazoquinone ester
$HMDS$	Hexametyhldiszilane
Ir	Iridium
$PMMA$	Polymethylmethacrylate
Pt	Platinum
Si	Silicon
Si_xN_y	Silicon Nitride
Ta	Tantalum
Ti	Titanium

Index of Abbreviations

Abbreviations	**Meaning**
AFM	**A**tomic **F**orce **M**icroscopy
CAD	**C**omputer **A**ided **D**esign
CMOS	**C**omplementary **M**etal **Oxide** **S**emiconductor
CVD	**C**hemical **V**apor **D**eposition
EDX	**E**nergy **D**ispersive **X**-ray spectroscopy
FEM	**F**inite **E**lement **M**ethod
FWHM	**F**ull **W**idth at **H**alf **M**aximum
IDT	**I**nter**D**igital **T**ransducer
ISE	**I**nverse **S**putter **E**tch
MEMS	**M**icro **E**lectro-**M**echanical **S**ystems
NVA	**N**etwork **V**ector **A**nalyzer
PVD	**P**hysical **V**apor **D**eposition
PZT	Lead **Z**irconate **T**itanate
RIE	**R**eactive **I**on **E**tching
SAW	**S**urface **A**coustic **W**ave
SEM	**S**canning **E**lectron **M**icroscopy
SZM	**S**tructure **Z**one **M**odel
TCD	**T**emperature **C**oefficient of **D**elay
TCF	**T**emperature **C**oefficient of **F**requency
TEM	**T**ransmission **E**lectron **M**icroscopy
UV	**U**ltra **V**iolate

A Appendix

A.1 Ab initio - DFT calculation

For the realization of new materials, the knowledge of the material properties like piezo-electricity or stiffness are very important. Pre-investigations with theoretical modeling of the material structure can reduce and simplify the experimental effort substantially. For the doping of AlN, the theoretical lattice parameters (a, c) can be verified with XRD measurements. Additionally, the piezoelectric and the elastic constants can be calculated and therefore the number of the experiments can be minimized. The quantum mechanical description of such system can be calculated using the wave function $\Psi(\vec{r}, \vec{\sigma}, \vec{R}, t)$, which is a position function in the atomic lattice with the dependency of M nucleons R_l, n electrons r_i, the electron spin σ_i and the time t. Furthermore, the Schrödinger equation has to be solved. The equations are written in non-relativity form [159]:

$$i\hbar\frac{\partial\Psi}{\partial t} = \hat{H}\Psi \tag{A.1}$$

$$\begin{aligned} \hat{H} = -\frac{1}{2}\sum_{i=1}^{n}\frac{1}{m_i}\nabla_i{}^2 - \frac{1}{2}\sum_{l=1}^{N}\frac{1}{M_l}\nabla_l{}^2 - \sum_{i,l}\frac{e^2 Z_l}{|r_i - R_l|} \\ + \frac{1}{2}\sum_{i\neq j}^{n}\frac{e^2}{|r_i - r_j|} + \frac{1}{2}\sum_{k\neq l}^{N}\frac{e^2 R_k Z_l}{|R_k - R_l|} \end{aligned} \tag{A.2}$$

The Hamilton operator H describes the energy state of the system. From left to right, the terms correspond to the kinetic energy of the electrons as well as the nucleus, the Coulomb energy of the nucleus as well as the electron-electron and nucleus-nucleus interaction. If the system is time-independent, the stationary Schrödinger equation ($\hat{H}\Theta(\vec{r}, \vec{\sigma}, \vec{R}) = E\Theta$) can be used.

Another approach to calculate the material properties uses the density function theory (DFT), which was introduced by Kohn in the year 1965. He used the electron density

$n(r)$ instead of the wave function, which reduced the problem from $3n$ to three variables [160]. With this approach, it can be shown that the initial state can be described accurate enough through the electron density [161]. Therefore, the real system of interacting particles is changed to non-interacting particles. The calculation of the initial state according to *Kohn-Sham* yields the solution of the initial state. But a problem arises with the exchange correlation $V_{ex}(r)$ term and the equation can not be solved, because the exact form of $V_{ex}(r)$ is unknown, which describes all possible effects of a many-body problem [160]. Therefore, the term will be exchanged with approximated functions like the local density approximation (LDA) or with the generalized gradient approximation (GGA). With the LDA, only local exchange reactions are considered. The result is applicable only for homogenous electron distributions in a material. By an extension to the LDA, the GGA considers additional the gradient of the electron density distribution $n(r)$ at the position r. The results of this work are based on the work of Perdew and Wang [162]. To solve the Kohn-Sham equation, the so called projector augmented wave (PAW) is used. It reconstructs the wave function and fixes the inner electrons, which do not participate in the chemical bonds [163]. Consequently, the energy of the system can be calculated based on the position and the chemical mixture of the initial state. For *ab initio* calculations of a doped system, the local distribution of the atoms is important. The values of the c-matrix are determined by using a random distribution of the doping elements in the aluminum lattice using a special quasi-random structure (SQS). The dimension of the system was a 4x4x2 unit cell with 128 atoms.

For the determination of the *ab initio* based elastic constants, the structure is strained 6 times using the universal independent coupling strain approach [164]. The strained structure is relaxed and from the observed relation of mechanical stress and strain, the linear elastic tensor C_{ij} can be evaluated using a fitting tool. Finally, a hexagonal projection of the elastic tensor is implemented to get the symmetry of the crystal back [165]. Using DFT perturbation theory as a final step, the piezoelectric tensor e_{ij} of the cells is calculated.

A.2 C-Matrix

In the following, the c-matrix and Young's moduli for AlN, AlScN and modified AlN are listed. The parameters for AlN were taken from literature [139].

$$C_{ij} = \left\{ \begin{matrix} 345 & 125 & 120 & 0 & 0 & 0 \\ 125 & 345 & 120 & 0 & 0 & 0 \\ 120 & 120 & 395 & 0 & 0 & 0 \\ 0 & 0 & 0 & 118 & 0 & 0 \\ 0 & 0 & 0 & 0 & 118 & 0 \\ 0 & 0 & 0 & 0 & 0 & 110 \end{matrix} \right\} GPa \tag{A.3}$$

$$e_{ij} = \left\{ \begin{matrix} 0 & 0 & 0 & 0 & -0.48 & 0 \\ 0 & 0 & 0 & -0.48 & 0 & 0 \\ -0.58 & -0.58 & 1.55 & 0 & 0 & 0 \end{matrix} \right\} C/m^2 \tag{A.4}$$

The parameter for AlScN were calculated in cooperation with the Institute of Materials Science and Technology by Dr. Holger Euchner using DFT method.

$$C_{ij} = \left\{ \begin{matrix} 305.8896 & 139.6300 & 129.5984 & 0 & 0 & 0 \\ 139.6300 & 305.8896 & 129.5984 & 0 & 0 & 0 \\ 129.5984 & 129.5984 & 253.2919 & 0 & 0 & 0 \\ 0 & 0 & 0 & 95.6678 & 0 & 0 \\ 0 & 0 & 0 & 0 & 95.6678 & 0 \\ 0 & 0 & 0 & 0 & 0 & 83.1298 \end{matrix} \right\} GPa \tag{A.5}$$

$$d_{ij} = \left\{ \begin{matrix} -0.0009 & 0.0002 & 0.0015 & -0.0001 & -0.0265 & 0.0066 \\ 0.0043 & -0.0043 & 0.0010 & -0.0274 & 0.0010 & 0.0011 \\ -0.0598 & -0.0624 & 0.1624 & 0.0011 & 0.0020 & -0.0011 \end{matrix} \right\} * 10^{-10} m/V \tag{A.6}$$

$$e_{ij} = \left\{ \begin{matrix} -0.0042 & 0.0140 & 0.0259 & -0.0008 & -0.2529 & 0.0533 \\ 0.0816 & -0.0575 & 0.0225 & -0.2619 & 0.0097 & 0.0091 \\ -0.6433 & -0.6854 & 2.1222 & 0.0106 & 0.0195 & -0.0086 \end{matrix} \right\} C/m^2 \tag{A.7}$$

To implement the influence of tilted grains occurring in sputtered AlN layers, the AlN compliance matrix from Tsubouchi was rotated and weighted with mean values gained from the rocking curve measurements from section 3.2.1.

$$C_{ij} = \left\{\begin{matrix} 345.0179 & 124.9887 & 120.0312 & 0 & 0 & 0 \\ 124.9887 & 345.0179 & 120.0312 & 0 & 0 & 0 \\ 120.0312 & 120.0312 & 394.8410 & 0 & 0 & 0 \\ 0 & 0 & 0 & 118.0183 & 0 & 0 \\ 0 & 0 & 0 & 0 & 118.0183 & 0 \\ 0 & 0 & 0 & 0 & 0 & 110.0146 \end{matrix}\right\} GPa \tag{A.8}$$

$$e_{ij} = \left\{\begin{matrix} 0 & 0 & -0.5763 & 0 & 0 & -0.5763 \\ 0 & 0 & 1.5423 & 0 & -0.4764 & 0 \\ -0.47646 & 0 & 0 & 0 & 0 & 0 \end{matrix}\right\} C/m^2 \tag{A.9}$$

A.3 Acoustic Wave

In solids, two types of waves are observed: longitudinal and shear waves. The velocity v of acoustic waves is related to the density ρ and the elastic constant c, according to the following equation [166]:

$$v = \sqrt{c/\rho} \tag{A.10}$$

An approach to calculate the phase velocity, which considers the wave normal $\vec{N}$ and the polarization direction $\vec{U}$, the Christoffel equation is applied:

$$\rho v^2 U_i = c_{ijkl} N_j U_k N_l \tag{A.11}$$

The derivation of the Christoffel equation, based on Newton's laws and the differential volume element, is given in [166]. By performing a contraction over j and l the equation becomes

$$\rho v^2 U_i = C_{ik} U_k, \tag{A.12}$$

where

$$C_{ik} = c_{ijkl} N_j N_l. \tag{A.13}$$

The four-order stiffness tensor c_{ijkl} can be written as a tensor of second-order using the Voigt notation. In matrix form the Equation A.12 becomes

$$\rho v^2 \vec{U} = C\vec{U}. \tag{A.14}$$

To calculate the phase velocity, the eigenvalue problem of the product ρv^2 has to be solved. For bulk acoustic waves the calculated velocities are faster by a material specific factor R compared to surface acoustic waves [166]. To estimate the influence of the

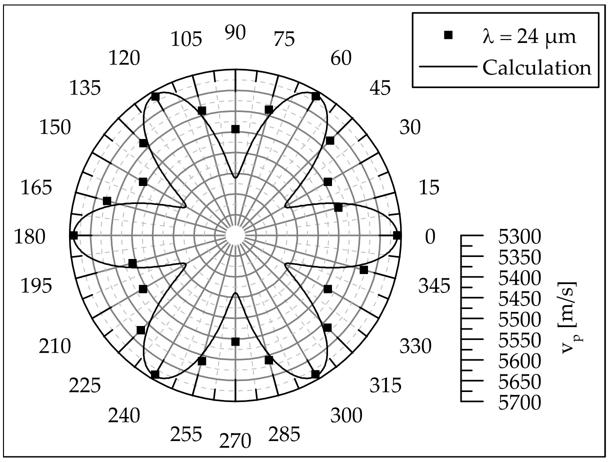

Figure A.1: Normalized calculated phase velocity (solid line) and measured phase velocities of 2 µm AlN layer on top of sapphire (points) dependent on the wave propagation direction. An angle of 0° corresponds to the $\langle 11\bar{2}0 \rangle$ direction of the sapphire substrate.

substrate on the phase velocity of multi-layer structures depending on the wave propagation direction along different substrate orientations, the calculated wave velocities are normalized to the measured phase velocities along the $[11\bar{2}0]$ direction of c-plane sapphire. Figure A.1 shows normalized calculated phase velocity and measured phase velocities of SAW devices with $\lambda = 24$ µm and $h_{AlN} = 2$ µm, which are also shown in section 5.2. The measurements are in good agreement with the calculated wave velocities. As expected the physical property of SAW devices must include the symmetry of the point group of the substrate, which was first approached by F. Neumann [167]. The deviation at 30° can be attributed to the influence of the AlN layer stiffness.

A.4 SAW Simulations

To extract parameters from SAW devices, such as phase velocity, a detailed experimental study has been performed. Therefore, for each parameter and design dimension a new device has to be fabricated. To understand the properties of the complex device based on multilayered structure, simulations help to separate different influences on the performance of the device.

The mathematical models for SAW devices can be divided into two groups. One approach includes 1D simulations utilizing approaches with lumped parameters and was first used in the 1960s. It is a quite rough estimation and only predicts the basic device behavior. It does not deliver a result in every point if interest. These models are currently used to design SAW devices. The first application used the delta-function impulse - response model published by Tancrell *et al.* [168]. For this, the transducers are assumed to be reflection less and uniform. The disadvantage of this system is, that the impedance can not be calculated [169]. The next, improved approach is the equivalent circuit model [170], where an equivalent array of bulk wave transducers are simulated. The electrical field is in this case either vertical (cross-field model) or horizontal (in-line model) with the *cross-field* being in better agreement with experimental data. It covers capacitance, transduction, propagation and reflection calculations [169]. A recent model is coupling of modes (COM) [171]. It is a system of differential equations and describes the interaction between forward and backward propagation waves. This approach gives algebraic expressions for the parameters conversion, reflection and admittance. Needed input parameters are transduction, reflection, velocity and attenuation [169]. An improvement is the P-matrix model, which can be considered as an algebraic equivalent of the COM model [172]. It is based on a *black box* principle, with one electrical and two acoustic ports. The advantage is that every part of the SAW device can be specified with a 3x3 P-matrix. The whole device can than afterwards be described by a concatenation of the P-matrices. The disadvantage is that the input parameters (conversion, reflection and admittance) has to be known. They can not be deduced by the model itself.

The second group of mathematically models for SAW devices are the analysis of the stop-band. The analysis yields the sound velocity and the reflection coefficient of the system. The mathematical models are based on partial differential equations, which describe the electro-mechanical field coupling. The first approach was suggested by Milson *et al.* [173], with a combination of numerical and analytical techniques. The numerical model calculates the electron charge across the electrode and the analytical model calculates a semi-infinitive 2D piezoelectric half space using the Green function. Hashimoto and Yamaguchi improved the model with a discrete Green function for modeling a wave under periodic grating [174]. Due to the investigation of the film thickness by Chen *et al.* newer models were developed to consider this parameter [175]. The idea is to use FEM simulations for the electro-mechanical behavior and the Green function for the piezoelectric substrate. Two models are gained from this approach. The first is the boundary element method (BEM) and the second the spectral domain analysis (SDA) [176]. The simulation tools are now able to deal with complex structures, which include thin film inhomogeneities, layered structures or the position of the electrode. Furthermore, external physical influences for example like temperature, humidity or pressure can be taken into account. The disadvantage is the amount of nodal points and hence, the different mesh densities inside the substrate and the electrode, which consumes a lot of computation power. The most simplification of the structure is the use of periodic patterns, for example one finger of the electrode grating with a 2D spatial dependency of the wave.

The results of the simulation in this work are based on the numerical model on finite element (FE) frequency domain for a unit cell of periodic structure. The model consists of a piezoelectric layer, metallic electrode and a substrate. A Bloch-periodic boundary condition is implemented for possible periodic pattern. Furthermore, a special absorption boundary condition in form of a perfectly matched layer is applied (PML), which reduces the simulation time. The analysis of the harmonic admittance gained by the FE simulation yields the desired COM and P-matrix parameter. With these parameters, the phase velocity, reflectivity and capacity can be calculated [177]. The compliance matrix for the simulations are listed in section A.2. The simulations were performed by Dr. Kirill Shaposhnikov in cooperation with the Institute of Mechanics and Mechatronics.

Curriculum Vitae

Manuel Gillinger

Personal Information

Date of Birth	8. July 1984
Place of Birth	Villach
Nationaly	Austria

Education

November 2012	**Entered PhD programme at Institute of Sensor and Actuator**, TU Wien
Januar 2012	Recieved degree of "Diplomingenieur"
2008-2012	**Master programme Microelectronics**, TU Wien
	Diploma Thesis *Elektrische Transportuntersuchungen an quasi 1D NiGe/Ge Nanowire Heterostrukturen* Supervisor: O.Univ.Prof. Dr.phil. Emmerich Bertagnolli, Ao.Univ.Prof. Dipl.-Ing. Dr.techn. Alois Lugstein
July 2008	Recieved degree of "Diplomingenieur (FH)"
2007-2008	**Diplomingenieur programme "Economic and Infrastructure"**, FH Kapfenberg
	Diploma Thesis

	Measurement System for Magnets used in the end-of-line test of automotive angle sensors Supervisor: DI. Wolfgang Steinbauer
09-12/2006	**Erasmus programme at IT Sligo,**
2004-2006	**Diplomingenieur programme "Economic and Infrastructure"**, FH Kapfenberg
Juni 2003	Passed Matura Exam
1998-2003	**Höhere Technische Bundeslehranstalt**, Klagenfurt, Regelungs und Netzwerktechnik

WORK EXPERIENCE

04-10/2012	**IMS Nanofabrication AG**, Vienna
2001-2010	**Infineon Technologies Austria AG**, Villach Different departments during summer vacation and diploma thesis (2008)